LBL--32436

DE93 000587

Measurements of the Cosmic Microwave Background Temperature at 1.47 GHz

Marc John Bensadoun
Ph.D. Thesis

Department of Physics
University of California

and

Physics Division
Lawrence Berkeley Laboratory
University of California
Berkeley, CA 94720

November 1991

This work was supported in part by the National Science Foundation Grants Numbers DPP87-16548 and AST 84-06187, and by the Director, Office of Energy Research, Office of High Energy and Nuclear Physics, Division of High Energy Physics, of the U.S. Department of Energy under Contract No. DE-AC03-76SF00098.

Measurements Of The Cosmic Microwave Background Temperature at 1.47 GHz

by

Marc John Bensadoun

Abstract

A radiofrequency-gain total power radiometer measured the intensity of the cosmic microwave background (CMB) at a frequency of 1.47 GHz (20.4 cm wavelength) from White Mountain, California, in September 1988 and from the South Pole, Antarctica, in December 1989. The CMB thermodynamic temperature, T_{CMB}, is 2.27 ± 0.25 K (68% C.L.) measured from White Mountain and 2.26 ± 0.21 K from the South Pole site. The combined result is 2.27 ± 0.19 K. The correction for galactic emission has been derived from scaled low-frequency maps and constitutes the main source of error. The atmospheric signal is found by extrapolation from zenith scan measurements at higher frequencies. The result is consistent with previous low-frequency measurements, including a measurement at 1.41 GHz (Levin *et al.* 1988) made with an earlier version of this instrument. The result is ~2.5 σ (~1% probability) from the 2.74 ± 0.02 K global average CMB temperature.

Contents

List of Figures

List of Tables

Acknowledgements

Where to begin? On the science side of life, my advisor, George Smoot, has been a source of solid physics intuition and a different perspective on physics and life. Steve Levin, who suffered through the group's early efforts at low-frequency measurements, has been a source of optimism, energy and new ideas. Chris Witebsky has provided perceptive, thoughtful advice and criticism on every aspect of this project. I thank him for his invaluable help in the design and construction of the new cold load. Al Kogut brought the group's computer software into the modern era; we enjoyed many ultimate frisbee games and Monday evening dinners before Al escaped to the East Coast. Giovanni De Amici, a mainstay of the group, has been present on every expedition since 1982. Marco Bersanelli and Michele Limon have helped with every phase of this work, both physically and psychologically; I thank them for unforgettable times. I thank Steve, Chris, Al and Marco for their generous help in the design of the experiment and the data analysis.

John Gibson provided custom-built electronics to make the experiment a reality. Thanks to the Radio Astronomy Laboratory, and Tap Lum in particular, for help in building the radiometer's first-stage HEMT amplifier and assistance in radiometric testing of the radiometer and cold load. Armando Meuti (and, later, Richard Kuiper) taught me how to make art in the machine shop. I made good on Luis Alvarez's opinion that an experimental physicist should spend half his time making an experiment.

Jon Aymon, the group's poet-in-residence, has helped me with computing and life at work. Faye Mitschang and Jeanette Larsen have helped me survive the paperwork side of life at LBL. For help during various phases of this work, I thank Giuseppe Bonelli, Francesco 'Stikkis' Cavaliere, Barron Chugg, Doug Heine, Gary Hinshaw, Jenny Hwang, Jay Levin, Larry Levin, Giorgio Sironi, and Luis Tenorio.

The staffs and crews at the White Mountain Research Station and the Amundsen-Scott South Pole Research Station have been a pleasure to work and live with and they have eagerly provided first rate support, far beyond the call of duty. My experiences at the South Pole have been particularly satisfying, and I thank the Met and Comms folks in particular for making it possible to finish this thesis during the 1991 expedition and send it back to Berkeley.

This research was funded in part by the National Science Foundation Grants Numbers DPP 87-16548 and AST 84-06187 and by the Director, Office of Energy Research, Office of High Energy and Nuclear Physics, Division of High Energy Physics of the U.S. Department of Energy under Contract DE-AC03-76SF00098.

On a personal note, Paul Selvin, Nathan Hunt, Jim Garnett and I (with part-time participation from Chris Goedde, Jeff Svoboda and others) spent countless hours engaged in bughouse madness. We occasionally did physics together.

Thanks to Myriam Zini for her support during four years of graduate school.

My profound thanks go to my parents, André and Paula, for their encouragement, love, and for the example they set for me. Paul and Jennifer, Helen, Aldo, and the rest of my family have been a source of adventure, warmth and support. I thank my son Daniel for inspiration.

Special thanks to Cristina Hawes for a wonderful, crazy year spent on opposite sides of the continent, for unflagging support and love, and for help when I most needed it.

Chapter 1 Introduction to the Measurement

1.1 Cosmology

Twenty-six years after its discovery, the cosmic microwave background (CMB) remains as one of the three primary pieces of evidence for the Hot Big Bang theory which has become the 'Standard Model' of the universe. The triad is: the general recession of the galaxies, primordial nucleosythesis and the CMB. Each provide us with information about the universe during its infancy.

The philosophical underpinning of the Hot Big Bang theory is the continuation of the progression in our world view from the Ptolemaic Principle (anthropocentric) to the Copernican Principle (heliocentric) to the Cosmological Principle. The Cosmological Principle maintains that there is no special place in the universe or, in cosmological terms, that on large scale the universe is spatially homogeneous and isotropic. The Cosmological Principle applies only to the universe on large scales, although, to date, observations of the luminous matter in the universe have shown structure on all scales including the largest observed. In contrast, the CMB is observed to be isotropic to high order. It stands alone as strong evidence of the Cosmological Principle and that, the universe approaches isotropy on progressively larger scales.

The Hot Big Bang theory describes the universe as a homogeneous and isotropic (and therefore structureless) space described mathematically by the Robertson-Walker metric. A direct consequence of homogeneity and isotropy is that the distance, $d(t)$, between two galaxies satisfies the relationship

$$d(t) = r_0\, a(t) \tag{1.1}$$

where r_0 is time-independent comoving 'distance' and $a(t)$ is the scale parameter (*e.g.* Peebles 1971). A direct consequence of the distance relationship is that the relative velocity between galaxies is proportional to their distance. This is known as Hubble's law:

$$v \equiv \dot{d} = \frac{\dot{a}}{a} d \equiv H d \tag{1.2}$$

where v is the relative velocity of the galaxies and d their proper distance. Experimentally, H is observed to be positive and therefore the universe is expanding. The Einstein equations and energy conservation imply that, as long as the sum of pressure, p, and density, ρ, remains positive, H decreases with time (*e.g.* Weinberg 1972):

$$\dot{H} = \ddot{a} = -\frac{4\pi G}{3} a (\rho + 3p) \tag{1.3}$$

where G is the gravitational constant. A kinematic effect of the expansion is the radiation redshift relation:

$$1 + z \equiv \frac{\nu_e}{\nu_0} = \frac{a(t_o)}{a(t_e)} \tag{1.4}$$

where z is the redshift, ν_e and ν_0 are the emitted and observed frequency of the radiation, respectively, and t_e and t_0 are the times of emission and observation, respectively.

A direct consequence of equations (1.2) and (1.3) and the observed sign of H (galaxies are generally receding) is that the universe passes through an early phase where the matter is dense and hot (hence the name Hot Big Bang).

1.2 CMB Spectral Distortions

The Hot Big Bang theory, predicts the existence today of an isotropic, blackbody radiation. At early times, the radiation background is in thermal equilibrium with the matter and photons are freely created and destroyed producing a Planck spectrum. As the universe expands, the spectrum remains blackbody and the photons injected to the

background at z ~ 1000 only cause a slight perturbation to the spectrum. Further expansion of the universe preserves the Planck spectrum with the temperature scaling according to $(1 + z)^{-1}$. At the present epoch, this photon spectrum which fills the universe, peaks in the microwave, hence the name cosmic microwave background.

A blackbody spectrum has a specific photon spectrum and spectral intensity given by the Planck occupation number (per photon mode):

$$\eta_P = (e^x - 1)^{-1} \tag{1.5}$$

where $x = h\nu / kT$, h is the Planck constant, and k is the Boltzmann constant, and T is the thermodynamic temperature. For a given occupation number, the brightness temperature of the photons, T_B, is given by:

$$T_B(x) = \frac{xT}{ln[1 + 1/\eta(x)]} \ . \tag{1.6}$$

and the brightness temperature of a blackbody spectrum is:

$$T_B(x) = T \ . \tag{1.7}$$

Any addition of photons to the spectrum or change in the energy of the existing photons causes a distortion in the spectrum. Two factors determine if the spectrum will be restored to a Planck spectrum. Firstly, there must be a way to create and destroy photons on a timescale short compared to the expansion time. Secondly, there must be a way to redistribute the photons in energy on a timescale short compared to the expansion time.

At early times, when the universe is more than 10^9 times smaller than at present ($z > 10^9$), the average energy of the background photons we observe today is 0.23 MeV. During this "Lepton era", photons and electron-positron pairs are in equilibrium, with roughly equal numbers of electrons and photons. During the Lepton era, pair creation, annihilation, and scattering efficiently restored any distorted spectrum to blackbody.

Therefore, one cannot expect to find distortions in the spectrum due to processes which occurred before the end of the Lepton era.

Radiative Compton scattering continues to maintain a blackbody spectrum until a redshift $z_{therm} \sim 2\times10^6\ \hat{\Omega}_b^{-1/3}$ (Danese and De Zotti 1977), where $\hat{\Omega}_b = h^2\Omega_b$; $h = H_o/(50\ \text{km-sec}^{-1}\text{Mpc}^{-1})$ is the normalized Hubble constant, and Ω_b is the ratio of the baryon density of the universe to the critical density. Thus the e^+-e^- annihilation radiation ($\Delta\varepsilon/\varepsilon \approx 2.85$, *i.e.*, the energy released was nearly three times the radiation energy), the small energy release from primordial helium synthesis ($\Delta\varepsilon/\varepsilon \approx 10^{-6}$) at $z \sim 10^7$, and any other release before z_{therm} are all re-thermalized and are not practically observable.

After z_{therm}, radiative Compton scattering can no longer restore the blackbody photon number density but (non-radiative) Compton scattering can still thermalize the spectrum. An energy release during this epoch results in a chemical potential, or μ-, distortion. A μ-distortion is characterized by a Bose-Einstein spectrum which dips down (for $\mu>0$) at low frequency, then rises (for $\mu>0$) at long wavelengths where bremsstrahlung produces photons fast enough to reestablish a blackbody spectrum. The occupation number for a μ-distortion is given by

$$\eta_{BE}(\nu) = [exp(x + \mu(x)) - 1]^{-1}, \tag{1.8}$$

where $\mu(x)$ is the frequency-dependent chemical potential which is driven to zero at low frequency by bremsstrahlung.

At a redshift of $z_1 \sim 4\times10^4\ \hat{\Omega}_b^{-1/2}$ (when the universe is roughly 500 years old), the density of electrons becomes so low that Compton scattering can no longer establish a thermal Bose-Einstein distribution. Because the spectrum does not have time to reaach equilibrium, an energy injection at this time causes a spectral distortion whose form depends on the mechanism and epoch of the energy release. If the energy release is via heating of the photons, Compton scattering acts to establish a Bose-Einstein distribution but, for $z < z_1$, the redistribution of photon energies does not proceed fast enough to

achieve kinetic equilibrium (a μ-distortion is not achieved). The resulting spectrum has a slight excess of photons at high frequencies and a depletion at low frequencies and the very-low-frequency part of the spectrum thermalized by bremsstrahlung emission. If the energy release is via photons added to the spectrum, the feature will persist to the present, since Compton scattering does not proceed fast enough to redistribute the added photons.

At $z \sim 1000$, the photon background is no longer energetic enough to keep the plasma ionized, the plasma combines ('recombination'), and the dominant form of interaction changes from Compton scattering to Rayleigh scattering. At the peak of the photon background the cross section for interaction decreases by four orders of magnitude, and the radiation travels without scattering from recombination until the present.

After recombination, if the energy transfer to the CMB is via a direct heating of the plasma, bremsstrahlung (free-free emission) efficiently populates the low-frequency part of the spectrum, and, after z_1, Compton scattering does not have sufficient time to redistribute the excess of low frequency photons. The free-free distortion signature is a brightness temperature which deviates from blackbody as

$$\frac{\Delta T}{T_0} \approx 3.2 \times 10^3 \left(\frac{\nu}{1\ \mathrm{GHz}}\right)^{-2} Y_{\mathrm{ff}}, \tag{1.9}$$

where Y_{ff} is the amplitude of the distortion and T_0 is the unperturbed temperature. The distorted spectrum ultimately reaches the plasma temperature (Bartlett and Stebbins 1991). At frequencies below a few GHz, this distortion would not be revealed by past CMB measurements because of the large uncertainties in the measurements in this range and because galactic synchrotron emission partially masks any distortions present.

A free-free distortion is of interest because it probes the temperature and density of the intergalactic medium, and may provide verification that 'recombination' at $z \approx 1000$ actually occured or reionization has occurred.

distortions is not fixed because the former is linearly proportional to the density of the plasma while the latter is proportional to the density squared. Thus, even though high frequency (COBE FIRAS) results strongly limit the Compton distortion, they only very weakly limit the low frequency free-free distortion. The sensitivity to a free-free distortion is a strong motivation for these measurements.

Particle (WIMP) decay produces a low-frequency distortion with magnitude, shape and characteristic frequency dependent on the mass, lifetime and decay mode of the particle (Silk and Stebbins 1983). For a particle with a photonic decay mode, the addition of photons to the spectrum produces a distortion characterized by a negative chemical potential. An review of energy releasing processes is given by De Zotti (1986).

1.3 Previous Low-frequency Measurements

Recent results from the FIRAS experiment aboard the COBE satellite (Mather *et al.* 1990) have established the blackbody nature of the spectrum above 30 GHz and focused attention on the low-frequency spectrum. High precision measurements in the low-frequency region $\nu < 10$ GHz potentially have higher sensitivity to μ- and Y_{ff}-distorted spectra than the FIRAS.

Previous low-frequency measurements have limited precision, typically $\geq \pm 0.5$ K at frequencies below 10 GHz. One reason for the large error is the difficulty of calibrating at low frequencies. A radiometer antenna operating at 1.5 GHz with a beam size of $<30^{o}$ has an aperture of >50 cm. This is larger than the size of the LHe-cooled calibrators in use at the time and these instruments were not calibrated at the antenna aperture. If the radiometer cannot be calibrated at the aperture, a correction must be made for emission upstream of the calibration. The correction for antenna and transition emission is difficult to evaluate and prone to systematic error. In the cases where a cooled coaxial termination

was used, the correction for emission from the warm part of the coaxial line introduced large errors.

Other sources of error in previous low frequency measurements are atmospheric emission (for measurements made at sea level), ground emission, and galactic emission. As of 1980, measurements of the low-frequency spectrum could place only a 10% limit on fractional energy release during the $10^7 > z > 10^4$ period.

Precise measurements in the 1-2 GHz range combined with precise the high-frequency measurements now available are an ideal probe of μ and Y_{ff} distortions. A measurement near 1.5 GHz is low enough in frequency to make the temperature deviate significantly from an unperturbed, but high enough that the foreground galactic signal is still a factor of three less than the CMB.

Since 1982 the LBL Astrophysics Group and collaborating groups have made measurements of the CMB spectrum at frequencies between 0.6 and 90 GHz which have greatly improved our knowledge of the spectrum (e.g. Kogut *et al.* 1991 and references therein). In 1986 we made a measurement at 1.410 GHz (Levin *et al.* 1988); based on that experience, I built a new radiometer and cold load calibrator to make measurements at 1.47 GHz.

In September 1988, the LBL Astrophysics group made CMB measurements at 3.8 GHz (De Amici *et al.* 1990), 7.5 GHz (Kogut *et al.* 1990), and 1.47 GHz from White Mountain (WM). In December 1989, we repeated these measurements from the South Pole (SP) and a collaborating group made measurements at 0.82 and 2.5 GHz. The results from the South Pole are reported in Sironi *et al.* (1991), De Amici *et al.* (1991), Levin *et al.* (1992), and Sironi *et al.* (1992). The measurements at 1.47 GHz are the subject of this thesis.

Chapter 2 Concept of the Experiment

2.1 Measurement Concept

The measurement is performed with a total-power radiometer whose output signal, S, is proportional to the power, P, entering the antenna aperture. The output is calibrated in units of antenna temperature, T_A, defined by the relation

$$T_A \equiv \frac{P}{kB} = \frac{T_\nu}{e^{T_\nu/T} - 1} \approx T - \frac{T_\nu}{2} \quad \text{for } T >> T_\nu$$

where B is the bandwidth, $T_\nu = h\nu/k = 0.0706$ K at 1.47 GHz, h is the Planck constant, and k is the Boltzmann constant. For temperatures of ~4 K, the antenna temperature is ~ 0.035 K lower than the thermodynamic temperature.

The experiment consists of comparing the zenith with a large, liquid-helium cooled, cold-load calibrator (CL) whose antenna temperature, $T_{A,load}$, is precisely known. The antenna temperature of the zenith, $T_{A,zenith}$, is:

$$T_{A,zenith} = G\,(S_{zenith} - S_{load}) + T_{A,load} - \Delta T_{inst} - \Delta T_{A,joint}, \qquad (2.1)$$

where G is the gain calibration coefficient for the radiometer, ΔT_{inst} is the correction for any changes in the radiometer offset associated with its inversion and $\Delta T_{A,joint}$ is the differential temperature contribution from the imperfect joint between the antenna and the cold load interface plate and the ground screen interface plate.

The temperature of the CMB is found by accounting for all non-cosmological contributions to $T_{A,zenith}$. These include emission from the atmosphere, ground, the sun and moon, and man-made radio-frequency interference (RFI):

$$T_{A,zenith} = T_{A,sky} + T_{A,atm} + T_{A,ground} + T_{A,sun} + T_{A,RFI}\,. \qquad (2.2)$$

These contributions are shown schematically in Figure 2.1. The atmospheric signal is found by extrapolating from measurements at higher frequencies. The ground signal is found by convolving the measured antenna gain pattern with the ground emission. The terms in Equations (2.1) and (2.2) are discussed in detail in Chapter 5.

The sky temperature, $T_{A,sky}$, is defined as the sum the galactic emission and the CMB:

$$T_{A,sky} = T_{A,CMB} + T_{A,gal}. \tag{2.3}$$

Galactic emission, which includes emission from our galaxy and other galaxies, is calculated from low-frequency maps and the observed spectral index. A detailed discussion of the galactic signal is given in Chapter 7. The signals from the atmosphere, ground, and cold load are constant during each measurement whereas the galactic signal varies due to the earth's rotation.

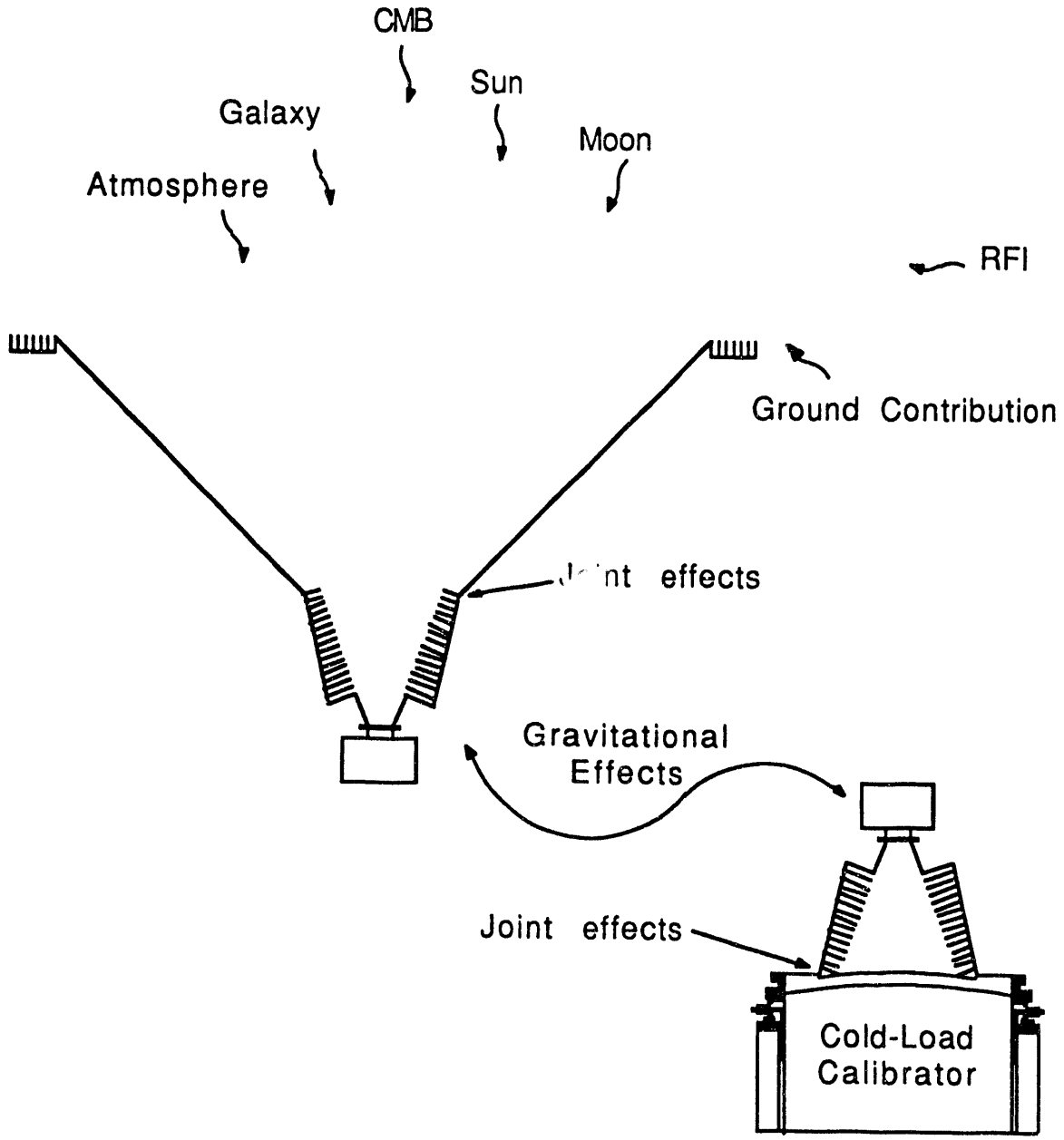

Figure 2.1 Concept of the experiment

2.2 Foreground Signals

Foreground signals are those signals originating from outside the antenna aperture which are not of cosmological interest. As such, this includes everything from emission from the joint at the aperture of the antenna to extragalactic emission from other galaxies. Some foreground signals can be reduced or removed entirely by choice of the observation site and time of observations (atmospheric, galactic, ground, and solar emission, RFI) while others can be reduced by the design of the instrument and apparatus (ground and solar emission, RFI, orientation-dependent, load-dependent and joint effects). Some are the result of a trade-off, like the small emission from the ground screen which is used to reduce the much larger ground emission signal.

The following foreground signal considerations are important in site selection. The solid angle subtended by the ground must be minimized to reduce the ground signal. Practically speaking, a flat horizon is ideal. The magnitude and temporal variability of atmospheric emission and the characteristic roll-off frequency of the emission both decrease with increasing altitude necessitating a high-altitude site. The copious RFI emission associated with population areas requires a remote site. Minimum error from the galactic correction requires a region of sky with minimal galactic emission and to be near overhead during the observations.

The two sites chosen for the measurements are on White Mountain in California and at the South Pole in Antarctica. The White Mountain site has rocky terrain, a low horizon (rising as high as 18^{o} above horizontal in one direction) and is remote. The atmospheric emission is low (due to the high altitude), variable, and sometimes near the minimum value for the site's altitude. The galactic signal is modulated by the Earth's rotation. The South Pole site sits on nearly 3 km of packed snow and ice, has a flat horizon and is very remote.

Atmospheric emission is very stable but is not as low as the minimum value from the White Mountain site (which is at higher altitude). The galactic signal at the zenith is ~0.8 K.

The following foreground signal considerations are important in the design of the radiometer. An isotropic antenna at a site with a flat horizon and 273 K ground temperature would see 136 K of emission. Low sidelobe response and ground-screen shielding of the antenna are necessary to cope with this signal. The low sidelobe response generally means the beamwidth is small and the response very directional. The small beamwidth allows the radiometer to observe away from the zenith (without undue ground pick-up) and means that strong sources (like the galactic plane or the sun) contribute less to the signal. This is difficult to achieve at long wavelength and still calibrate the radiometer at the antenna aperture.

While ground emission, RFI, and solar emission can be greatly reduced as sources in ground-based CMB measurements, the atmosphere and galaxy are ever-present sources. Even after proper site selection these are the dominant foreground sources as shown in Figure 2.2.

This measurement is a single frequency measurement. The result must be taken together with other measurements of the CMB temperatures at other frequencies to provide spectral information. It is therefore important to consider the spectral dependence of the foreground signals. The foreground spectrum is also important because, in some cases, it is used to help remove a foreground signal (*e.g.* atmospheric emission). Figure 2.3 demonstrates how the main foreground signals define a frequency range, approximately $1.5 < \nu < 15$ GHz, where the CMB is > 50% of the total signal and precise ($\leq \pm 0.1$ K) ground-based CMB measurements can be made.

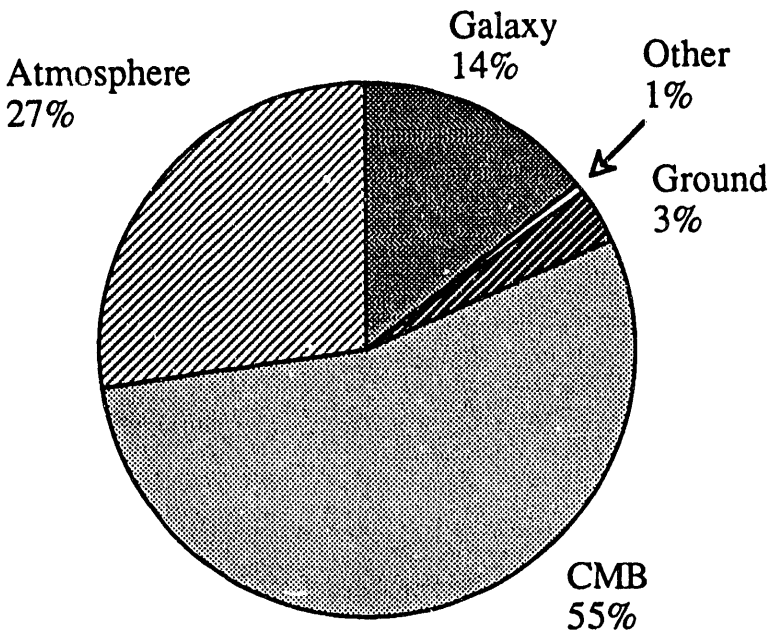

Figure 2.2 Approximate breakdown of the zenith sky temperature at 1.5 GHz from the South Pole site.

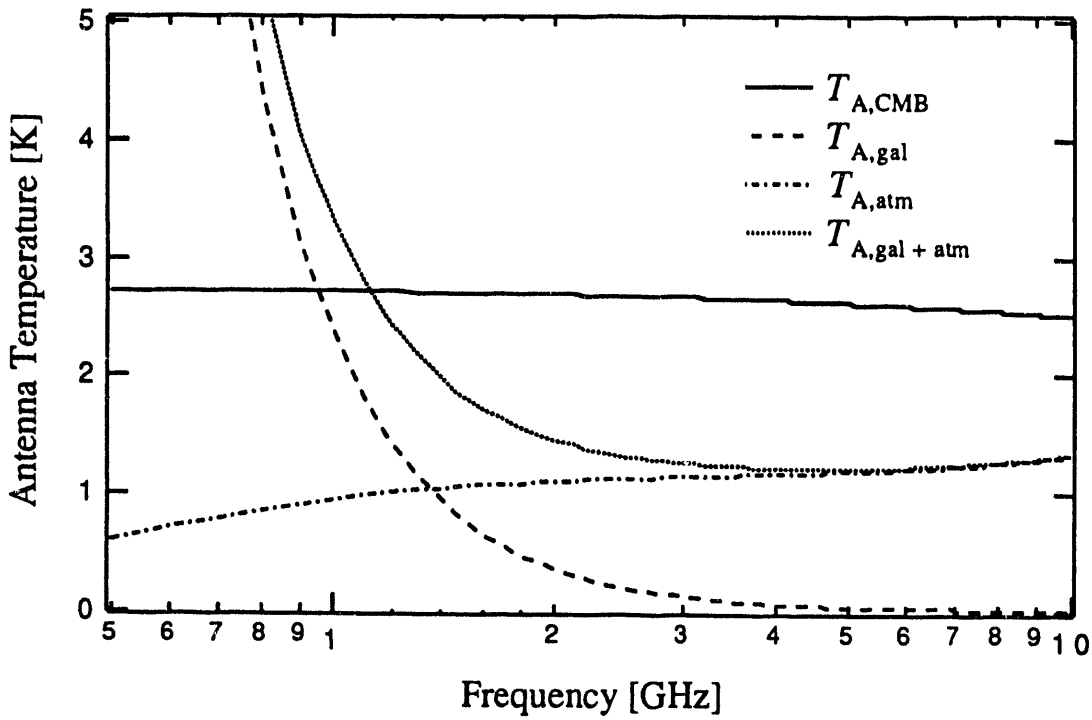

Figure 2.3 Foreground sources at low-frequencies. Values are for the zenith sky at the South Pole.

Chapter 3 The Equipment

3.1 The Radiometer

The radiometer has an E-plane corrugated horn antenna and a radiofrequency-gain total-power receiver (see Figure 3.1 and Table 3.1). Advantages of this design are simplicity and ease of construction. Physically, however, the measurements are not easy. In contrast with Dicke-switched or correlation receivers which have two antennas and continually measure a signal difference, a total-power radiometer must be physically moved in order to measure a signal difference.

The output of a total-power receiver with system temperature T_{sys} and observing a load with temperature T_{load} is, neglecting any loss or reflection in the radiometer,

$$S_{load} = \frac{1}{G}(T_{sys} + T_{load}) . \tag{3.1}$$

(See §5.3 for a treatment including radiometer loss and reflection.) The rms thermal noise on the receiver output, known as the sensitivity T_{sens}, is (Krauss 1966)

$$T_{sens} = \frac{T_{sys} + T_{load}}{\sqrt{B\tau}} \tag{3.2}$$

for an integration time τ.

The rectangular aperture of the antenna measures 46 x 52 cm. The corrugations reduce the E-field amplitude on the E-plane walls and thereby reduce the sidelobe response. The waveguide-coaxial transition couples to the TE_{10} mode which has zero E-field on the H-plane walls; therefore, there are no corrugations on the H-plane walls (Witebsky *et al.* 1987).

The signal enters the antenna and passes via a waveguide-coaxial transition into coaxial cable. It is then amplified and filtered prior to detection. A 1.0-1.6 GHz bandpass

filter cuts out low-frequency RFI signals to avoid saturation of the second RF amplifier. The signal level at the output of each radiofrequency (rf) amplifier is at least 20 dB below the 1 dB gain saturation point.

A 6-stage Yttrium Iron Garnet (YIG) filter defines a 26 MHz instantaneous bandpass. During CMB measurements, the YIG filter center frequency is swept at 1 GHz/sec from 1.375 to 1.575 GHz to synthesize a bandwidth of 200 MHz centered at 1.475 GHz. The gain-weighted band center is 1.471 GHz. The rejection of YIG filters drops by 6 dB/octave/stage, where an octave is the 3-dB filter bandwidth. For this filter, the dropoff is 36 dB/26 MHz and the out-of-band rejection is ~115 dB. This Watkins Johnson YIG filter is the first 1-2 GHz 6-pole filter to be sold commercially. The filter showed no signs of sensitivity to moderate magnetic fields (the case is made from mu-metal) and the tuning current and heater wires are well shielded to prevent any cross-talk.

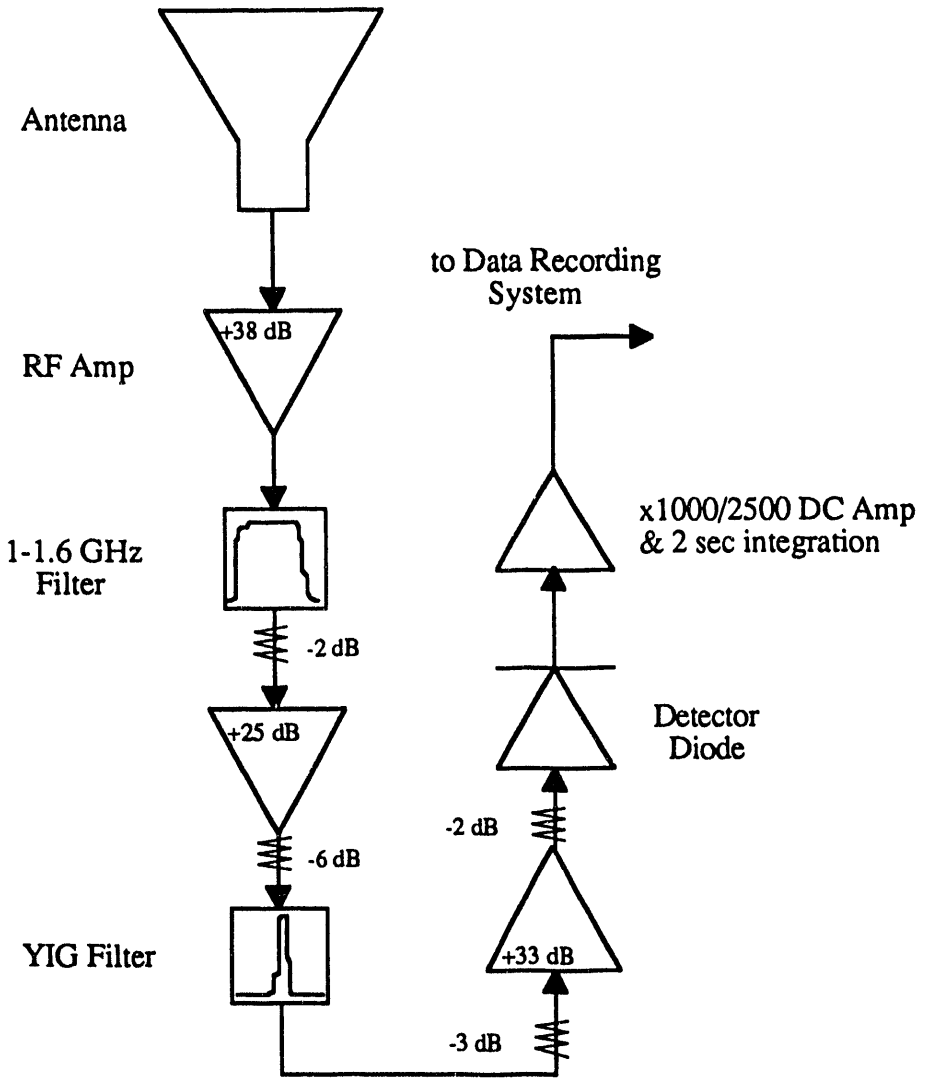

Figure 3.1 Radiometer schematic. Amplifier gains and attenuator values are given.

Table 3.1 1.47 GHz radiometer parameters

Parameter	Value	Comments
Center frequency	1.47 ± 0.01 GHz	Measured (λ = 20.4 cm)
YIG filter bandwidth	26 MHz	Measured
YIG sweep frequency	5 Hz	Measured
Synthesized bandwidth	200 MHz	Measured
System temperature	53.5 ± 0.4 K[a]	Measured with cold and warm loads
Sensitivity	10 mK $Hz^{-1/2}$	Theoretical
	18 mK $Hz^{-1/2}$	Measured with ambient target
Beamwidth [b]	30° x 27°	ExH-plane, measured w/ ground screen
Beam area	0.284 sr	Calculated
low gain	25.0 ± 0.2 K/V	WM, measured
	24.2 ± 0.1 K/V	SP, measured
gain ratio	2.537 ± 0.025	WM, measured
	2.488 ± 0.005	SP, measured
high gain	9.84 ± 0.12 K/V	WM, calculated
	9.74 ± 0.05 K/V	SP, calculated
DC amplifier offset	-10.04 ± 0.04 V	Measured with terminated input

[a] Uncertainty is the quadrature sum of the spread in measured values and the error on each value

[b] the half-power-beam-width (HPBW)

The rf signal is detected by a power-law detector diode and the DC detector diode ouput signal is then amplified by either 1000 (low-gain scale) or 2500 (high-gain scale). The signal is then integrated for 2 seconds, offset by -10 V and recorded. The -10 V offset is stable to better than 1 part in 10^4 over a period of a few minutes. The detector diode output is in the range 1.2-6.5 mV when the radiometer observes 4 K - 300 K targets. Saturation of the detector diode results in a 2.0 ± 0.9 % gain correction derived from measurements of the diode linearity.

The YIG filter provides flexibility since any band in the interval $1.3 < \nu < 1.7$ GHz can be selected for the observations. It also allows measurements at different frequencies over the band, which could in principle give information on galactic emission; in practice, the stability of the receiver and behavior of the joint at the horn mouth were such that this was not possible. The smaller instantaneous bandwidth degraded the sensitivity by a factor of ~3. This was a disadvantage in measuring systematic effects.

The measurement requires that the antenna mate to the ground screen, the ambient calibrator and the cold load (these three parts of the experiment are discussed in the following sections). The mating parts meet at a metal-to-metal joint (see Figure 3.2). The ground screen and ambient target rest on the antenna aperture; the radiometer rests on the cold load. During zenith scans, the radiometer hangs from beneath the extension and four latches pull the joint closed.

Each side of the antenna aperture consists of a 5 cm wide flat surface which is perpendicular to the antenna wall (the wall is at a 19° angle from the beam axis). The mating surface of the cold load interface plate and the extension have matching 5 cm wide surfaces at matching angles. The mating surface of the ground screen is a flat plate that makes contact with the antenna aperture along a line. The radiometric effect of the joints is discussed in §5.6 and §9.1.

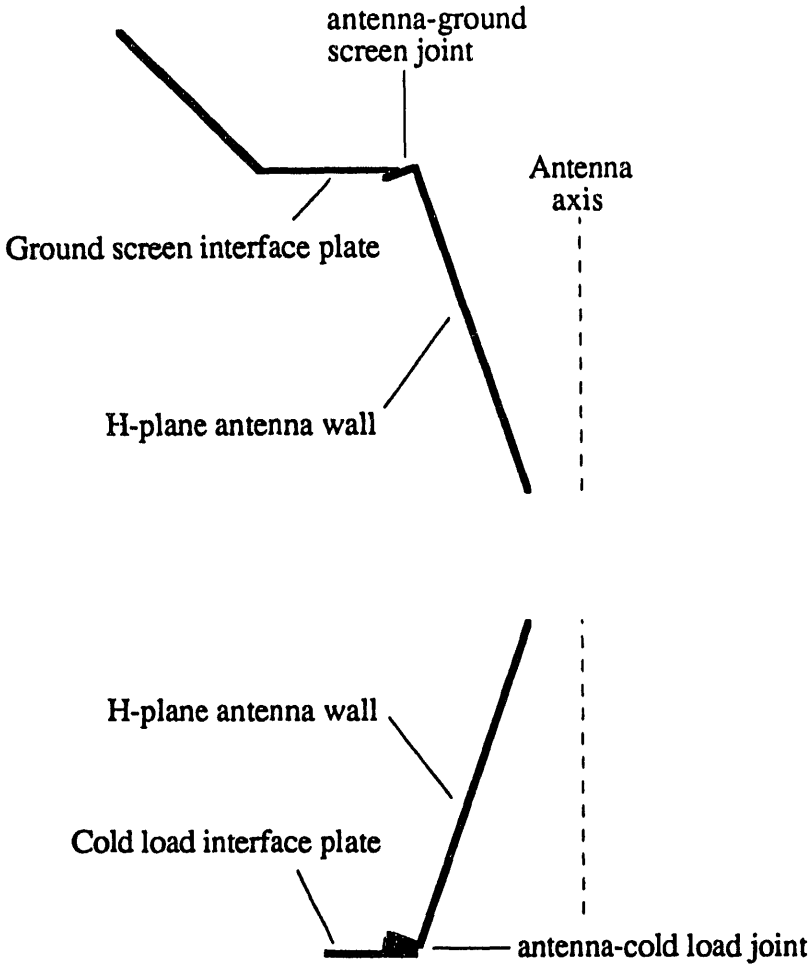

Figure 3.2 H-plane section of the antenna aperture joint design. The antenna and ground screen meet along a line; the cold load interface plate mates with the 2"-wide surface at the antenna aperture. In the E-plane, the antenna wall backplane angle is 13°, but the joint is the same as in the H-plane.

The temperature of the radiometer is actively controlled to reduce gain variations. Four temperature sensors monitor the rf components, electronics, antenna throat and ambient target temperatures. In 1988, the radiometer had one electronic angle sensor which measured the H-plane tip angle to ± 0.5°. In 1989, a second angle sensor was added in the E-plane, primarily as an aid in measuring the beam pattern.

The second angle sensor, which draws ~ 60 mA, pushed the radiometer's ±15 V power supply to the limit of its current capacity. This resulted in an oscillation in the

supply output which, in turn, caused the radiometer output to oscillate with a characteristic period of ~225 sec. The source of this problem was only discovered after the South Pole observations. Fortunately, this oscillation only appeared intermittently, and when it was present, introduced only scatter (but no offset) into the results.

3.2 The Ground Screen

The size of the antenna aperture is limited by the requirement that the antenna be able to observe the 78-cm diameter cold load. The resulting aperture is relatively small (~2.5λ for a pyramidal antenna) and the antenna gain pattern has a large half power beam width (HPBW). The zenith-looking antenna at the White Mountain site would observe ~0.6 K of ground radiation. A pyramidal ground screen reduces this signal by 0.30 K and quarter-wavelength traps on the E-plane sides of the screen further reduce the ground signal by 0.15 K. Figure 3.3 shows the measured E- and H-plane gain patterns with the ground screen as measured at the South Pole site.

The screen (shown schematically in Figure 2.1) has a square, flat mating interface which rests on the antenna aperture when in use. It has a 45° semi-flare angle and extends out to a 2.5 m square aperture. The ground screen edge is at ~56° from aperture center, just outside the base of the main lobe (at ~45°).

The ground screen interface plate was a flat aluminum sheet with a rectangular cut-out to match the antenna aperture. During observations of the zenith, the hole was positioned over the antenna aperture. This was difficult to align precisely although the sky signal was not sensitive to the precise positioning. For the South Pole observations, alignment plates were added to make the ground screen positioning simpler and more repeatable.

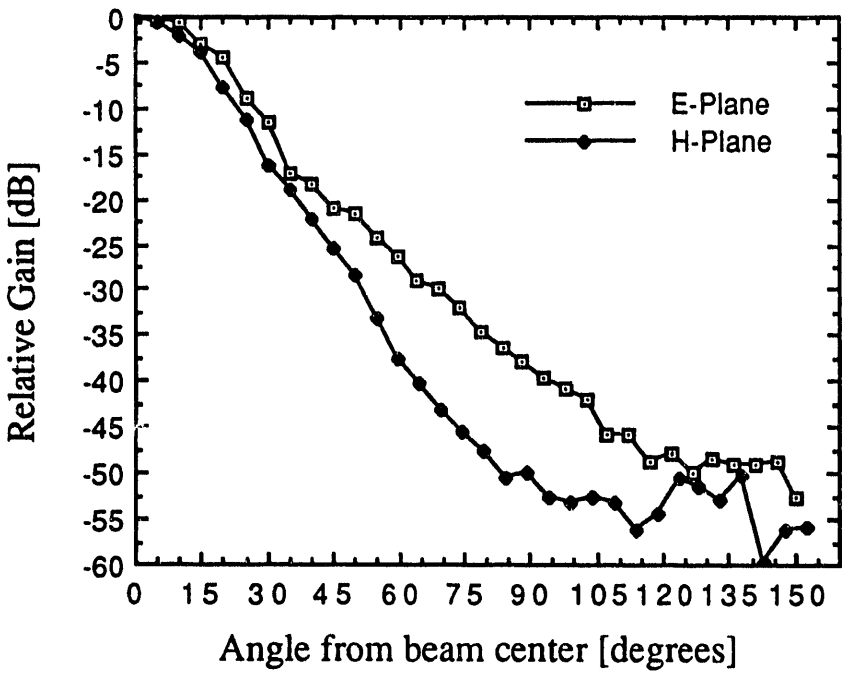

Figure 3.3 Gain pattern of the antenna and ground screen

The antenna was designed to operate with an extension to achieve the very low sidelobe response required. The ground signal with the extension in place was very low (<0.020 K at White Mountain, see Levin *et al.*, 1988), but the extension was lossy and contributed to the zenith sky temperature. This emission is difficult to measure precisely: removing the extension from the antenna changes the ground and galactic signals and the large mass of the extension prevented measurement of the emission by changing the physical temperature of the extension. The best tests indicated an extension emission of ~0.5 ± 0.2 K. This large loss was not expected but it is consistent with the ~5 K which the antenna and waveguide-coaxial transition loss contributed to the system temperature. The source of the loss is probably the resistive attachment of the corrugations to the backplane and the resistive joint around the transition backshort.

3.3 The Ambient Calibrator

The ambient temperature target is a 60 cm x 60 cm blackbody absorber enclosed in a thermally insulated, rf-tight box which covers the antenna aperture during gain calibration (see Figure 3.4). The absorber is VHP-6, a pyramidal open-celled foam with a 5 cm thick foam window on the front. The temperature of the target was monitored to ± 1 K.

The target has angle pieces made of thin, bent aluminum sheet screwed to the back for rigidity during instrumental offset tests. No signal was produced by pressing in the middle of the back of the target with a force much larger than the weight of the absorber and box. During offset tests, the target was secured to the horn aperture with four screws. In 1989 at the South Pole, heating strips were added to the target to allow heated target offset measurements.

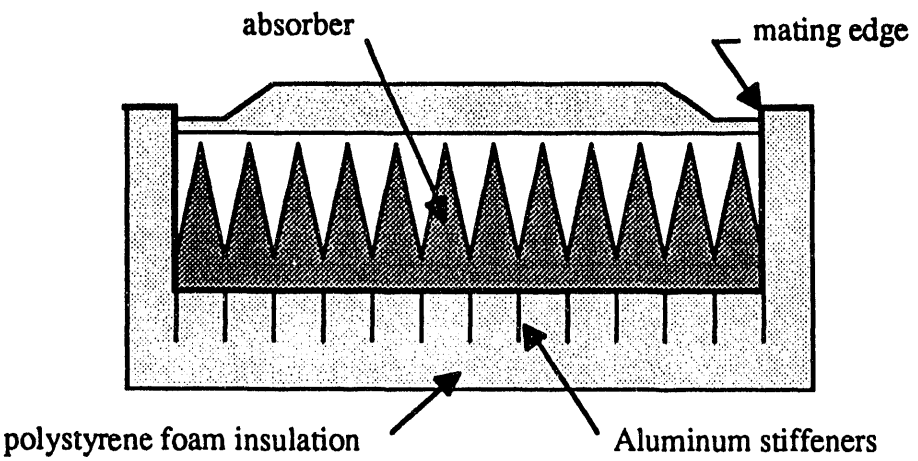

Figure 3.4 The ambient calibration target

3.4 The Cold Load Calibrator

The accuracy of the 'known' temperature reference and the precision of the measured difference are critical to the precision of the CMB measurement. These factors together lead to the use of a liquid-helium-cooled calibrator. Liquid helium (LHe) has three properties which are nearly ideal for these measurements.

First, at the ambient pressure of our sites, the LHe boiling point is within ≤0.2 K of the sky temperature at 1.47 GHz. This small sky-cold load difference means that even a (large) ±5% error in the measurement of the radiometer gain introduces less than ±0.010 K error into the difference. The nearest practical competitor to LHe, liquid nitrogen, has an ambient pressure boiling-point at ~73 K, so even an excellent ±1% measurement of the gain would introduce a ~±0.69 K error in the difference.

Second, when left to boil at ambient pressure the temperature is very well determined and stable. Lastly, LHe has a very small dielectric constant and does not significantly degrade the black-body properties of the absorber: the power reflection from the He-LHe transition is $< 1.1 \times 10^{-4}$.

Difficulties of using LHe include a very small heat of vaporization, high cost, and transporting the liquid to the remote locations where the measurements are made. The small heat of vaporization is partially offset by the large enthalpy of the gas. This is exploited by using the boiloff gas to decrease the heat leak to the LHe bath.

For measurements below 2.5 GHz, the primary calibration has historically been a major source of error, as was the case for the 1.41 GHz measurement of Levin *et al.* (1988). The cold load used for the 1.41 GHz measurement is described in Smoot *et al.* 1983 and in § I A of Appendix A. Briefly, the old cold load had a 20 thick absorber immersed in LHe with only two thin polyethylene windows covering the 70 cm diameter aperture. The radiative heat load was reduced by means of a movable shutter. The old cold

load was designed for the 2.5 to 90 GHz range. At 1.41 GHz, the absorber reflection was greater, and the joint in the radiometric wall associated with the shutter was not well understood.

Any improvement on the 1.41 GHz measurement required a better cold load calibrator. I spent the next 9 months designing, modelling and building a new cold load reference target which would be more suitable for operation in the 1 to 10 GHz range. The resulting cold load calibrator, its history, design, construction, radiometric modelling and testing are discussed in depth in Appendix A. Here, I only emphasize the main features, performance across the operating band, and the thermal and operational performance in 1988 and 1989.

The absorber is joined to the mouth of the cold load by a 78 cm diameter aluminum-foil-lined fiberglass cylinder. The aluminum is thin (25 μm), to minimize heat conduction down to the LHe bath, but thick enough to be less than $\sim 10^{-5}$ transparent at 1 GHz. The fiberglass wall serves as a structural support for the Al foil as well as the absorber and all of the level, temperature and pressure sensors.

Two sets of windows solve two separate problems. The first potential problem is condensation of atmospheric gases onto the cold radiometric surfaces. Two 23 μm-thick polyethylene windows with warm gas circulating in between and prevent condensation by maintaining the upper window at above ambient temperature.

The second problem is the large (50-200 W) radiative heat leak through the 4800 cm^2 cold load aperture which would result in a loss rate of 70-280 l/hr. It is well known that glasses are generally opaque in the infrared (IR) and become transparent in the microwave. A window made of glass would absorb the IR heat load (before reaching the LHe bath) and have minimal emission in the microwave. Glass becomes brittle at low temperatures and must be encapsulated in a supporting material to be useable as a large window. Teflon was chosen for its low temperature flexibility and low loss in the microwave. I found a Teflon-impregnated glass cloth material manufactured by Fluorglas

which was inexpensive and had the right dimensions (38" width and ~70 μm thickness). The drawback was that the glass was woven (a thin film would be ideal). However, Fourier spectrometer measurements of the reflection and transmission properties from 100-1000 cm^{-1} with the Fluorglas at 300 K and at 4.2 K showed that, for three layers, only between 2% and 5% of the the leak would be transmitted.

Although similar to the cold load used in our 1986 measurement, the new cold load incorporates several changes important to calibration at 1.5 GHz. The most important changes are: 1) thicker absorber resulting in lower absorber reflection at 1.5 GHz, 2) fewer discontinuities in the radiometric wall for lower emission, 3) capability of stable calibration for periods sufficient to study systematics and take data, and 4) complete and precise measurement of the radiometric wall temperature profile, LHe level and pressure over the LHe bath.

The performance across the operating band for a typical radiometer is shown in Figure 3.4. (The exact performance depends on the radiometer bandwidth, beamsize, antenna dimensions, and broadcast noise temperature.) Towards the low end of the operating range the signal increases because the absorber appears more transparent and the coupling to radiometric wall emission increases. Towards the high end of the operating range, the ratio of thickness to wavelength increases and the window reflection and emission increase causing a larger signal.

CL construction and LHe testing were completed at LBL in July 1988. The CL was then taken to White Mountain and used for measurements at 1.47, 3.8, and 7.5 GHz in September 1988. The CL operated very well and, after several minor improvements, was shipped to the South Pole nine months later.

The cold load arrived in good condition at the South Pole. As I transferred liquid nitrogen into the cold load, the dewar pressure began to rise. This is the opposite of what should happen: as the getter in the dewar vacuum space cools and begins cryopumping, the

pressure should drop. The leak was real, large, and on the inside of the bucket dewar, probably due to one of the four epoxy joints in the neck tube.

The repair plan was the following: pull the radiometric part of the cold load out of the dewar and apply epoxy to all the joints. The radiometric part of the cold load consists of the radiometric wall, the interface at the top, the windows, and the absorber (see Figure 1 in the Appendix). The radiometric part is ~55" long, weighs ~250 lbs, has delicate sensors on its exterior, and clears the neck tube of the bucket dewar by less than 3 mm per side. The next morning, Steve Levin, our fearless leader at the Pole, lead in the construction of an A-frame over the cold load. This Cadillac of A-frames had a plastic exterior (to keep the wind out and let the sunlight in) and rigging on the 4"x6" ridge pole to lift the radiometric part of the cold load. The next day, the radiometric part of the cold load was lifted out of the dewar, and, by the end of the day, the six 100" long glue joints had been cleaned and sealed with epoxy. After a night of curing with three heat lamps, the CL was reassembled, flushed with N_2 and prepared for liquid nitrogen. Less than four days from the time the first signs of the leak showed up, LN was in the CL and the dewar pressure dropped steadily until it was off-scale. Back in Berkeley, on the second thermal cycling of the epoxy patch, the leak reappeared when LN was tranferred into the cold load. This time the leak was so large as to be audible, and later inspection revealed a 6" long crack in the lower-most glue joint.

Beyond the improvements in the low-frequency radiometric performance, the new cold load is a pleasure to operate. Just ask anybody who got stuck with the job of operating the shutter on the old cold load on a cold, windy night, as they applied grease to the slide and struggled to ram the shutter all the way open for a quick look at the load. Or maybe, if those people have blanked the shutter from their minds, ask them about the half day of work to replace the polyethylene windows, only to find that there were large gas leaks and that the job had to be repeated. Another memory I have are the long days

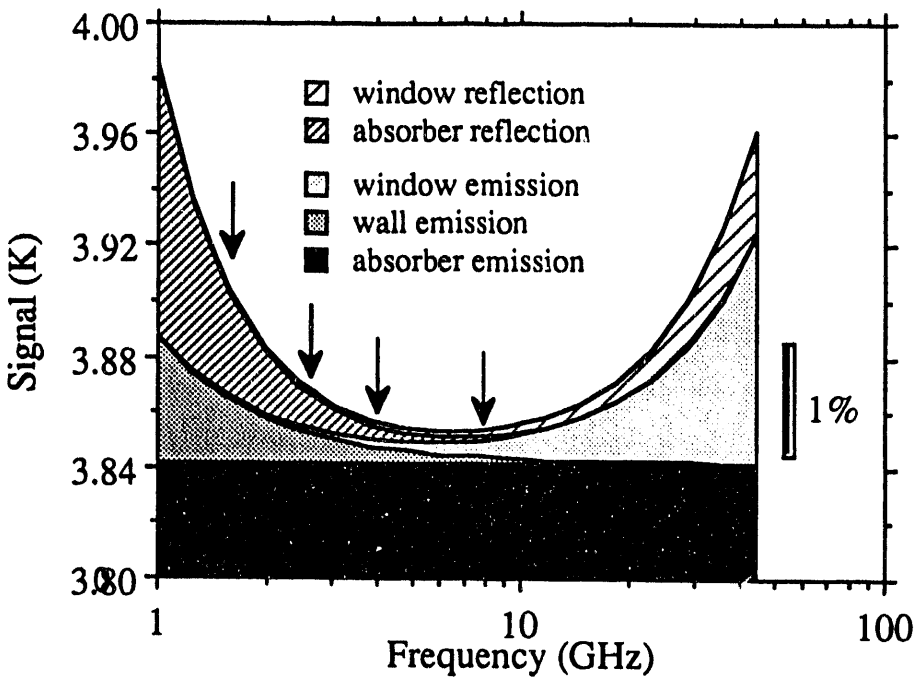

Figure 3.5 Cold load calibrator signal

required to ready the old load for LHe, and, once we had LHe in the load, the panic that set in to take data before the helium was gone.

With the new CL, it's a pleasure to change the polyethylene windows indoors (if they need to be changed at all), to never have gas leaks, to spend only a few hours a day for three or four days to ready the load for LHe, to fill the CL with LHe once a day, and to have the time to think about the measurements while there is LHe in the CL.

Chapter 4 The Observations

The choice of observing sites is critical to precise measurements. The RFI emissions associated with populated areas require a remote site. The ground signal is greatly reduced by low sidelobe response and shielding of the antenna, but a low horizon is needed to reduce the signal to an acceptable level. The magnitude of atmospheric emission and the characteristic roll-off frequency of the emission both decrease with altitude necessitating a high-altitude site. A region of sky with minimal galactic emission is needed overhead during the observations. Other important considerations in the site selection are the availability and quality of electric power, logistical support, and living conditions.

CMB observations were made from a wooden platform with the CL aperture at the level of the platform. The radiometer sat on its base to observe the sky and was physically inverted and the aperture placed on the CL interface plate to observe the CL. The observation cycle (Table 4.1) allows either 16 or 32 seconds to move from one target to another target and collect data. Moving the radiometer usually took less than 5 sec and if it took more than 8 seconds the data were not used.

During the CMB measurements, we used the smooth-walled pyramidal ground screen to avoid the unacceptably large signal (~0.6 K) due to ground emission with the antenna alone. The E-plane sides of the screen were equipped with quarter-wave traps to further reduce ground pick-up.

The radiometer gain coefficient and system temperature are measured by comparing the ambient calibrator signal, $S_{ambient}$, with the cold load signal, S_{load}. From Equation 3.1,

$$G = \frac{T_{ambient} - T_{load}}{S_{ambient} - S_{load}} \tag{4.1}$$

and

$$T_{sys} = G\, S_{load} - T_{load}, \tag{4.2}$$

where $T_{ambient}$ and T_{load} are the ambient calibrator and cold load temperatures, respectively. During ambient calibration, the ambient calibrator is placed over the zenith-looking antenna aperture. Because all measurements made with the radiometer are differential (*eg.* Equations 2.1 and 5.5) the results are independent of the system temperature to first order.

A 1.5 m long extension was added to the antenna to make differential zenith scans; for these measurements, no absolute calibration was needed but very low sidelobes were essential. With the extension attached to the mouth, the HPBW was ~15° and the sidelobe response was <-60 dB at angles >90° (Witebsky et al. 1987).

Table 4.1 CMB observing cycle

Time (sec)[a]	32	16	32	16	16	16	16	16
Orientation	up	–[b]	down	down	–[b]	up	up[c]	up
Target	zenith	–	CL[d]	CL	–	WL[d]	–	zenith
Gain Scale	high	high	high	low	low	low	low	low[e]

[a] The second half of each 16 sec observing period is used in the analysis

[b] The radiometer is inverted in less than 16 sec

[c] The ambient target is removed and the ground screen placed on the antenna

[d] cold load (CL) and warm load (WL) targets

[e] high-gain scale at White Mountain

4.1 White Mountain 1988

We observed from the Nello Pace Laboratory of the University of California White Mountain Research Station (latitude 37.6° N, 3800 m altitude). The site lies on the eastern slope of a ridge which rises 18° towards the northwest; the horizon is lower in all other directions.

CMB observations were made at White Mountain during six separate runs on 18 and 19 Sep 1988 (UT). On 18 Sep, we experimented initially with a less optimal observation sequence, and for all three runs on 18 Sep, the ground screen did not have quarter wave traps and those data are not used in the CMB result. From here on, I will refer to the three runs on 19 Sep 1988 as runs 1, 2 and 3. The first run occurred when the galactic plane was nearly overhead (RA ~21^h) to gather data on galactic emission. The second and third runs observed regions of lower galactic emission (RA ~22^h - 2^h). During the June-September period when the site is accessible, the region of minimum galactic emission (at 38° declination) is overhead during the daytime and we cannot make observations. Differential galactic scans at ±15° in the East-West plane were made on 4 nights. During the same period, we made CMB, atmospheric and galactic measurements at 3.8 and 7.5 GHz, and atmospheric measurements at 90 GHz.

During each CMB measurement cycle, the radiometer measures the zenith-cold load difference on high gain, then measures the high-gain to low-gain ratio (observing the CL) and finally calibrates in low gain. This measured the low gain once and the zenith-cold load temperature difference once. The gain ratio was measured by taking the ratio of the low-gain cold-load signal to the high-gain cold load signal.

The differential galactic scans were made by tipping the radiometer 15° to the east of the zenith for 32 sec, then 15° to the West for 32 sec. During the first 16 sec of each period, the YIG filter was tuned to 1.375 GHz, while during the second half the filter was

tuned to 1.550 GHz. This cycle was repeated for the duration of a run and interrupted every hour for gain calibration.

The White Mountain group in 1988 consisted of Al Kogut, Steve Levin, and myself who stayed the for the entire expedition, Marco Bersanelli (who flew in from Italy just for these measurements), John Gibson, George Smoot, Giovanni De Amici, and short visits from Jon Aymon, Jay Levin, Larry Levin, Luis Tenorio, and Chris Witebsky. During the same period, we also made CMB, atmospheric and galactic measurements at 3.8 and 7.5 GHz.

4.2 South Pole 1989

These measurements were made from a site 1.8 km from the Amundsen-Scott Research Station (latitude 90° S) at the geographic South Pole. Resting on 2.5 km of ice at an altitude of 2800 meters, the site had an ambient temperature ranging from -20° to -30° C at the time of the observations. Except for two small buildings and the apparatus at the site, the horizon was flat. The ice was a dielectric at an effective temperature of 225 ± 10 K.

The South Pole site offered a better horizon, lower ground temperature and lower galactic signal than the White Mountain site but the lower altitude resulted in a larger atmospheric signal. We used the same ground screen as at White Mountain, and erected a 5 m high screen to reduce solar radiation. Solar radiation had to diffract over two sun-screen edges before reaching the ground screen.

CMB observations were made at the South Pole during five separate runs on 16, 17, 18 and 19 Dec 1989 (UT) during periods when the CL platform screen shielded the radiometer from solar radiation. In order to reduce the galactic signal, I tipped the radiometer away from the galactic plane during four of the five runs.

The same CMB observing cycle was used at the South Pole as at White Mountain except that each cycle measured the zenith-cold load difference temperature on both high

and low gain (see Table 4.1). The low-gain zenith-cold load difference is independent of the gain ratio and has a different dependence on post-gain electrical effects than the high-gain difference. This is useful to investigate radiometric problems.

The gain ratio was measured independently many times during the observations by placing a 3/4" sheet of plywood over the antenna and recording the high- and low-gain signal differences.

The South Pole group in 1989 consisted of Marco Bersanelli, Giovanni De Amici, John Gibson, Al Kogut, Michele Limon, Steve Levin, myself, and, from Milano, Giorgio Sironi, Giuseppe Bonelli, and Francesco Cavaliere. During the same period, the group from Berkeley made CMB, atmospheric and galactic measurements at 3.8 and 7.5 GHz and monitored atmospheric emission at 90 GHz. The group from Milano made CMB, galactic and atmospheric measurements at 0.82 and 2.5 GHz.

Chapter 5 Contributions to the Sky Temperature

5.1 The Atmosphere

For these measurements, the atmospheric emission at 1.47 GHz is determined by extrapolating from measurements at White Mountain and the South Pole at 3.8 GHz (De Amici *et al.* 1990, De Amici *et al.* 1991) and 7.5 GHz (Kogut *et al.* 1990, Levin *et al.* 1992). An attempt was made to measure atmospheric emission at 1.47 GHz by tipping the radiometer to correlate the signal with airmass. Uncertainties in the instrumental offset and the signal from the extension joint rendered these data useless.

The group has a long history of atmospheric measurements at higher frequencies (3.8, 7.5, 10, 33, and 90 GHz), and the atmospheric model is discussed extensively elsewhere (see for example Witebsky *et al.* 1986). Here I present only a brief outline of the measurement technique.

The atmospheric antenna temperature can be measured by comparing the antenna temperature of the zenith sky with the antenna temperature when the radiometer is tilted to a zenith angle *z*. The antenna temperature seen by a pencil beam at zenith angle z is:

$$T_{A,\,pen} = T_{kin}\left(1 - e^{-\tau h f(z)}\right) + T_{A,ext}\, e^{-\tau h f(z)} \qquad (5.1)$$

where T_{kin} is the effective kinetic temperature of the atmosphere, τ is the effective optical depth of the atmosphere, h is the atmospheric scale height , $T_{A,ext}$ is the temperature of the sources above the atmosphere and $f(z)$ is the path length through the atmosphere in units of the scale height, defined by:

$$f(z) = \frac{1 + \frac{h}{R}}{\sqrt{\cos^2(z) + 2\frac{h}{R} + \left(\frac{h}{R}\right)^2}} \tag{5.2}$$

where R is the Earth's radius. The O_2 scale height is ~7 km, so $h/R \sim 1.1 \times 10^{-3}$ and the difference between $f(z)$ and sec(z) at 40° is only 0.2% (a flat-slab model is a good approximation of the atmosphere). The signal is approximately:

$$S(z) = G^{-1} T_{A,pen} \sec(z) \tag{5.3}$$

and the atmospheric temperature for a pencil beam is:

$$T_{A,pen} = G \frac{S(z) - S(0)}{\sec(z) - 1} . \tag{5.4}$$

The discussion so far only applies to the pencil beam atmospheric signal. For an arbitrary beam, the signal is the convolution of the beam pattern with $f(z)$:

$$T_{A,atm}(z) = T_{A,pen} \int_{atm} f(z)\, G(\theta,\phi)\, d\Omega \equiv T_{A,pen} \langle f(z) \rangle \tag{5.5}$$

For small angles, the denominator in Equation (5.1) is large and any uncertainty in the signal difference is amplified. For a pencil beam, the zenith angles of 30° and 40° multiply the signal difference by 6.5 and 3.3, respectively. These angles provide a compromise between large amplification of errors for angles of less than 30° and increased signal (and error) from ground emission for angles greater than 40°.

Atmospheric tip scans were performed at 1.47 GHz at the South Pole in an attempt to measure atmospheric emission directly. At 1.47 GHz, the differential galactic signal is known to ±0.05 K (Reich and Reich, 1986), so the galactic subtraction would add ~±0.23 to the error in the measured atmospheric signal. Other errors arise from the instrumental offset, ΔT_{inst}, ground emission correction (~±0.03 K) and beam pattern errors.

However, because there was leakage through the extension joint and there was no precise measurement of ΔT_{inst}, the scans did not yield useful data.

For the receivers operating at 3.8 and 7.5 GHz, the sidelobe response is lower and the instrumental offset can be measured more precisely. In addition, at these higher frequencies the galactic signal is much smaller (by a factor of nearly 14 at 3.8 GHz). The total uncertainty in the measurements at these frequencies is ~±0.06 K. Provided we can extrapolate down to 1.47 GHz without adding significant uncertainty, the higher frequency measurements yield a more precise determination of $T_{A,atm}$ at 1.47 GHz than a direct measurement.

The atmospheric signal at 1.47 GHz at our sites is due to resonant and non-resonant emission by the complex of pressure-broadened oxygen lines clustered near $\nu_0 = 60$ GHz. The amplitude of the O_2 emission depends on atmospheric pressure and temperature and varies slowly with time. Emission from the water line at 22 GHz contributes negligibly at both sites (Danese and Partridge, 1989) and, for scaling purposes, the atmosphere is dry. Over the range $1 < \nu < 10$ GHz, in the simple, dry-atmosphere model of Gordon (1967), the attenuation, α (dB/km), scales approximately as:

$$\alpha = A\gamma \frac{x(1 + 3x)}{g(1 - 3x)^2 + x(1 - x)^2}, \tag{5.6}$$

where $x = (\nu/\nu_0)^2$, $g = (\gamma/\nu_0)^2$, and γ is the pressure- and temperature-dependent line-width parameter for oxygen. Leibe (1985) reports:

$$\gamma = 0.565 \left(\frac{300}{T}\right)^{0.8} p_d , \tag{5.7}$$

where T is the temperature of the air, p_d is the dry-air partial pressure in atmospheres, and the small contribution from water vapor is omitted. From our sites, $\gamma < 0.5$ GHz so that the roll-off in atmospheric emission occurs below 1.5 GHz.

We extrapolate the measured values according to Equation (5.3), propagate the error in each measured datum and include the uncertainty in the model parameter γ. The extrapolations from 3.8 and 7.5 GHz are in agreement at each site. $T_{A,Atm}$ is the mean value weighted by the uncorrelated measurement errors, with uncertainty given by the quadrature sum of the weighted measurement errors and the uncertainty in γ. The parameters used in the simple atmospheric model described by Equation (5.3), the higher frequency data and the resulting values for the atmospheric temperature for a pencil beam at 1.5 GHz are shown in Table 5.1.

The atmospheric emission seen by the radiometer is the obtained from the pencil beam result and $\langle f(z) \rangle$ according to Equation (5.3). Table 5.2 summarizes $\langle f(z) \rangle$ and $T_{A,Atm}$ results at 1.47 GHz for the two sites.

This simple extrapolation from values measured at nearby frequencies agrees well with the empirical atmospheric attenuation model of Danese and Partridge (1989). At 1.47 GHz at our sites, the dependence on water vapor content in the Danese and Partridge model is negligible (< 0.001 K/mm H_2O). Figure 5.1 summarizes the measured data, the two models and the calculated values at 1.47 GHz.

Table 5.1 Determination of the atmospheric temperature for a pencil beam

Quantity	White Mountain	South Pole	Units	Comments
Atmospheric temperature	240±10	235±10	K	Measured
Atmospheric pressure	480	520	Torr	Measured
γ	0.427±0.032	0.478±0.033	GHz	Calculated
precipitable water vapor	1.5	1	mm H_2O	Measured[a]
$T_{A,Atm}$(3.8 GHz)	0.921±0.055	1.070±0.060	K	Measured[b]
$T_{A,Atm}$(7.5 GHz)	1.037±0.055	1.161±0.060	K	Measured[c]
$\alpha_{1.5,3.8}$	0.921±0.042	0.907±0.040	—	Model[d]
$\alpha_{1.5,7.5}$	0.862±0.038	0.846±0.038	—	Model[d]
3.8 GHz datum scaled	0.849±0.064	0.970±0.069	K	Extrapolated[e]
7.5 GHz datum scaled	0.894±0.061	0.983±0.067	K	Extrapolated[e]
$T_{A,pen}$(1.5 GHz)	0.873±0.063	0.977±0.068	K	Extrapolated[f]
$T_{A,pen}$(1.5 GHz)	0.917	1.062	K	Model[g]

[a] Inferred from measurements at 90 GHz and the model of Danese and Partridge

[b] Value for pencil beam is 0.965 of the value measured with 16° HPBW

[c] Value for pencil beam is 0.961 of the value measured with 20° HPBW

[d] $\alpha_{\nu 1,\nu 2}$ is the ratio of atmospheric attenuation at ν_1 and ν_2 using Equation (5.3)

[e] Includes combined error from the Gordon (1967) model and the measured datum

[f] Weighted average of 3.8 and 7.5 GHz scaled data and the average of the errors

[g] From the model of Danese and Partridge

Table 5.2 1.47 GHz atmospheric emission

z (deg)	$\langle f(z) \rangle$	White Mountain (K)	South Pole (K)
0	1.071±0.022	0.935±0.070	1.046±0.076
15	1.114±0.024	—	1.088±0.080

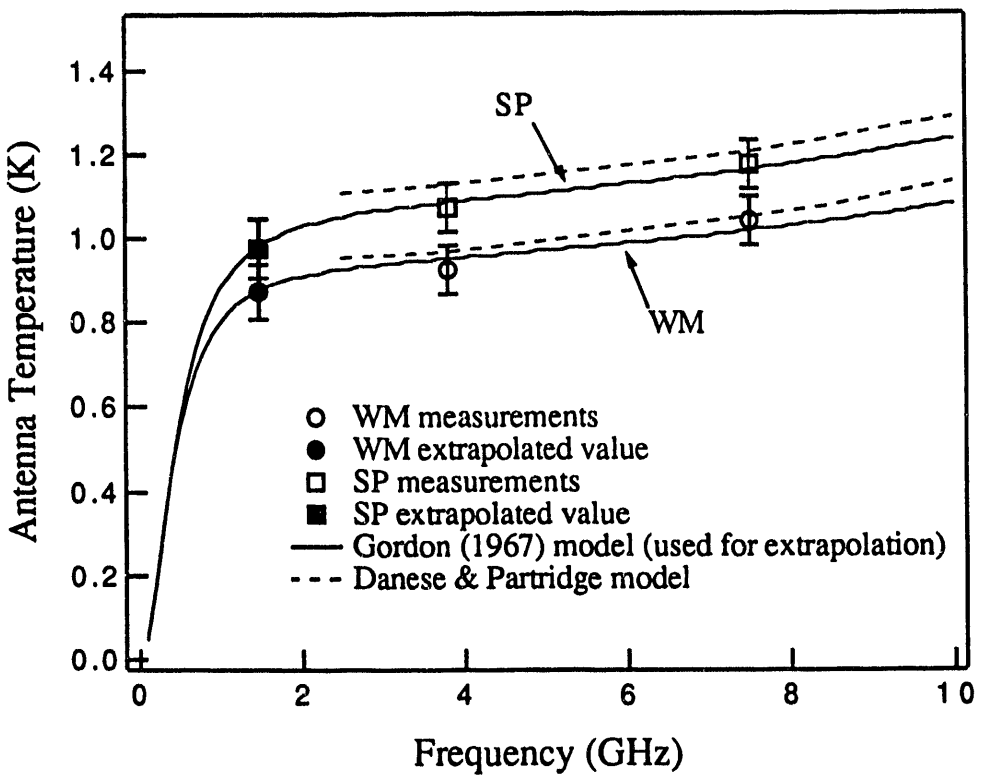

Figure 5.1. Atmospheric antenna temperature. The solid lines are the best-fit extrapolation from the measured data according to the model described by Equation (4). The data have been corrected for the finite beamwidth of each instrument.

5.2 Ground Emission

Ground emission enters the antenna side- and back-lobes, contributing to the zenith signal. We calculate the ground contribution by convolving the measured antenna beam pattern (Figure 3.3) with the ground. We take into account the surface reflection and temperature of the ground, and the horizon profile. The results are summarized in Table 5.3. The co-polarized response in between the E- and H-planes is generally lower than in the E- or H-planes, resulting in a correction by a factor of 0.87 ± 0.13 to the ground signal at both sites. Other uncertainties (and the uncertainty in the quantity) arise from the horizon elevation profile ($\pm 2^{o}$), the HPBW of the gain pattern ($\pm 2^{o}$), the relative gain of side- and back-lobes ($\pm$1dB), and the cross-polarized response (> -20dB).

We set a lower limit on the ground contribution from measurements of the residual ground radiation which can be blocked out. The tests consist of shielding the aperture edge from ground radiation incident from below (diffraction test), extending the reflecting surface of the shield or extension (extension test) or covering part of the ground with a reflector. Because both the ground screen and extension have quarter-wave traps at the aperture on the E-plane sides, we expect that extension chop tests will block out less ground radiation than diffraction chop tests. For a detailed discussion of the techniques we use to measure sidelobe reception see Kogut *et al.* (1990).

5.2.1 White Mountain

The ground at the White Mountain site is dry, rocky and rough on the scale of a wavelength. We estimate the ground to be a grey body at 273 ± 3 K with emissivity of 0.9 ± 0.1 (Ulaby *et al.* 1981) and calculate $T_{A,ground} = 0.147 \pm 0.056$ K.

Diffraction tests set a lower limit on $T_{A,ground}$ with the antenna pointed at the zenith. We measured a signal of 0.040 ± 0.012 K in the H-plane in the direction of highest

horizon, and no signal at the ±0.010 K level on the E-plane sides. This sets a lower limit at 0.040 ± 0.012 K, consistent with the calculation.

5.2.2 South Pole

The surface at the South Pole is smooth and flat, consisting of dry, packed ice crystals. The surface ice density is 0.11±0.01 g/cm^3 which corresponds to a dielectric constant at the surface of ~1.7 (Ulaby *et al.* 1981). The density of the ice increases smoothly with increasing depth due to the increasing pressure. At depths ≥80 m the ice is non-porous and the dielectric constant is ~3.2. The optical depth of the ice is >100 m (Warren 1984) so that the effective ground temperature is ~225 K (the annual average temperature). Including the effect of polarized reflection from the surface (Jackson 1975) we estimate $T_{A,ground}$ = 0.059 ± 0.023 K and 0.089 ± 0.034 K at 0° and 15° zenith angles, respectively. The ground emission correction is smaller at the South Pole than at White Mountain due to the lower horizon, colder ground and higher reflectivity of the surface.

Diffraction tests of the horn and ground screen did not give useful results because of the large size of the shield required (1.2 x 2.4 m) and the wind conditions at the site.

Table 5.3 Estimated ground contribution for antenna with ground screen (K)

z (deg)	White Mountain	South Pole
0	0.147 ± 0.056	0.059 ± 0.023
15	—	0.089 ± 0.034

5.3 Orientation-dependent Offset

When the radiometer is inverted to observe the cold load and the zenith, its properties can change. Orientation-dependent changes in gain, system temperature, physical temperature, and characteristic reflection and insertion loss of the front-end of the radiometer can contribute to ΔT_{inst}. The radiometer signal, S, can be written as

$$S \approx \frac{1}{G}\left[T_{sys} + T_{A,load}(1 - R - L) + T_B R + T_R L\right] \tag{5.8}$$

where the radiometer is characterized by the system temperature T_{sys}, the antenna temperature of the load $T_{A,load}$, the effective reflection coefficient R, the effective insertion loss L, by the broadcast noise temperature T_B, and the effective physical temperature of the lossy components T_R. The change in output when the radiometer is inverted with a fixed load attached to the aperture is given by:

$$\Delta T_{inst} = G\,\delta S \approx \delta T_{sys} + \delta T_B\, R + \delta T_R\, L$$

$$- \frac{\delta G}{G}(T_{sys} + T_{A,load}) + \delta R\,(T_B - T_{A,load}) + \delta L\,(T_R - T_{A,load}), \tag{5.9}$$

where second order terms have been dropped in the gain-change term. The first three terms are independent of $T_{A,load}$ while the last three terms (gain, reflection, and insertion loss) are linearly dependent on $T_{A,load}$. Measurements of ΔT_{inst} at 7.5 GHz, where a cryogenic load was available, showed an effect which was linear in $T_{A,load}$ (Levin *et al.* 1992).

The temperature differences in the last two terms determine the sensitivity of a particular test to δR and δL. For the 1.47 GHz radiometer, $T_{A,load} >> T_{sys} \approx T_B$ and $T_{A,load} \approx T_{ambient} \approx T_R$ (the equilibrium situation), ΔT_{inst} is very sensitive to δR but it is independent of δL. A precise measurement of δL requires a load temperature far from ambient; a cooled target decreases the extrapolation error.

We needed to evaluate ΔT_{inst} for $T_{A,load} = T_{A,sky}$, but were unable to build a stable, invertible, cryogenic target of such large aperture size. ΔT_{inst} was measured by securely attaching the ambient calibration target to the antenna aperture and inverting the radiometer. The ambient target was stiffened and insulated so that its properties would not change during these tests. Tests of the target itself showed no change in the reflection coefficient when inverted.

At White Mountain we performed tests with the load at ambient temperature (275 ± 2 K). We subsequently mounted a heater on the load and at the South Pole we measured the effect with load temperatures in the range 244 to 330 K. After returning to Berkeley, we modified the target further and performed tests with the load in the range from 223 to 331 K.

Figure 5.2 shows the results of the tests performed with 32 or 64 sec periods plotted versus load temperature. The three data sets are in agreement, showing no significant change in the effect from site to site. There is no significant dependence on $T_{A,load}$. The statistical errors on the individual tests (typically 0.01 K) are smaller than the scatter probably due to non-repeatable mating of the target to the antenna aperture. The least-squares linear fit using only the statistical error on each datum, yields an extrapolated value at $T_{A,load} = 4$ K of -0.009 ± 0.013 K. The fit is poor ($\chi^2 = 284$ for 16 D.O.F.) because the statistical error on each datum is less than the ~0.03 K rms scatter in the data. If we increase the average uncertainty on the test data to 0.03 K (a factor of 4.2 increase) to account for this scatter, we obtain $\Delta T_{inst} = -0.009 \pm 0.061$ K and $\chi^2 = 16$ for 16 D.O.F. (plotted in Figure 5.2). If the outlying result, -0.069 ± 0.006 K, is not included the estimated mean increases by 0.011 K. This test result could be due to an insecure attachment of the load to the antenna.

The 32 and 64 sec tests were sensitive to changes in the terms in Equation (5.9) which occurred as the radiometer was inverted but were insensitive to instrumental effects caused by slow thermal gradients. To measure thermal effects, we attached the ambient

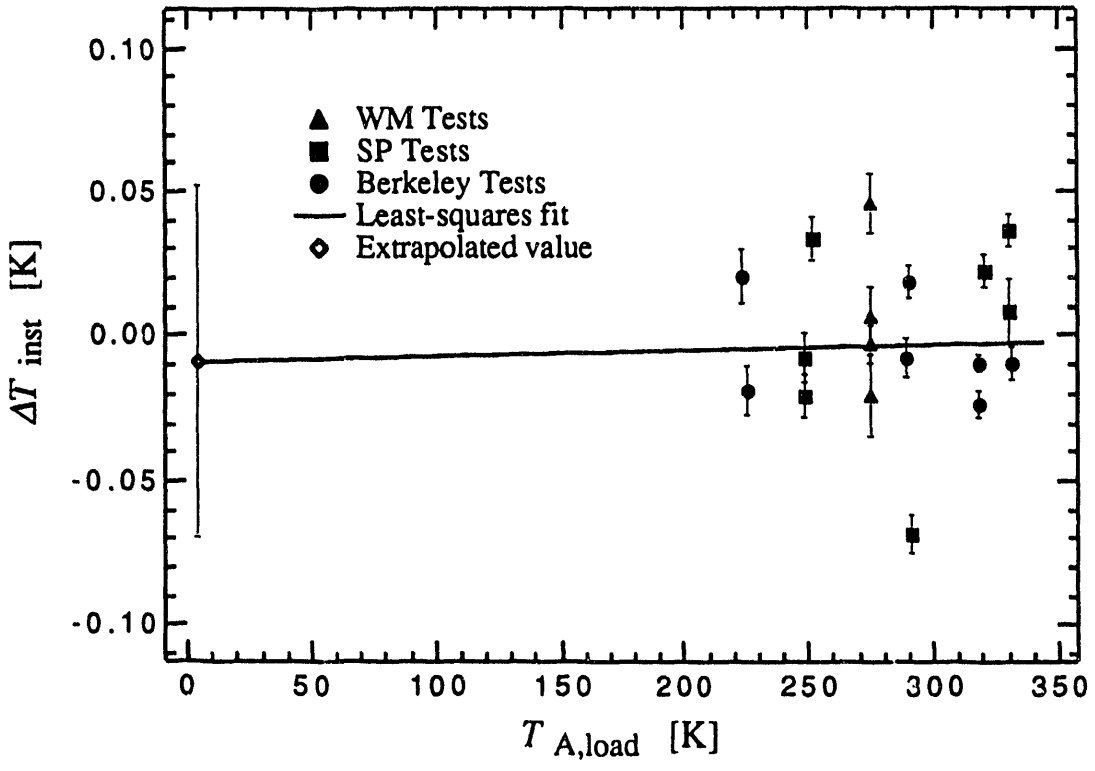

Figure 5.2. ΔT_{inst} versus $T_{A,load}$ for tests done at WM (triangles), the SP (squares), and Berkeley (circles). The least-squares fit line is drawn with the filled circle is the effect at $T_{A,load}$ = 4 K (see text for discussion of the error).

temperature target to the antenna and inverted the radiometer at the 160 sec period of the CMB measurement. The data, analyzed as if they were CMB measurements, showed $\Delta T_{inst} = 0.037 \pm 0.004$ K (Table 5.4). If this effect were due solely to gain variation, it would contribute 0.007 ± 0.001 K to the measurement. If this effect were due to any combination of variation in T_{sys}, T_B, or T_R, it would contribute 0.037 ± 0.004 K to the CMB measurement. Since we cannot distinguish between these possibilities, we adopt the average value 0.022 ± 0.015 K for thermal effects. Added to the extrapolated value discussed previously, we obtain $\Delta T_{inst} = +0.013 \pm 0.063$ K.

Table 5.4 Results of 160 sec period ΔT_{inst} tests

Test Location	Number of cycles	$T_{A,load}$ (K)	Effect (K)
WM	10	275 ± 2	0.045 ± 0.012
SP	12	244 ± 5	0.035 ± 0.006
SP	6	246 ± 5	-0.026 ± 0.032
SP	10	251 ± 5	0.041 ± 0.008
			0.037 ± 0.004[a]

[a] Weighted mean and statistical error in the mean; rms = 0.033 K

5.4 RFI

Radiofrequency interference was a major factor in our choice of observation sites. We used a spectrum analyzer to search for and monitor continuous and pulsed RFI sources at both sites.

5.4.1 White Mountain

We examined the signal after the first amplifier and the 1.0-1.6 GHz bandpass filter of the radiometer. No RFI signals were observed over the bandwidth of the measurement to give an upper limit of 0.006 K due to a single spike. There was a very strong pulsed signal at 1.33 GHz which set the lower limit of our operating frequency range. The lower limit of the synthesized bandwidth was set at 1.375 GHz, giving >60 dB rejection of the source at 1.33 GHz; it contributed negligibly. If we assume 5 sources just at the limit of detectability, the 2 σ upper limit on RFI was 0.030 K. At White Mountain in 1988, $T_{A,RFI}$ = 0.00 +0.015/-0.000 K.

5.4.2 South Pole

We monitored RFI in 20 MHz bands with 1 kHz resolution over the measurement band using a separate widebeam horn and low-noise amplifier. In four of the ten bands we found only small spikes at the limit of our detection sensitivity of 5 x 10^{-4} K per spike. These total a maximum of ~ 0.005 K, or less for a duty cycle <1. In the 1.53 - 1.55 GHz band a source was observed during two of the three observations of that region. If this source was present during the measurements the scatter on the sky data would have been of order 0.3 K, inconsistent with the observed value of 0.05 K. Some of the vehicular traffic at the Station (1.8 km away) generated pulsed noise over a wide frequency range.

This was observable only when a vehicle was closer than ~0.1 km, and during observations there were no vehicles closer than 1 km. At the SP in 1989, $T_{A,RFI}$ = 0.000 +0.005/-0.000 K.

5.5 Cold Load

At 1.47 GHz, approximately 99% of the signal from the cold load comes from the microwave absorber submerged in LHe. The differential pressure over the LHe bath is monitored continuously and maintained at less than +1 Torr during observations. At the ambient pressures of the sites, the slope of the LHe boiling point curve is ~0.0018 K/Torr, so variations in the pressure lead to temperature variations of ~±0.001 K. A full discussion of all aspects of the CL is given in Appendix A.

Only two sets of windows come between the radiometer and the LHe-bathed absorber. The most significant of emission are the Fluorglas windows whose opacity near 1.47 GHz is $<2 \times 10^{-5}$. Their physical temperature is between 30 and 50 K, so the emission is ~0.001 K.

The total correction to the LHe bath temperature is 0.048 ± 0.023 K; the calibration introduces negligible error to the measurement. Table 5.5 summarizes the contributions to $T_{A,Load}$. $T_{A,Load}$ = 3.790 ± 0.023 K in 1988 and 3.854 ± 0.023 K in 1989.

Table 5.5 Contributions to the cold load temperature (K)

Quantity	White Mountain	South Pole
Barometric pressure (Torr)	485	520
$T_{Absorber}$ [a]	3.777 ± 0.002	3.842 ± 0.002
$T_{A,\,Absorber}$	3.742 ± 0.002	3.806 ± 0.002
Radiometric wall emission[b]	0.024 ± 0.016	
Window emission	0.001 ± 0.001	
Incoherent reflection	0.023 ± 0.015	
Coherent reflection	0.000 ± 0.008	
Total correction to $T_{A,Absorber}$	0.048 ± 0.023	
$T_{A,Load}$	3.790 ± 0.023	3.854 ± 0.023

[a] T_{LHe} data from Duriex and Rusby, 1983

[b] The corrections to $T_{A,Absorber}$ are the same in the two years

5.6 Joint Effects

Differences in the the joint between the horn antenna and the cold load interface plate and the joint between the horn and ground screen interface plate contributed to the observed sky-CL temperature. This contribution, $\Delta T_{A,joint}$, arose from three contributions: 1) differential emission from within the resistive metal to metal joints, 2) differential transmission (leakage) of ambient radiation through the joints, and 3) differential joint reflection. Each joint has emission, e, transmission, t, and reflection, r. The temperature of the load, T, including the effects of the joint is given by

$$T = (1 - e - t - r)\, T_{A,load} + e\, T_{joint} + t\, T_{ext} + r\, T_B$$

$$= T_{A,load} + e\,(T_{joint} - T_{A,load}) + t\,(T_{ext} - T_{A,load}) + r\,(T_B - T_{A,load}), \qquad (5.10)$$

where $T_{A,load}$ is the temperature of the load in the absence of joint effects, T_{joint} is the physical temperature of the joint, T_{ext} is the effective temperature of the radiation arriving at the joint from outside the joint, and T_B is the radiometer broadcast temperature. This expression neglects higher order terms in e, t, and r and coherent reflection. The contribution of the joint to the measurement is given by

$$\Delta T_{A,joint} = \delta e\,(T_{joint} - T_{A,load}) + \delta t\,(T_{ext} - T_{A,load}) + \delta r\,(T_B - T_{A,load}), \qquad (5.11)$$

where δe, δt, and δr are the differential coefficients. Equation 5.11 must be evaluated for $T_{A,load} \approx 4$ K (the value during the measurements). The properties of the cold load and extension joints and $\Delta T_{A,joint}$ were measured with the cold load absorber cooled by liquid nitrogen. The terms in Equation 5.10 were evaluated for the cold load joint.

The cold load joint emission was measured by inserting a 0.9 mil polyethylene sheet (the same as the CL windows) between the antenna and CL interface plate. The emission can also be measured by modulating the joint temperature. Neither of these tests unambiguously give the CL plate joint emission: inserting a thin polyethelyene sheet could have modified the joint and the joint temperature is difficult to modulate. Other tests (discussed below) indicate that the emission is on the order of 20 mK.

The cold load joint transmission was measured by placing pieces of LN-cooled absorber on the four sides of the antenna-CL joint so as to cover the joint. This measures $\Delta T = e\,\Delta T_{joint} + t\,\Delta T_{ext}$. The term which depends on the change in joint temperature is unwanted and can be reduced by looking for a step in the signal when the LN-cooled absorber is removed (not allowing time for the horn to warm up). The uncertainty in t comes from the uncertainty in the temperature of the LN-cooled absorber ($T_{A,load} \approx 105 \pm 25$ K) and uncertainty in the proportion of warm radiation blocked out, including the effects of absorber reflectivity and transparency ($\varepsilon \approx 50 \pm 25$ %). The power absorption coefficient is 0.18 cm^{-1} corresponding to absorption $\beta = 0.6 \pm 0.2$ for the 5 cm thick absorber used. The absorber reflectivity is estimated at 0.1 ± 0.05. We then calculate:

$$\Delta T_{ext} = \beta (T_{amb} - T_{A,load}) + r (T_{amb} - T_{A,load}) = 131 \pm 40 \text{ K}, \quad (5.12)$$

and the test result of $\Delta T = 43 \pm 10$ mK gives the joint transmission coefficient:

$$t = \Delta T / \Delta T_{ext} = (3.3 \pm 1.3) \times 10^{-4}. \quad (5.13)$$

The effect on the cold load temperature due to the cold load plate transmission is then $t (T_{ext} - T_{A,load}) = 0.043 \pm 0.028$ K.

A second method of measuring the transmission is to terminate the outside of the joint with a reflector, reflecting the cold CL signal back into the joint. This measurement is difficult to interpret due to the coherence of the signal reflected back in through the joint with the signal reflected back from the load.

A measure of the overall sensitivity of the output to the CL plate joint is the effect of modifying the H-plane joint gap. In the H-plane, the mating surfaces are not exactly parallel (the surfaces touch at the innermost part of the joint) and slight pressure applied to the joint closes the gap. The signal decreased by 0.044 ± 0.031 K when the joint was pressed closed. A thin (25 μm) polyethylene sheet was placed in between the mating surfaces to prevent any change in the joint loss. Without the polyethylene sheet in place, closing the joint increased the joint loss, resulting in a smaller net effect of ~0.027 K (implying a ~0.017 K increase in emission with the joint closed).

The net effect on the sky-CL measurement of joint emission and transmission was measured by observing the LN-cooled cold load through the ground screen plate and the cold load plate. Two effects were accounted for in this test. There was 0.033 K leakage through the four small gaps between the square ground screen plate sides and the round cold load aperture; these gaps were sealed during the test. The force applied to the joint affected the signal by ~0.01 K; more mating pressure decreased the signal of the LN-cooled cold load, probably due to reduced joint leakage. During observations with the cold load plate, the full weight of the radiometer rested on the plate; during observations of the ground screen plate, the equivalent weight of the ground screen was applied to the plate (this required some of the radiometer's weight to be taken off of the plate). The result of

this joint comparison test, after scaling the result to a 4 K load, was 0.016 ± 0.035 mK (decreases $T_{A,CMB}$). Because these tests were not performed with a LHe-temperature absorber and the system is difficult to model, the error on this result is doubled to account for modeling errors.

The above comparison of the ground screen and cold load plates does not take into account the cold load and sky reflection. The joint reflection was measured with a network analyzer (Figure 5.3). A timing gate measured only reflection from the coaxial-waveguide transition, the antenna and the antenna interface and joint. The gate excluded reflection from any part of the cold load or ground screen beyond the joint. The reflection by the joint interferes coherently with internal reflections of the broadcast signal. The unknown phase difference between the cold load and ground screen interface reflections introduced additional error into the result. Averaged across the measurement bandwidth,

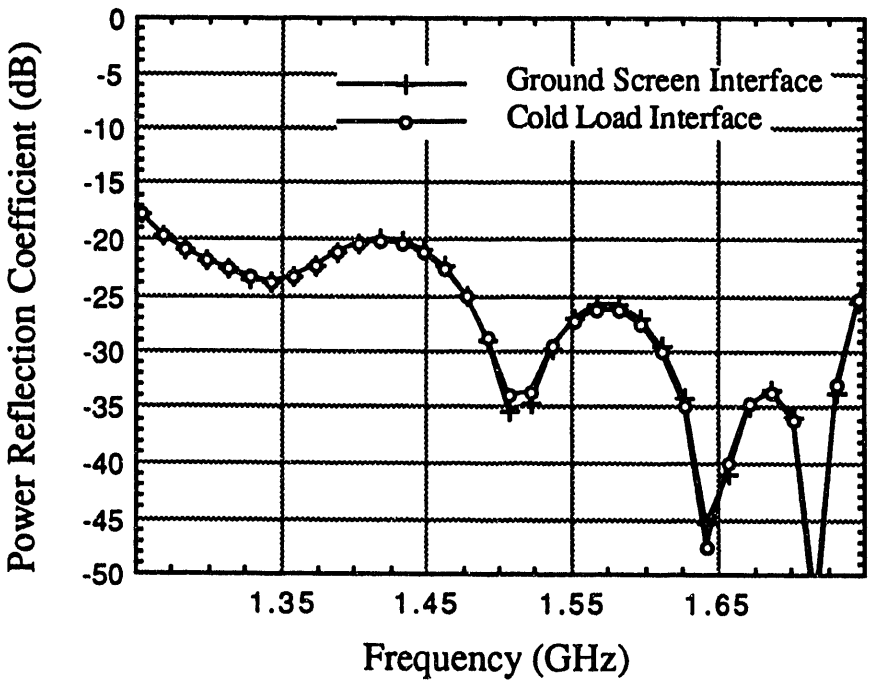

Figure 5.3 Transition, antenna and joint reflection.

the result is $\delta r = (1.7 \pm 1.5) \times 10^{-4}$ (more reflection from the ground screen interface). The correction for the measurement is r times $T_B - T_{A,load} \approx 50$ K, or 0.009 ± 0.008 K.

The variability of the transmission, emission and reflection effects contributed to the noise in the CL data at below the 0.06 K level. The total correction is the sum of the emission and transmission result, 0.016 ± 0.070 K, and the reflection result. It is the same for the two years (the joint was unchanged): $\Delta T_{A,joint} = 0.025 \pm 0.070$ K.

5.7 Solar Emission

The sun is a strong emitter at radio frequencies. We avoided solar emission at White Mountain by observing only at night. At the South Pole, the sun was ~23° above the horizon. We measured the solar antenna temperature on 12 Dec 1989 to be 69 ± 5 K in beam center, corresponding to an effective solar temperature of $\sim 3.4 \times 10^5$ K (for a 0.5° disk diameter). This is in agreement with predicted values of 1.3×10^5 K for the quiet sun to more than 10^6 K during outbursts (Allen, 1973).

During all CMB observations, the antenna was at a zenith angle from 0° to 15°, placing the sun at least 67° from the beam center where the antenna beam gain ($< 5 \times 10^{-5}$) reduced the signal to <0.004 K. The solar screen discussed in § III further reduced solar radiation. We adopt 0.004 K as a 68% CL upper limit on $T_{A,sun}$.

Chapter 6 The Sky Temperature

We calculate the zenith-cold load signal difference and the gain for each CMB measurement cycle. The gain was stable to better than 1% over all CMB observations and varied by less than 0.2% between any two cycles. We remove the linear component of the gain drift by linear interpolation between the cold load signal of adjacent cycles. We evaluate $T_{A,sky}$ using Equations 2.1 and 2.2 and the contributions evaluated in Chapter 5. The average value of the sky temperature during each run is given in Table 6.1 which also summarizes the terms in Equations 2.1 and 2.2.

6.1 White Mountain

The three runs have a total of 51 cycles; the data from 4 cycles are discarded because of errors in the observing sequence. Figure 6.1 shows zenith and CL raw data from WM run 3. The gain decreases by 0.5% at the start of the run and drifts slowly thereafter. The increasing difference between the zenith and CL signals towards the end of the run is due to increasing galactic emission.

Three effects cause noise in the data above the ±0.006 K system noise. Variation in pointing (due to wind) contributes ~±0.05 K of noise to the sky data due to sidelobe modulation of the galactic plane emission. The joint at the antenna aperture introduces scatter into the DC level of each observation ($\Delta T_{A,joint}$ is the average effect of the joint on the difference signal; see §5.6). An exponential upward drift in the sky data is evidence of a thermally induced increase in the gain or system temperature following the inversion of the radiometer. This effect has been accounted for by the 160 sec period ΔT_{inst} tests discussed in §5.3.

Table 6.1 Summary of White Mountain and South Pole sky and CMB data analysis [a]

Quantity	WM run 1	WM run 2	WM run 3	SP run 1	SP run 2	SP run 3	SP run 4
Time (UT)	19 Sep 1988 4:47-5:33	19 Sep 1988 6:16-6:57	19 Sep 1988 8:58-9:54	17 Dec 1989 5:02-7:00	18 Dec 1989 4:40-5:43	18 Dec 1989 8:02-8:46	19 Dec 1989 4:36-5:40
RA (h)	20.8-21.9	22.3-23.0	1.0-1.9	4.1-6.0	3.7-4.7	7.1-7.7	3.7-4.7
Zenith angle (deg)	0	0	0	15	15	0	15
No. of data points	16	11	19	43	22	14	23
$G(S_{zenith}-S_{load})$[a,b]	1.100±0.027	0.546±0.012	0.434±0.008	0.178±0.009	0.145±0.022	0.391±0.010	0.152±0.016
$T_{A,load}$	3.790±0.023	3.790±0.023	3.790±0.023	3.854±0.023	3.854±0.023	3.854±0.023	3.854±0.023
ΔT_{inst}	0.013±0.063	0.013±0.063	0.013±0.063	0.013±0.063	0.013±0.063	0.013±0.063	0.013±0.063
$\Delta T_{A,joint}$	0.025±0.072	0.025±0.070	0.025±0.070	0.025±0.070	0.025±0.070	0.025±0.070	0.025±0.070
$T_{A,zenith}$[c]	4.852±0.102	4.298±0.098	4.186±0.097	3.994±0.097	3.961±0.100	4.207±0.097	3.968±0.098
$T_{A,atm}$	0.935±0.070	0.935±0.070	0.935±0.070	1.088±0.080	1.088±0.080	1.046±0.076	1.088±0.080
$T_{A,gnd}$	0.147±0.056	0.147±0.056	0.147±0.056	0.089±0.034	0.089±0.034	0.059±0.023	0.089±0.034
$T_{A,sun}$	0.000±0.000	0.000±0.000	0.000±0.000	0.000±0.004	0.000±0.004	0.000±0.004	0.000±0.004
$T_{A,RFI}$	0.000±0.015	0.000±0.015	0.000±0.015	0.000±0.005	0.000±0.005	0.000±0.005	0.000±0.005
$T_{A,sky}$[a,c,d]	3.770±0.028 ±0.137	3.216±0.014 ±0.133	3.104±0.011 ±0.133	2.817±0.010 ±0.131	2.784±0.023 ±0.132	3.102±0.010 ±0.126	2.791±0.016 ±0.131
$T_{A,gal}$[a,c,d]	1.498±0.150 ±0.317	0.990±0.069 ±0.233	0.866±0.063 ±0.219	0.583±0.015 ±0.162	0.569±0.015 ±0.160	0.819±0.058 ±0.205	0.573±0.015 ±0.161
$T_{A,CMB}$[d]	2.271±0.152 ±0.346	2.226±0.070 ±0.269	2.238±0.064 ±0.257	2.235±0.018 ±0.208	2.215±0.027 ±0.208	2.283±0.059 ±0.241	2.218±0.022 ±0.208

[a] Average value during run

[b] Statistical error only; includes correction for atmospheric absorption

[c] Component polarized along lines of constant RA (towards the NCP for WM data; in the direction of the indicated RA for the SP data)

[d] The first entry is the error which is statistically uncorrelated from run to run (see Table 8.1); the second entry is the total error

$T_{A,sky}$ data for the White Mountain runs (Figure 6.2 (a)) show the decreasing contribution from galactic emission in the sky temperature data as the galactic plane moves further from beam center.

6.2 South Pole

There was an abrupt change in the zenith and cold load signals as well as a 0.13 K increase in their difference after the 18th cycle of the first set of data taken at the South Pole. Taken alone, the first part of this first data set would give a T_{CMB} 0.116 K lower than runs 1 to 4. The latter part of the first set of data is consistent with runs 1 to 4 to within the statistical errors. This data set is not included in the analysis; if included, it would decrease T_{CMB} by 0.009 K.

The four runs following the first observations have 103 cycles. Of these, we discard 7 of the high-gain data and 11 of the low-gain data points due to errors in the observing sequence. The high- and low-gain measurements of the sky temperature for each cycle agree to within the statistical errors. We use the average of the high- and low-gain data in the analysis. Figure 6.2 (b) shows data from the three runs at 15^{o} zenith angle.

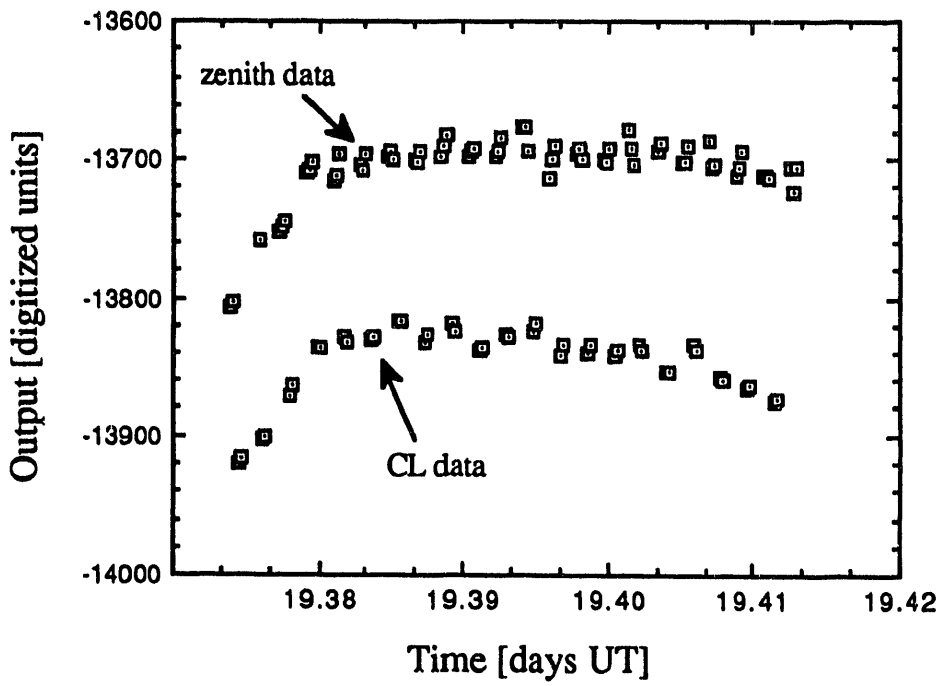

Figure 6.1. Raw high-gain zenith and CL data from WM run 6. Each point represents the average of four 2 sec data points. The radiometer high gain is ~3.0 mK/du. Gain calibration and low-gain CL data from each cycle are off-scale on this plot.

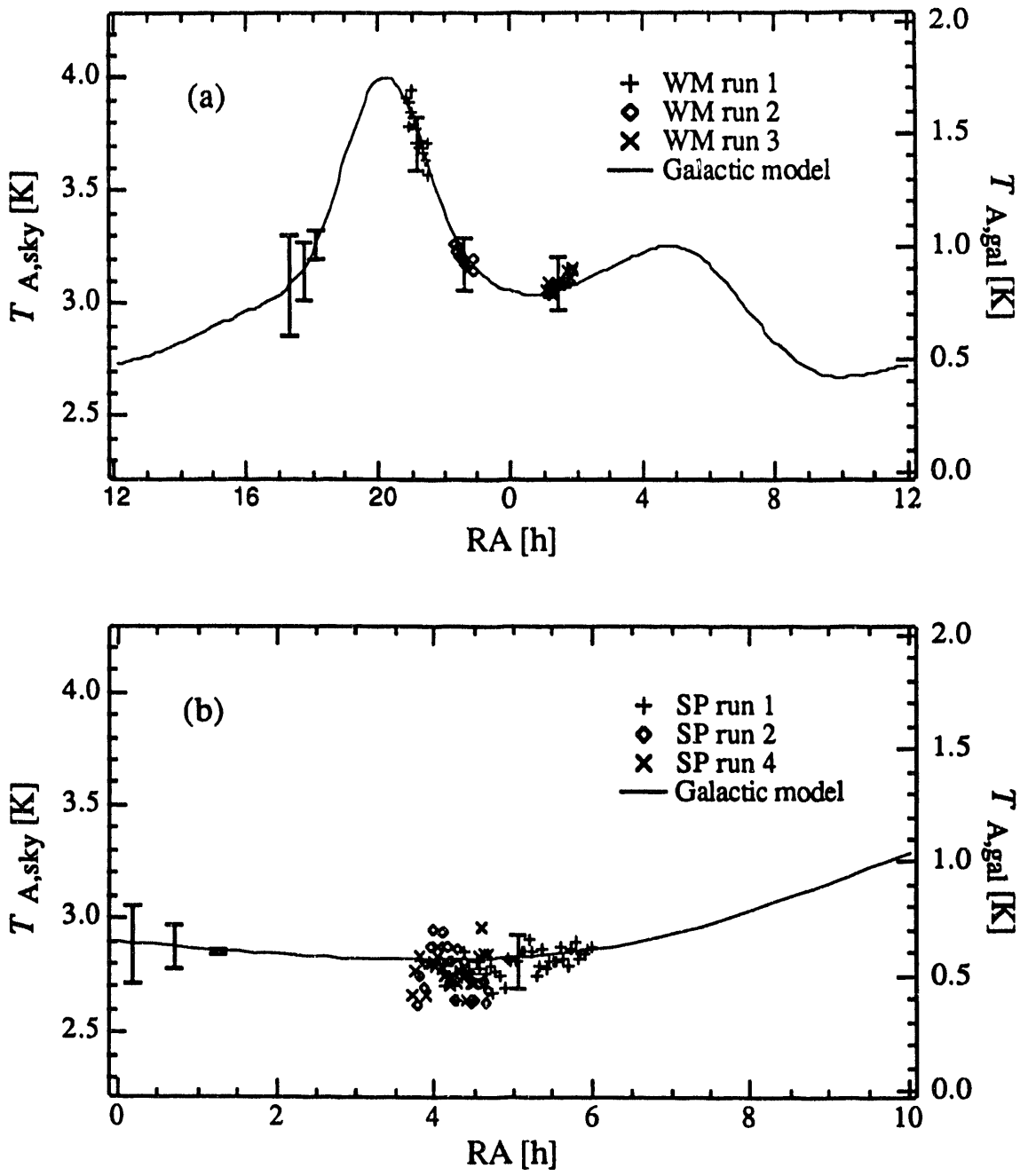

Figure 6.2. Measured antenna temperature of the sky (= $T_{A,CMB} + T_{A,gal}$), and the predicted galactic signal (see § VII). Each point is the sky temperature computed from one zenith-CL comparison measurement. Representative total error bars are shown for the measured data. The three error bars shown at the left on the galactic profiles are (l. to r.) estimates of the total galactic error, the part of the error which is uncorrelated from site to site, and that part which is uncorrelated from run to run (see Table 8.1). (a) All WM data; declination = 38°. (b) all SP data from runs at declination = -75°.

Chapter 7 Galactic Emission

Emission from the galaxy is the largest correction to the zenith data and the largest source of uncertainty in the measurement. Galactic continuum emission is spatially and frequency dependent, consisting of synchrotron radiation from cosmic ray electrons and thermal electron emission (HII emission). Significant HII emission is localized near the plane of the galaxy and has a spectral index of 2.1. Synchrotron emission is characterized by a spatially and frequency dependent spectral index α.

The emission from the blend of unresolved extragalactic radio sources is small compared to galactic emission (~10% for the observed regions) and has a spectral index of ~2.75 (Willis *et al.* 1977). This emission is generally not removed from galactic radio emission maps and we include it in the galactic signal in the analysis and discussion.

Table 6.1 lists the average galactic correction for each run.

7.1 The Galactic Model

We estimate the galactic signal using a 408 MHz skymap (Haslam *et al.* 1982) and a compilation of HII sources at 2.5 GHz. The 408 MHz map is first corrected for a CMB signal of 2.7 ± 1 K to allow for the possibility of up to a 1 K spectral distortion at 408 MHz. The 408 MHz map is then corrected for HII emission to avoid double counting. This is difficult for strong sources where the spectral index of 2.1 rolls off for $\nu \leq 1$ GHz due to self-absorption (Verschuur and Kellermann, 1974). I make the HII correction to the 408 MHz map by assuming that all of the emission scales to 1 GHz with a spectral index of 2.1 and remains constant from 1 to 0.408 GHz. Away from the plane of the galaxy (where the observations contribute significantly to the CMB result), the total correction for HII emission is ~0.005 K.

The corrected 408 MHz skymap and the HII map are convolved with the measured antenna gain pattern to produce a profile at the declination of each observation. These profiles are then scaled to 1.47 GHz using spectral indices of 2.75 ± 0.15 for the 408 MHz data and 2.1 for the HII data.

The galactic model is shown for a declination of 38° for the White Mountain observations (Figure 6.2 (a)), and for -75° declination for runs 1, 2, and 4 at the South Pole (Figure 6.2 (b)). The galactic signal at 408 MHz ranges from 46 to 25 K during the White Mountain observations and from 28 to 19 K for the South Pole observations.

7.2 Errors in the 408 MHz Map

The accuracy of the galactic model at 1.47 GHz depends primarily on the accuracy of the 408 MHz map and the accuracy of the spectral index used to scale from 408 MHz to 1.47 GHz. The 408 MHz full-sky map is a compilation of four different surveys. The map has overall errors of ±3 K in the zero level and ±10% in the gain. The zero level of the Northern Hemisphere is determined by comparison to the absolutely calibrated survey at 404 MHz of Pauliny-Toth and Shakeshaft (1962). The Southern Hemisphere zero level is based on a comparison of the equatorial band which overlaps with the Northern hemisphere surveys.

As a crosscheck of the zero level of the 408 MHz map at the South Celestial Pole (SCP), it was compared to an independent measurement by Price (1967). Using a pyramidal antenna with a 12.5° x 14° beam, Price measured the SCP brightness to be 23.9 ± 1.6 K. The 408 MHz map, integrated over Price's beam, yielded 24.4 K, 0.5 K above Price's result and well within the ±3.9 K combined gain and zero level errors in the 408 MHz map.

Although this agreement suggests that the error in the 408 MHz map have been overestimated (at least at the SCP), it is possible that Price underestimated several errors in

the measurement (*e.g.* from atmospheric emission, ground emission, or antenna emission). Therefore, the 408 MHz map (with the quoted errors) is used to obtain the galactic emission at 1.47 GHz, instead of the Price result.

7.3 Errors in the Spectral Index

The largest error in the galactic signal arises from uncertainty in the spectral index. We make a first approximation of the index from the ratio of the 408 MHz map and a map at 1420 MHz (Reich and Reich, 1986), after both have been corrected for the CMB signal. The result is $\alpha \approx 2.61 \pm 0.06$ for the regions observed at White Mountain where the errors given are statistical only. For the entire region covered by both maps, $\delta > -19^{o}$, $\alpha = 2.64 \pm 0.08$. The error on α due to the gain and zero level uncertainties on the maps at frequencies ν_1 and ν_2 is

$$\delta\alpha = \frac{1}{\ln(\nu_1/\nu_2)} \sqrt{\left(\frac{\delta T_1}{T_1}\right)^2 + \left(\frac{\delta T_2}{T_2}\right)^2} \tag{7.1}$$

where $\delta T/T$ is the relative error of the maps. For ≤ 4 K emission at 1420 MHz, the ± 0.5 K zero level error on the 1420 MHz map dominates the uncertainty in α. For WM runs 2 and 3 the total error on α is $\sim \pm 0.4$.

Lawson *et al.* (1987) attempt to improve the precision in the spectral index by a better determination of the zero level of the 1420 MHz map. They assume that, for a region of low galactic emission near the North Celestial Pole, the spectral index is frequency-independent and has a value determined by the 408 MHz map and a lower frequency map at 38 MHz. They adjust the zero level of the 1420 MHz map by -0.13 K to fit the constant spectral index in the region of minimum emission. For WM runs 2 and 3, the Lawson corrections give $\alpha \approx 2.71 \pm 0.05$ (statistical error only). This procedure exploits the small ($\leq 25\%$) relative zero level errors on the 408 and 38 MHz maps

(compared to the ≥100% error on the 1420 MHz map) in the region of low emission, but it relies on the assumption of a constant spectral index. Lawson's method yeilds an improved mean value for α, but does not decrease the error on α. If the constant spectral index assumption is valid (and the error on the 1420 MHz map no longer contributes to the error), the total error on α would be ±0.13 (from the 408 MHz map).

The spectral index can also be estimated by comparing differences in the galactic signal at 408 MHz and at higher frequencies. We measured the differential galactic signal at White Mountain by scanning the radiometer (mounted on the extension) ±15° from the zenith in the E-W direction. The data are plotted in Figure 7.1 with statistical error only. The least-squares fit to the data yields a synchrotron index $\alpha = 2.90 \pm 0.02$ (statistical error only) and with offsets of 4° in RA and 0.05 K in the difference signal. The low confidence level of the fit (χ^2 = 127 for 27 D.O.F.) and the 0.05 K signal offset are evidence of an instrumental effect (*e.g.* radiation leakage through the joint between the antenna and extension).

Differential galactic scans at 3.8 and 7.5 GHz at White Mountain and at 3.8 GHz at the South Pole are consistent with a synchrotron spectral index of 2.75 for $0.4 < \nu <$ 7.5 GHz (see, for example, De Amici *et al.* 1991 for a plot of ±30° zenith scan data from the South Pole).

The three estimates of the spectral index are 2.64, 2.71 and 2.90 and I take the spectral index of synchrotron radiation (for $0.4 < \nu < 1.5$ GHz and for the regions of the sky observed) to be their average, 2.75, with an error of ±0.15 to include the three estimates.

7.4 Other Errors in the Galactic Signal

Table 7.1 summarizes the sources of error in the galactic signal for the region observed during WM run 6. The 408 MHz and HII maps are total intensity maps whereas we only measure one linear polarization. We use the measured polarization (Brouw and Spoelstra, 1976) of the region of sky observed at White Mountain, integrated over the main lobe of the beam to correct the total intensity profiles. There are no published data of the polarization for the SCP region, but we can use the fractional polarization at White Mountain as a guide: the largest fractional error is 7% for run 3. For a random polarization angle, we obtain 0.000 ± 0.027 K for the SP runs 1, 2, and 4 (the uncertainty is slightly larger for SP run 3).

Price (1969) measured one linear polarization component of the SCP brightness at 408 MHz and observed a 0.5 K diurnal variation in the signal, attributed to differential modulation of the galactic plane by the elliptical beam. If the variation were entirely due to galactic polarization, it would scale to 0.015 K at 1.47 GHz. We adopt the larger value with a random polarization angle for the South Pole.

Other sources of error in the galactic signal are the uncertainty in the center frequency, the beam pattern, the pointing direction, and in HII emission (which we conservatively estimate at ±50%).

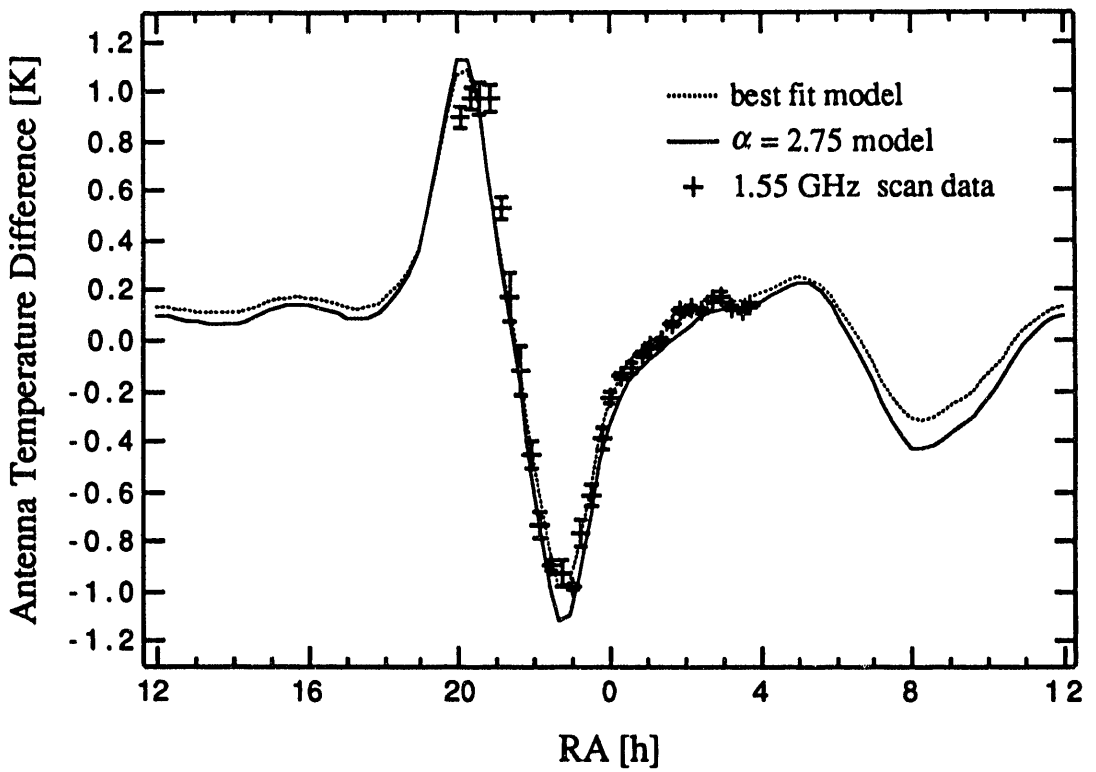

Figure 7.1. ±15° galactic zenith scan data and model. The data are shown with statistical error bars only. The solid line is the profile predicted from the model discussed in the text. The dotted line is the result of a least-squares fit with the synchrotron spectral index (best-fit value = 2.90), the vertical offset (+0.050 K) and the horizontal offset (-4°) as free parameters.

Table 7.1 Sources of error in the modeled galactic signal (K) [a]

Source	Uncertainty in Source	Error at 1.47 GHz
CMB correction to 408 MHz map	± 1 K	± 0.029
408 MHz map zero level	± 3 K	± 0.088
408 MHz map gain	± 10%	± 0.086
Spectral index	± 0.15	± 0.166
Polarized emission	± 10° angle, ± 0.03 K intensity	± 0.033
Beam pattern	± 2° angle, ± 1 dB gain	± 0.020
Center frequency	± 5 MHz	± 0.016
Pointing	± 2°	± 0.053
HII emission	± 50%	± 0.002
Total (added in quadrature)		± 0.219

[a] Calculated for total galactic emission during WM run 3; see text for an explanation of the uncertainties.

Chapter 8 CMB Results

We remove $T_{A,gal}$ from the zenith sky temperature to obtain $T_{A,CMB}$ as summarized in Table 6.1. The uncertainty is dominated by systematic effects which are largely correlated from run to run or from site to site. Tables 6 and 8 indicate the correlated and uncorrelated uncertainties. The run to run uncorrelated error and the total error are given for $T_{A,sky}$, $T_{A,gal}$, and $T_{A,CMB}$ in Table 6.1. An estimate of the magnitude of the uncorrelated component of the error for each term entering into the CMB result is shown in Table 8.1.

The results from the three White Mountain runs and the four South Pole runs are consistent with each other (see Table 6.1) to within the small part of the error which is statistically uncorrelated from run to run. Figures 8.1 (a), (b), and (c) show stacked histograms of the CMB data for the White Mountain runs, the South Pole runs and the combined data sets, respectively. The additional statistical noise in the South Pole data is due to an electrical problem in the receiver (§3.1) and possibly to a degredation of the joint at the antenna aperture (and the repeatability.of the mating).

The average, weighted by the uncorrelated part of the error of each run, gives a CMB antenna temperature of 2.24 ± 0.25 K for the White Mountain data set and 2.23 ± 0.21 K for the South Pole data set. The error is the quadrature sum of the statistical spread in each data set and the smallest total correlated error from each data set. Converting to thermodynamic temperature, we obtain:

$$T_{CMB} = 2.27 \pm 0.25 \text{ K} \qquad \text{(White Mountain 1988)}$$

$$T_{CMB} = 2.26 \pm 0.21 \text{ K} \qquad \text{(South Pole 1989).}$$

Combining the results from the two years, weighting by the part of the error which is uncorrelated from site to site, we obtain:

$$T_{CMB} = 2.27 \pm 0.19 \text{ K} \qquad \text{(1988 and 1989 combined).}$$

Table 8.1 Uncorrelated part of errors in the measurements (K) [a]

Source of error	WM Run 3			SP Run 4		
	Total error	uncorrelated error		Total error	uncorrelated error	
		run-run	site-site		run-run	site-site
$G(S_{zenith}-S_{load})$[a]	0.008	0.008	0.008	0.016	0.008	0.008
$T_{A,load}$	0.023	0.002	0.002	0.023	0.002	0.002
ΔT_{inst}	0.063	0 [b]	0.011	0.063	0	0.011
$\Delta T_{A,joint}$	0.070	0	0.035	0.070	0	0.035
$T_{A,atm}$	0.070	0	0.049	0.080	0	0.063
$T_{A,gnd}$	0.056	0	0.032	0.034	0	0.010
$T_{A,sun}$	0.000	0	0	0.004	0	0.004
$T_{A,RFI}$	0.015	0.007	0.015	0.005	0.002	0.005
$T_{A,gal}$ [c]	0.219	0.063	0.129	0.161	0.015	0.092
CMB correction to 408 MHz map	0.029	0	0	0.029	0	0
408 MHz map zero level	0.088	0	0.029	0.088	0	0.029
408 MHz map gain	0.086	0.020	0.043	0.057	0	0.040
Spectral index	0.166	0.045	0.100	0.109	0	0.066
Polarization	0.033	0.030	0.033	0.027	0	0.027
Beam pattern	0.020	0	0	0.020	0	0
Center frequency	0.016	0	0	0.011	0	0
Pointing	0.053	0.026	0.053	0.030	0.015	0.030
HII emission	0.002	0.002	0.002	0.003	0	0.003

[a] The error breakdown is given for one of the runs at each site.

[b] A zero entry indicates that that we take none of the error to be uncorrelated.

[c] The sources of uncorrelated error in the galactic signal are given; values represent the average during the run.

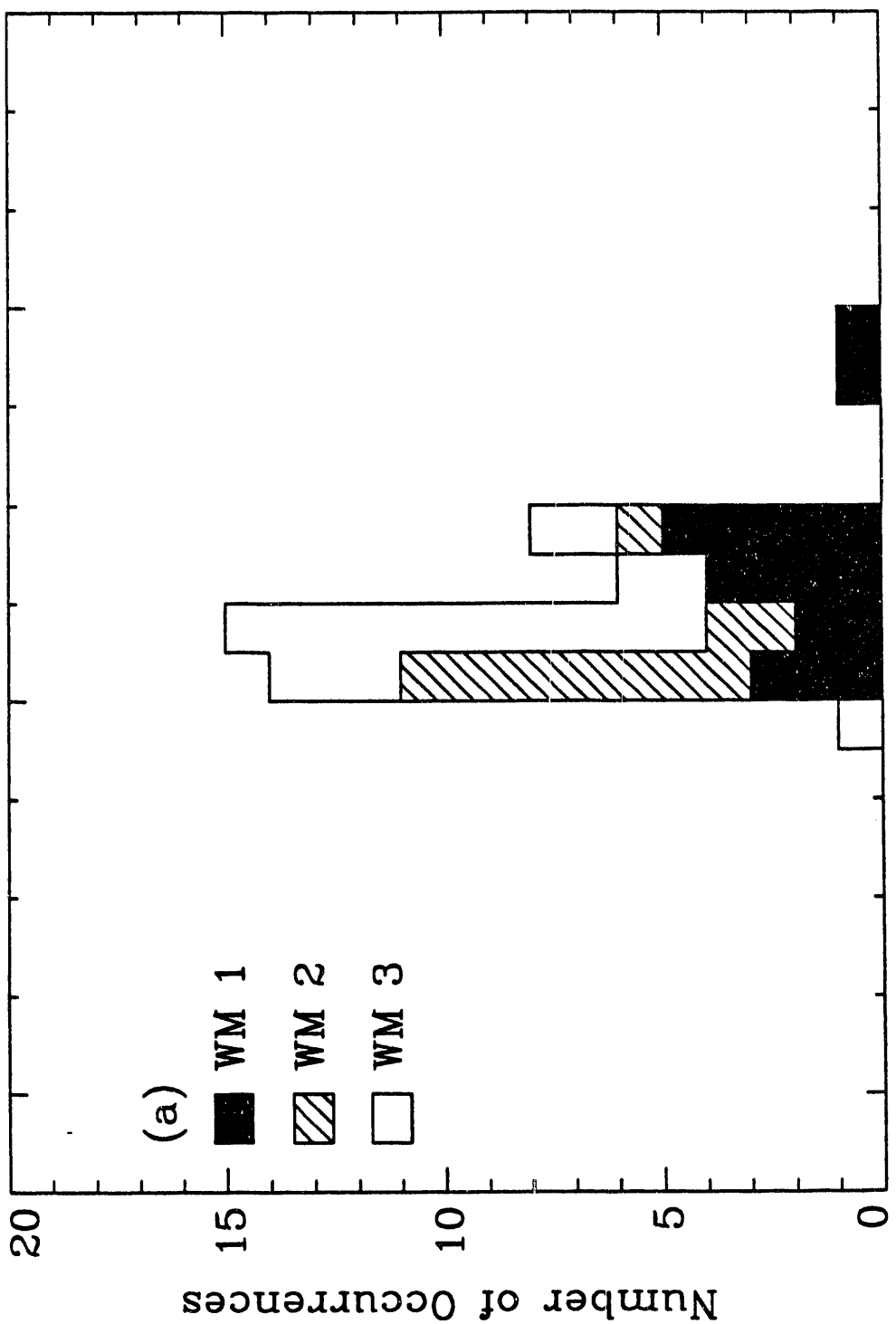

Figure 8.1(a) Histogram of CMB cycle measurements from White Mountain

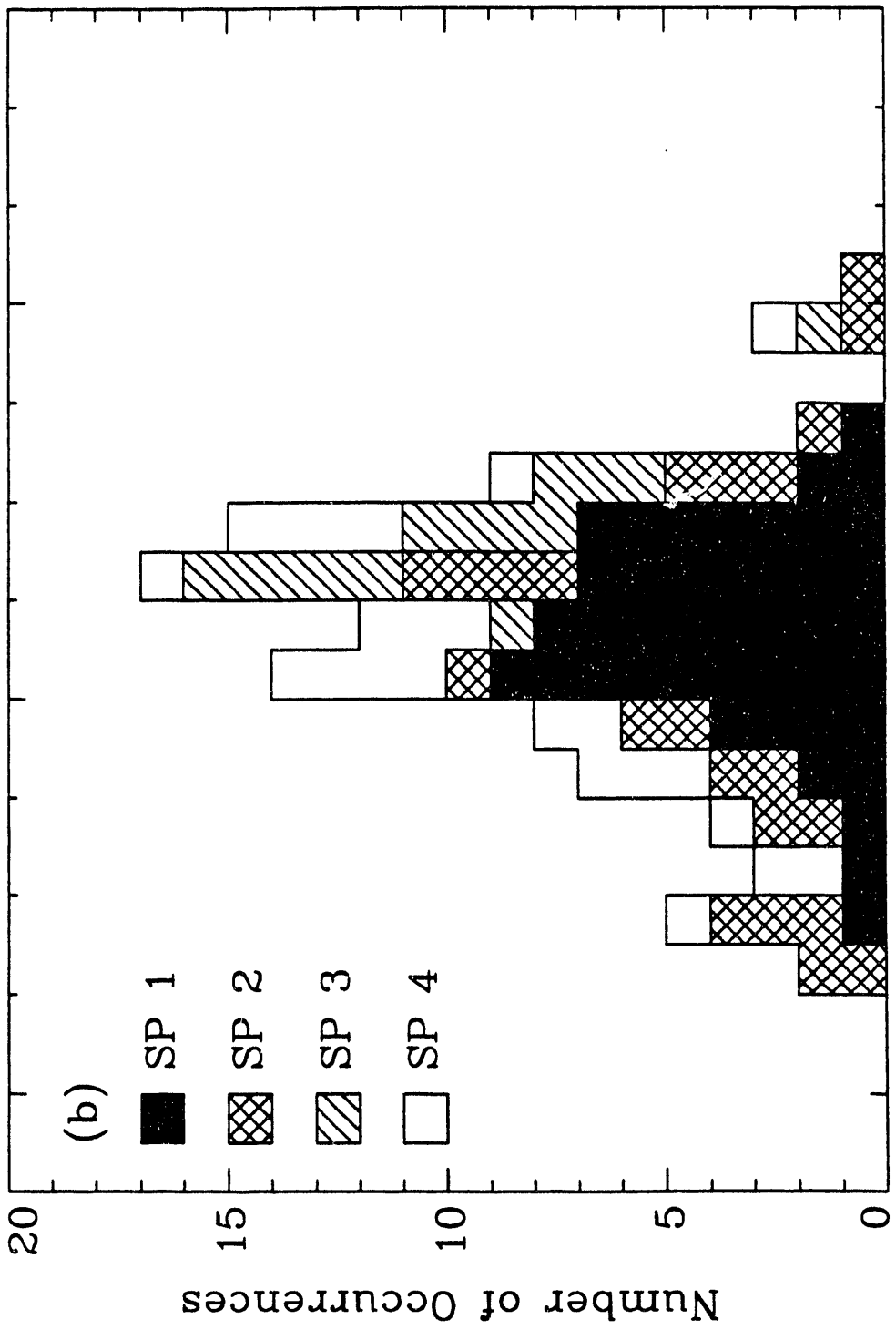

Figure 8.1(b) Histogram of CMB cycle measurements from the South Pole

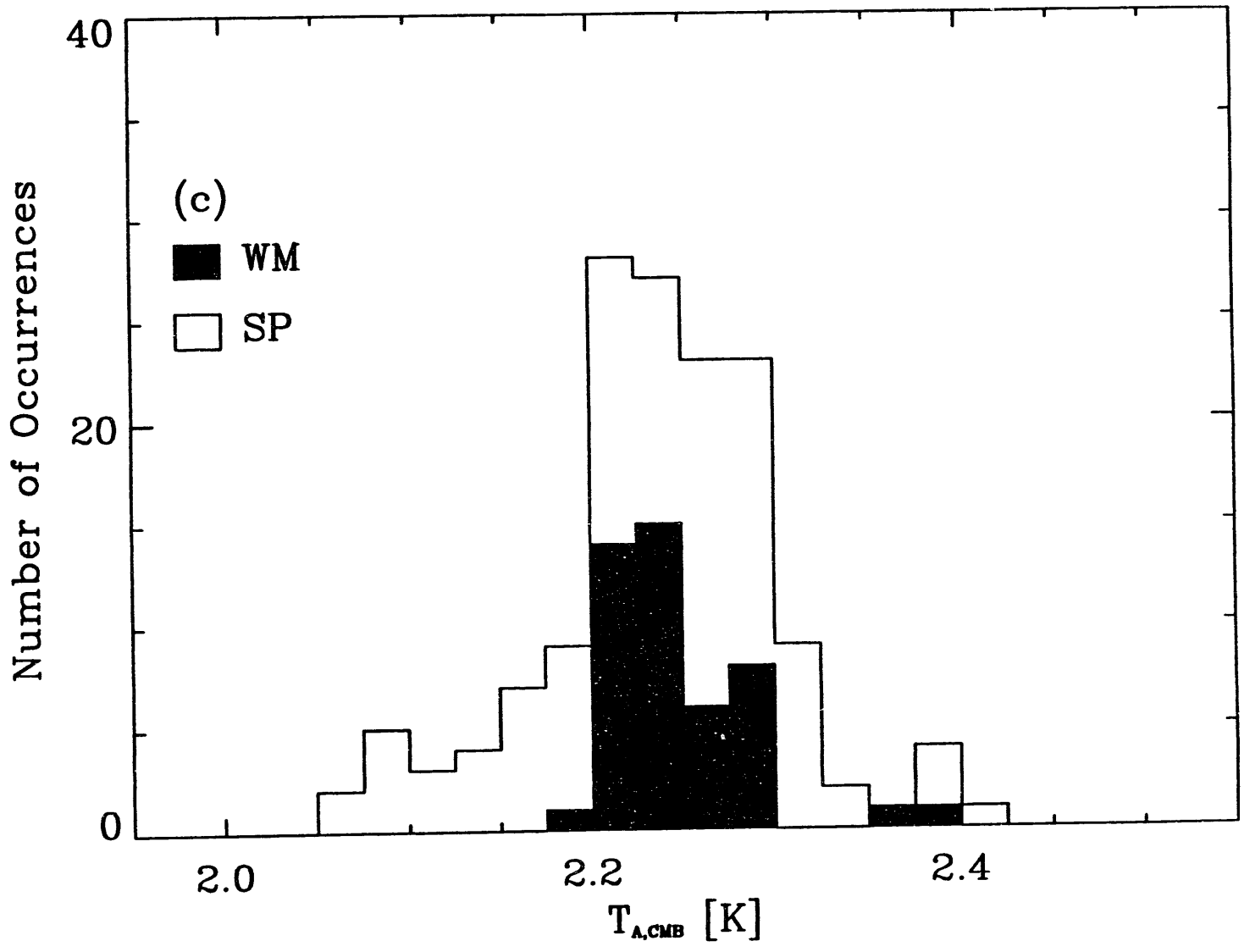

Figure 8.1(c) Histogram of all CMB cycle measurements

Chapter 9 Interpretation

The results are in good agreement with the value 2.11 ± 0.38 K obtained in 1986 from the White Mountain site with an earlier version of this instrument (Levin *et al.* 1988). Including the 1986 result and weighting by the uncorrelated parts of the error (≈ 0.34 K for the 1986 result) decreases the combined result by 0.010 K. This result is consistent with results of measurements at nearby frequencies: Howell and Shakeshaft (1966) measured T_{CMB} = 2.8 ± 0.6 K at 1.45 GHz and Pelyushenko and Stankevich (1969) measured T_{CMB} = 2.5 ± 0.5 K at 1, 1.5, and 2 GHz. Tables 9.1 (a) and (b) summarize previous measurements of the CMB.

The CMB result is 0.47 K, or ~2.5 σ, below the global average CMB temperature of 2.740 K. There is only a 1% chance of this occurring statistically. Other low-frequency ground-based measurements have reported CMB temperatures systematically lower than the FIRAS value; however none deviate by as much as the present result. This disagreement is due to an undetected problem with the measurement and/or a distortion in the CMB spectrum.

9.1 Possible Errors in the Measurement

If due to a problem with the cold load, the additional emission would be many times the 0.05 K total correction to the absorber temperature and we have not detected any such additional signal. Problems from instrumental effects, such as ΔT_{inst}, $\Delta T_{A,joint}$, and gain variations caused increased noise in the data; however the mean is very repeatable. Extra noise in the South Pole data, caused by a problem with a power supply, did not significantly change the mean in the zenith-CL difference.

The antenna joint injected noise into the CMB data. Increased noise in the 1989 data may also be evidence that the condition of the joint degraded from 1988 to 1989. The $\Delta T_{A,joint}$ correction was based on the best tests I could do in Berkeley. Tests of the effect with LHe in the cold load were not done and the error on $\Delta T_{A,joint}$ has been increased to allow for the modelling uncertainty.

The regions observed during three of the South Pole runs overlap. For the overlapping interval, $4.1^h < RA < 4.7^h$, $T_{A,sky}$ is 2.776 ± 0.016 K, 2.773 ± 0.029 K, and 2.781 ± 0.022 K for runs 1, 2 and 4, respectively. Because the corrections to these subsets of data are the same over this interval, the three measured values of $T_{A,sky}$ in this region should agree to within the error on the data. The rms of the averages is 0.004 K, much less than the 0.016 to 0.029 K standard deviation in the means. This, coupled with the good agreement between high- and low-gain data for each observation, shows that there is a source of scatter in successive sky-cold load temperature difference measurements, which does not appear within each individual measurement, and which has a repeatable mean. This noise is consistent with the properties of the joint at the antenna aperture as discussed in §5.6. The agreement between runs 1, 2, and 4 demonstrates that the sum of ΔT_{inst}, $\Delta T_{A,joint}$, $T_{A,sun}$, and $T_{A,RFI}$ (contributions which were not *a priori* known to be constant) did not change systematically from run to run at the ± 0.004 K level. Also, the excellent agreement between the White Mountain and South Pole results makes RFI and the sun unlikely as possible problems with the measurement.

Our estimate of ΔT_{inst} is based on measurements with the target temperature in the range 223 K to 331 K. We are unable to measure the dependence of ΔT_{inst} for target temperatures closer to 4 K; such measurements could have changed our estimate of ΔT_{inst}.

We rely on the theoretical understanding of microwave atmospheric emission to extrapolate the 7.5 and 3.8 GHz measurements to 1.47 GHz. If the roll-off in atmospheric emission occurs closer to 1.47 GHz, we may have overestimated the atmospheric contribution. According to the atmospheric model in §5.1, the roll-off frequency is ~10%

Table 9.1(a) CMB Results Before 1980 [a]

ν [GHz]	λ [cm]	T_{CMB} [K]	Sigma [K]	Technique[b]	Reference
0.408	73.5	3.7	±1.2	Ground (LN)	Howell & Shakeshaft 1967, *Nature*, **216**, 753.
0.610	49.1	3.7	±1.2	Ground (LN)	Howell & Shakeshaft 1967, *Nature*, **216**, 753.
1	30	2.5	±0.5	Ground (LN)	Pelyushenko & Stankevich 1969, *Sov. Astron.*, **13**, 223.
1.45	20.7	2.8	±0.6	Ground (Term)	Howell & Shakeshaft 1966, *Nature*, **210**, 1318.
1.5	20	2.5	±0.5	Ground (LN)	Pelyushenko & Stankevich 1969, *Sov. Astron.*, **13**, 223.
2	15	2.5	±0.5	Ground (LN)	Pelyushenko & Stankevich 1969, *Sov. Astron.*, **13**, 223.
2.3	13.1	2.66	±0.77	Ground (Term)	Otoshi & Stelzreid 1975, *IEEE Trans on Inst & Meas*, **24**, 174.
4.08	7.35	3.5	±1.0	Ground (Term)	Penzias & Wilson 1965, *Ap.J.*, **142**, 419.
9.4	3.2	3.0	±0.5	Ground (Term)	Roll & Wilkinson 1966, *Phys. Rev. Lett.*, **16**, 405.
9.4	3.2	2.69	+0.16/-0.21	Ground (CL)	Stokes et al. 1967, *Phys. Rev. Lett.*, **19**, 1199.
19.0	1.58	2.78	+0.12/-0.17	Ground (CL)	Stokes et al. 1967, *Phys. Rev. Lett.*, **19**, 1199.
20	1.5	2.0	±0.4	Ground (CL)	Welch et al. 1967, *Phys. Rev. Lett*, **18**, 1068.
32.5	0.924	3.16	±0.26	Ground (CL)	Ewing et al. 1967, *Phys. Rev. Lett*, **19**, 1251.
35.0	0.856	2.56	+0.17/-0.22	Ground (CL)	Wilkinson 1967, *Phys. Rev. Lett.*, **19**, 1195.
37	0.82	2.9	±0.7	Ground (LN)	Puzanov et al. 1968, *Sov. Astr.*, **11**, 905.
83.8	0.358	2.4	±0.7	Ground (LN)	Kislyakov et al. 1971, *Sov. Ast.*, **15**, 29.
90	0.33	2.46	+0.40/-0.44	Ground (CL)	Boynton et al. 1968, *Phys. Rev. Lett.*, **21**, 462.
90	0.33	2.61	±0.25	Ground (CL)	Millea et al. 1971, *Phys. Rev. Lett.*, **26**, 919.
90	0.33	2.48	±0.54	Plane (Term)	Boynton & Stokes 1974, *Nature*, **247**, 528.

[a] Data are included in the μ- and Y_{ff}-distortion least-squares fits but are not plotted in Figure 9.1

Table 9.1(b) CMB Results Since 1980 [a]

ν [GHz]	λ [cm]	T_{CMB} [K]	Sigma [K]	Technique[b]	Reference
0.60	50.	3.0	±1.2	Ground (Term)	Sironi *et al.* 1990, *Ap.J.*, 357, 301.
0.82	36.6	2.7	±1.6	Ground (Term)	Sironi *et al.* 1991, *Ap. J.*, 378, 550.
1.410	21.26	2.11	±0.38	Ground (CL)	Levin *et al.* 1988, *Ap.J.*, 334, 14.
1.47	20.4	2.27	±0.19	Ground (CL)	Bensadoun *et al.*, (this work)
2.5	12	2.79	±0.15	Ground (CL)	Sironi & Bonelli 1986, *Ap.J.*, 311, 418.
2.5	12	2.50	±0.34	Ground (CL)	Sironi et al. 1991, *Ap. J.*, 378, 550.
3.8	7.9	2.64	±0.07	Ground (CL)	De Amici et al. 1990, *Ap.J.*, 359, 219.
4.75	6.3	2.70	±0.07	Ground (CL)	Mandolesi et al. 1986, *Ap.J.*, 310, 561.
7.5	4.0	2.64	±0.06	Ground (CL)	Levin *et al.* 1992 *submitted to Ap.J.*
10	3.0	2.62	±0.06	Ground (CL)	Kogut et al. 1990, *Ap.J.*, 355, 102.
24.8	1.2	2.783	±0.025	Balloon	Johnson & Wilkinson 1987, *Ap.J. Lett.*, 313, L1.
33.0	0.909	2.81	±0.12	Ground (CL)	De Amici et al. 1985, *Ap.J.*, 298, 710.
90	0.33	2.60	±0.09	Ground (CL)	Bersanelli et al. 1989, *Ap.J.*, 339, 632.
90.3	0.332	<2.97		Balloon	Bernstein et al. 1990, *Ap.J.*, 362, 107.
113.6	0.264	2.70	±0.04	CN (z Per)	Meyer & Jura 1985, *Ap.J.*, 297, 119.
113.6	0.264	2.74	±0.05	CN (z Oph)	Crane et al. 1986, *Ap.J.*, 309, 822.
113.6	0.264	2.76	±0.07	CN (HD 21483)	Meyer et al. 1989, *Ap.J. Lett.*, 343, L1.
113.6	0.264	2.796	+0.014/-0.039	CN (z Oph)	Crane et al. 1989, *Ap.J.*, 346, 136.
113.6	0.264	2.75	±0.04	CN (z Per)	Kaiser & Wright 1990, *Ap.J. Lett.*, 356, L1.
113.6	0.264	2.834	±0.085	CN (HD 154368)	Palazzi et al. 1990, *Ap.J.*, 357, 14.
154.8	0.194	<3.02		Balloon	Bernstein et al. 1990, *Ap.J.*, 362, 107.
195.0	0.154	<2.91		Balloon	Bernstein et al. 1990, *Ap.J.*, 362, 107.
227.3	0.132	2.76	±0.20	CN (z Per)	Meyer & Jura 1985, *Ap.J.*, 297, 119.
227.3	0.132	2.75	+0.24/-0.29	CN (z Oph)	Crane et al. 1986, *Ap.J.*, 309, 822.
227.3	0.132	2.83	±0.09	CN (HD 21483)	Meyer et al. 1989, *Ap.J. Lett.*, 343, L1.
227.3	0.132	2.832	±0.072	CN (HD 154368)	Palazzi et al. 1990, *Ap.J.*, 357, 14.
266.4	0.113	<2.88		Balloon	Bernstein et al. 1990, *Ap.J.*, 362, 107.
30-600	1.0--0.05	2.735	±0.06	Satellite (FIRAS)	Mather et al. 1990, *Ap.J. Lett.*, 354, L37.
30-600	1.0--0.05	2.736	±0.017	Rocket (COBRA)	Gush et al. 1990, *Phys. Rev. Lett.*, 65, 537.

[a] Data are plotted in Figure 9.1

[b] Ground-based experiments calibrating with a LHe-cooled coaxial termination (Term) or a quasi-free space LHe-cooled load (CL) are indicated. For cyanogen (CN) measurements the observed star is reported in parentheses.

higher at the South Pole than at White Mountain and below ~0.5 GHz in both cases. As a worst case, if the roll-off occurred instead at 1.0 GHz, we would expect a ~4% systematic error from site to site, or ~0.04 K, which would pass undetected in our data. If the 7.5 and 3.8 GHz measurements both overestimate the atmospheric temperature by 0.1 K, $T_{A,atm}$ at 1.47 GHz would be ~0.09 K high and T_{CMB} ~0.09 K too low.

The galactic emission may have been overestimated although the small ~0.57 K emission at the South Pole makes overestimate of the galactic signal an unlikely source of deviation. The zero level of the 408 MHz map would have to be decreased by 12 K to raise the result by 2 σ = 0.36 K. The gain of the 408 MHz map would have to be 63% lower or the spectral index 0.77 higher to raise the result by 2 σ.

9.2 Possible Spectral Distortions

I will complete the discussion of spectral distortions from the first chapter, present best-fit parameters to the data set and then discuss the implications of the fits.

Radiative Compton scattering and bremsstrahlung are capable of thermalizing an arbitrarily large energy release to the photons at times earlier than z_{therm} given by (Burigana 1991a):

$$z_{therm} = 2.9 \times 10^6 \, \hat{\Omega}_b^{-0.36} \qquad \text{if } \mu_o \geq 2.5 \tag{9.1}$$

where

$$\hat{\Omega}_b = \left(\frac{H_0}{50}\right)^2 \Omega_b \tag{9.2}$$

and Ω_b is the baryon density in units of the critical density. This is an upper limit because other effects also tend to thermalize the spectrum. Smaller energy releases are thermalized at lower redshift. Events which occur earlier than z_{therm} leave no traces in the CMB spectrum. For an energy release at $z < z_{therm}$, photons can no longer be produced fast enough to thermalize the spectrum, but Compton scattering can still efficiently redistribute the photon energies to achieve kinetic equilibrium. The rate of transfer of energy is given by the collision rate times the energy transfer efficiency. The optical depth to Compton scattering is obtained by integration. This is expressed by the Comptonization parameter y_e given by:

$$y_e = \int_0^z \frac{dz}{z} \frac{t_{exp}}{t_C} \tag{9.3}$$

where the expansion time and Comptonization times are given as follows. For $10^9 > z > 1 - \Omega^{-1}$ (after $e^- - e^+$ annihilation but before the curvature of the universe becomes important), the expansion timescale is (Burigana 1991a):

$$t_{exp} = \left(\frac{3}{8\pi G\rho_{0r}}\right)^{1/2} (1+z))^{-3/2} [\kappa(1+z) + (1+z_{eq})]^{-1/2} \quad (9.4)$$

where $\rho_{0r} = aT_0^4/c^2$ is the energy in the unperturbed spectrum,

$$z_{eq} = 1.0 \times 10^4 \left(\frac{T_0}{2.7\ \mathrm{K}}\right)^{-4} \hat{\Omega}_b \quad (9.5)$$

is the redshift at which the radiation and matter densities are equal, and $\kappa = 1.68$.

The timescale for redistributing photons in energy to achieve kinetic equilibrium is:

$$t_C = t_{\gamma e} \frac{mc^2}{kT_e} \quad (9.6)$$

where $t_{\gamma e}$ is the photon-electron collision time

$$t_{\gamma e} = \frac{1}{n_e \sigma_T c}, \quad (9.7)$$

n_e is the electron density, and σ_T is the Thomson cross section. Burigana *et al.* numerically integrate Equation (9.3) to find z_1, the redshift of unity optical depth to Compton scattering:

$$z_1 \approx 4.3 \times 10^4 \left(\frac{T_0}{2.7\ \mathrm{K}}\right)^{-1} \left(\frac{\kappa}{1.68}\right)^{0.25} \phi^{-1/2} \left(\frac{y_1}{\hat{\Omega}_b}\right)^{1/2}, \quad (9.8)$$

where $\phi = T_e/T_r$ is the electron temperature to radiation temperature ratio.

In summary, for a transfer of energy to the CMB during the interval $z_1 < z < z_{therm}$ Compton scattering brings the spectrum to kinetic equilibrium by on average scattering photons to higher energies. The result is a Bose-Einstein spectrum.

Bremsstrahlung produces photons efficiently at low frequency thermalizing the spectrum up to a frequency given roughly by (Burigana 1991):

$$x_c \approx 1.08 \times 10^2 \left(\frac{T_0}{2.7\ \mathrm{K}}\right)^{-9/4} \hat{\Omega}_b^{\ 1/2} \phi(\mu_o)^{-9/4} (1+z)^{-3/4} \qquad (9.9)$$

For typical values, x_c is at $\nu \leq 0.6$ GHz. The overall effect of Compton scattering and bremsstrahlung is to create a Bose-Einstein distribution which returns to the equilibrium temperature below x_c. This is expressed as a Bose-Einstein distribution with a frequency dependent chemical potential given by:

$$\mu(x) = \mu_o \exp\left[-\frac{x_c}{x_e}\right] \qquad (9.10)$$

where x_c is the transition from frequency between the Bose-Einstein and Planck regions and the chemical potential is related to the magnitude of the energy release by:

$$\frac{\Delta\varepsilon}{\varepsilon} \approx 0.7\ \mu_o \quad (9.11)$$

The wavelength and magnitude of the maximum deviation from the unperturbed spectrum is (Burigana *et al.* 1991):

$$\lambda_m \approx 5.64\ \hat{\Omega}_b^{\ -2/3}\ \mathrm{cm} \qquad (9.12)$$

$$\left(\frac{\Delta T}{T}\right)_m \approx 5.82\ \mu_o\ \hat{\Omega}_b^{\ -2/3} \qquad (9.13)$$

For $\hat{\Omega}_b = 0.1$, $\lambda_m \sim 26$ cm and $\Delta T/T \sim 0.135$ ($\Delta T \sim 0.37$ K). The new result at 1.47 GHz is 0.47 K low and is evidence for a non-zero μ_0.

At more recent times $z < z_I$, the optical depth to Compton scattering is not sufficient to thermalize an injection of energy into the CMB and the resulting distortion depends heavily on how the energy is transferred to the CMB.

If the heat is transferred via hot electrons, a Compton y-distortion is produced. The only evidence of this type distortion at low frequencies is a fractional decrease equal to $2y$. The FIRAS is very sensitive to a Compton distortion due to the characteristic sharp rise in the spectrum above the peak.

Bremsstrahlung (free-free scattering) off of the hot plasma will produce an excess with a characteristic ν^{-2} spectrum at low frequencies. The amplitude of the effect depends on the square of electron density, n_e (De Zotti 1986):

$$Y_{ff} = Y_o\, g(x)\, x^{-3}(1 - e^{-x}), \tag{9.14}$$

where

$$Y_o = \frac{8\pi}{3} \frac{e^6 h^2 n_e (n_H + 4n_{He})}{m\,(6\pi m k T_e)^{1/2} (k T_e)^3}$$

$$\approx 2.61 \times 10^{-25} \left(\frac{T_e}{T_R}\right)^{-7/2} \left(\frac{T_o}{2.7}\right)^{-7/2} (1+z)^{5/2}\, \Omega_b^2 \text{ sec}^{-1}, \tag{9.15}$$

n_e is the electron density, T_e and T_R are the electron and radiation temperature, respectively, and $g(x)$ is the velocity averaged Gaunt factor.

The relative magnitude of the Compton and free-free distortions is not fixed because the former is linearly proportional to the density of the plasma while the latter is proportional to the density squared. Thus, even though FIRAS results strongly limit the Compton distortion, they only weakly limit the low frequency free-free distortion.

This result sets constraints on the shape of the spectrum of the CMB below 10 GHz. Tables 9.2 and 9.3 summarize the Y_{ff}- and μ-distortion fit parameters for the complete data set with and without the new result at 1.47 GHz. The best-fit chemical potential distortion for $\Omega_b = 0.05$ gives $\mu = (2.4 \pm 1.2) \times 10^{-3}$ (1 σ error) with χ^2/DOF = 35/46. The goodness of fit is only weakly dependent on Ω_b since Ω_b determines the location and value of the maximum deviation (Equations 9.12 and 9.13) which are not well determined by the data set. The best-fit free-free distortion gives $Y_{ff} = (-1.0 \pm 2.4) \times 10^{-5}$ (1 σ error) with χ^2/DOF = 43/46.

The significance of the best-fit values increases with the new datum because it lies significantly below the high-frequency mean. The 1.47 GHz datum adds ~2 to the χ^2 of the μ-distorted spectra fits and adds 6-7 for the Y_{ff}-distorted spectra and the Planck fits

indicating that it makes either distortion a worse fit to the data. This is because the low frequency results (ν < 10 GHz) disagree with results at ν > 30 GHz and the distorted spectra do not have enough curvature in the 10 < ν < 30 GHz region to dip down fast enough.

The results obtained more recently than 1980 are plotted in Figure 9.1 with the largest chemical potential and free-free distortions allowed at the 2 σ level as determined by the above least-squares fit.

If the new result at 1.47 GHz is confirmed and due to a μ-distorted spectrum, it implies an fractional energy release of 0.17%. The 2 σ upper limit from the result at 1.47 GHz on the amount of energy that may have been transferred to the CMB (from Equation 9.11) is:

$$\frac{\Delta\varepsilon}{\varepsilon} < 3.4 \times 10^{-3} \text{ (95\% CL)}. \qquad (9.14)$$

Table 9.2 Results of Y_{ff} - and μ-distortion fits including the new result at 1.47 GHz. Uncertainties are 68% CL estimates.

Ω_b	Fit	T_{CMB} [K][b]	Best fit Y_{ff} or μ	χ^2	D.O.F.
---	Planck	2.737 ± 0.008	---	43.2	47
0.05	μ	2.748 ± 0.013	(2.4 ± 1.2) x 10^{-3}	34.7	46
0.05	Y_{ff}	2.738 ± 0.014	(-1.0 ± 2.4) x 10^{-5}	42.6	46
0.01	μ	2.747 ± 0.013	(2.5 ± 1.2) x 10^{-3}	35.8	46
0.01	Y_{ff}	2.738 ± 0.014	(-1.0 ± 2.4) x 10^{-5}	42.6	46

[a] Fit is to all spectrum data in Tables 9.1 (a) and (b).

[b] The unperturbed value of T_{CMB}.

Table 9.3 Results of Y_{ff} - and μ-distortion fits without the new result at 1.47 GHz. Uncertainties are 68% CL estimates.

Ω_b	Fit	T_{CMB} [K][b]	Best fit Y_{ff} or μ	χ^2	D.O.F.
---	Planck	2.739 ± 0.010	---	37.0	46
0.05	μ	2.745 ± 0.016	(1.6 ± 1.6) x 10^{-3}	33.0	45
0.05	Y_{ff}	2.739 ± 0.014	(0.1 ± 2.3) x 10^{-5}	37.0	45
0.01	μ	2.745 ± 0.016	(1.7 ± 1.3) x 10^{-3}	33.7	45
0.01	Y_{ff}	2.739 ± 0.014	(0.1 ± 2.3) x 10^{-5}	37.0	45

[a] Fit is to all spectrum data in Tables 9.1 (a) and (b) except the 1.47 GHz result.

[b] The unperturbed value of T_{CMB}.

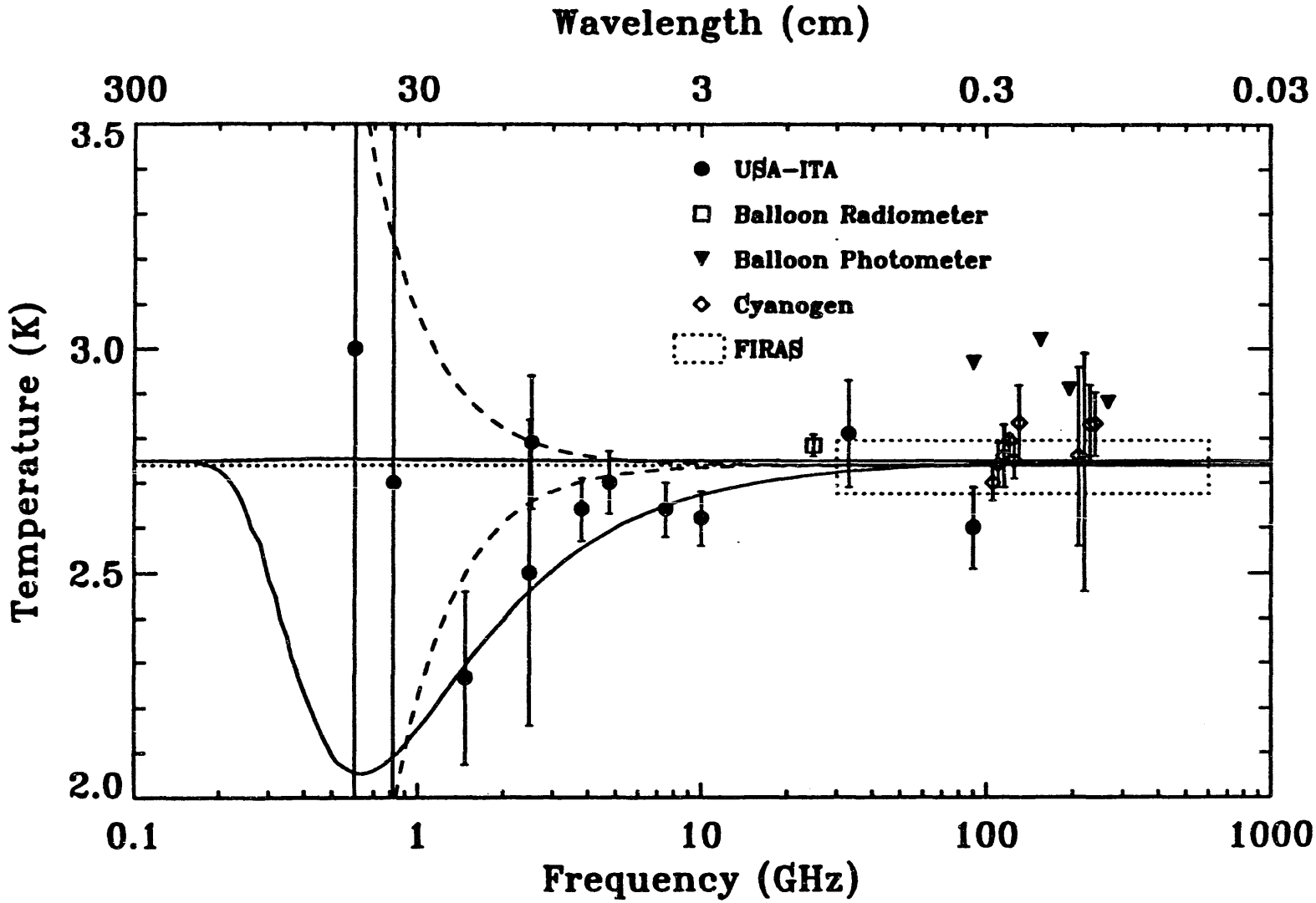

Figure 9.1 Recent CMB data and distortion limits. The data are from Table 9.1(b). The largest chemical potential (solid curves) and free-free (dashed curves) distortions allowed at the 95% confidence level are indicated.

Chapter 10 Future Observations

I plan to repeat this measurement from the South Pole site in December 1991. In addition to the 1.47 GHz measurement, members of the LBL Astrophysics Group will make a measurement at 2.0 GHz with a new radiometer, repeat the measurement at 7.5 GHz, and test a system to make measurements in the range 408 to 1000 GHz. The 1991 LBL group consists of Marco Bersanelli, Giovanni De Amici, John Gibson, Michele Limon, George Smoot, Bill Vinje, and myself; Steve Levin (JPL) will assist the LBL group. In collaboration with the LBL group, Giuseppe Bonelli and Andrea Passerini of the University of Milano will make a measurement at 2.5 GHz.

In preparation for the 1991 measurement at 1.47 GHz, many changes have been made to the experiment based on the experience of the 1988 and 1989 measurements and the results of the analysis. These changes are intended to reduce the major systematic errors in the 1988-89 result, to reduce the effects of instrumental problems, and to simplify the observations.

The major errors in the 1989 result are summarized in Table 10.1. The galaxy dominates the CMB error budget. The atmosphere, $\Delta T_{A,joint}$, and ΔT_{inst} dominate the error on $T_{A,sky} = T_{A,CMB} + T_{A,gal}$. The sky temperature is significant because 1) it can be used to calibrate galactic surveys, and 2) if, at some future time, galactic emission is determined to better accuracy, a corresponding improvement can be made in the CMB result. Here I summarize the changes made, the reasons for the modifications and the expected benefits.

Table 10.1 Sources of error in the 1989 South Pole Observations. Values are for run 3.

Source of Error	Error (K)	% contribution to total error
$T_{A,gal}$	0.163	61.2
$T_{A,atm}$	0.080	14.4
$\Delta T_{A,joint}$	0.070	11.0
ΔT_{inst}	0.063	8.9
$T_{A,gnd}$	0.034	2.6
$T_{A,load}$	0.023	1.2
$G(S_{zenith}-S_{load})$	0.016	0.6
$T_{A,RFI}$	0.005	0.1
$T_{A,sun}$	0.004	0.0

10.1 Improvements in the Galactic Correction

A more precise measurement of T_{CMB} at 1.47 GHz depends primarily on a more precise determination the galactic emission. The galactic signal was determined by scaling a 408 MHz map to 1.47 GHz using a spectral index consistent with experimental data. The HII component (~1% for observations away from the galactic plane) is obtained by scaling a compilation of sources at 2.5 GHz to 1.47 GHz. The error in the galactic signal at 1.47 GHz is due primarily to the uncertainties in the spectral index and the zero level error and gain error on the 408 MHz map.

The spectral index is determined by taking the ratio of the 408 and 1420 MHz maps (or corrected versions of those maps) or by taking the ratio of differences in the 408 and

1420 MHz maps (see §7.3). The spectral index error would be reduced by more precise differential or total intensity maps near 1.47 GHz.

Differential zenith scans, performed at the South Pole in 1989, are rendered useless by several instrumental problems. The problems, the sources of the problems, the solutions and the expected benefits on the measurement are:

1) There was excess noise in the radiometer output in 1989 due to the insufficient current capacity of the ±15V power supply (see §3.1). The power supply capacity has been increased. This change should result in a noise level close to the theoretical value of 0.011 K/Hz$^{1/2}$ (for $T_{sys} + T_{zenith} = 60$ K; see Equation 3.2). For zenith scans (and most other tests), $\tau \geq 8$ sec, so $T_{sens} \leq 0.004$ K for each observation and the statistical error on each difference measurement is 0.006 K.

2) There was leakage through the joint between the antenna and extension (see Figure 3.2). The joint has been rebuilt to reduce leakage. The new joint has planar (instead of beveled) mating surfaces. The new cold load and ground screen interface plates have rectangular openings and are 0.375" thick. The antenna aperture has a 0.375" step which allows the antenna aperture to extend through to the far side of these interface plates. This should result in a noise level nearer to the theoretically expected value.

The spectral index can be calculated from differential scans at two frequencies, ν_1 and ν_2. The error on α due to the map errors is given by (analogous to Equation 7.1)

$$\delta\alpha = \frac{1}{\ln(\nu_1/\nu_2)} \sqrt{\left(\frac{\delta\Delta T_1}{\Delta T_1}\right)^2 + \left(\frac{\delta\Delta T_2}{\Delta T_2}\right)^2} \qquad (10.1)$$

where $\delta\Delta T/\Delta T$ is the relative error on the differential profiles. The galactic signal error at 408 MHz in the regions observed ($T_{gal} \sim 20$ K at 408 MHz) is the quadrature sum of ±3 K (zero level error) and $0.1T_{gal}$ (gain error). Both the zero level and gain errors are highly correlated for nearby points on the sky. The error on the differential signal is $\sim 0.1\Delta T_{gal}$ (10% relative error) which contributes ~±0.08 to the error on α. To determine

α to $\leq\pm 0.15$, the relative error on the 1.47 GHz profile must be ≤ 0.16. The maximum differential signal (from the South Pole site and away from the galactic plane) at 1.47 GHz is ~0.25 K (Table 6.1), so the total error on the 1.47 GHz profile must be ≤ 0.04 K. The atmosphere and the instrumental offset will be the largest contributions to the error. The atmospheric error enters via the uncertainty in $\langle f(z) \rangle$ (§5.1) and pointing uncertainties (≤ 0.02 K). The instrumental offset error will depend on test results, but must be ≤ 0.035 K to keep the total error on the difference profile ≤ 0.04 K.

The second area for major improvement in the galactic correction is a higher-precision map at very low frequency (*eg.* at 408 MHz). In December 1991 the LBL group will test a new experiment designed to calibrate the zero level of the 408 MHz Haslam map, to make a map of the SCP cap out to ~-60° declination and to investigate the spectral index of the SCP region. This new radiometer consists of a 5.5 m dish (HPBW ~10°) with a helical-feed antenna at the prime focus. The receiver has seven 50 MHz-wide channels operating at 408, 500, 600, 700, 800, 900, and 1000 MHz.

The combined zero level and gain error on the 408 MHz map is ±3.9 K at the SCP (see §7.2). If the new measurement of the sky brightness at 408 MHz has an error smaller than 3.9 K, the uncertainly on the galactic correction at 1.47 GHz will be reduced. Ultimately, experiments like this very low-frequency sky-brightness spectrum experiment will be required to achieve a better understanding of the galaxy and improve the precision of CMB measurements below a few GHz.

10.2 Improved Measurement of $T_{A,sky}$

In the 1988-89 analysis, the atmospheric emission is determined from higher-frequency (3.8 and 7.5 GHz) measurements of atmospheric emission which are scaled to 1.47 GHz using a simple model of atmospheric emission for $\nu < 10$ GHz (§5.1). The error in the extrapolated value is due to the error in the measured data and errors in the

atmospheric model. The atmospheric scans made in 1989 were rendered useless due to leakage through the antenna-extension joint and the large error on the gravitational effect for the scans (similar to ΔT_{inst}).

In 1991, the atmosphere will be measured directly at 7.5, 2.0, and 1.47 GHz. The modification to the joint (§10.1) should render joint leakage insignificant. The instrumental offset for atmospheric measurements will be measured to higher precision; this is discussed below in the context of the vertical effect ΔT_{inst}. A third modification to the zenith scans is to shield the radiometer from ground radiation. This will be done by putting the receiver in a conical depression such that the aperture is below grade level and lining the depression with a reflective material (either aluminized mylar or aluminum sheet). All visible ground will be covered and the effective ground temperature will be ≤5 K warmer than the sky.

The same site setup will be used for the 2.0 and 7.5 GHz radiometers. The measurement at 2.0 GHz will be a cross-check on the atmospheric model used in the 1988-89 analysis and it is nearer to 1.47 GHz than the 3.8 GHz point used in the 1988-89 analysis.

If the modifications to the 1.47 GHz radiometer are successful, the direct measurement of atmospheric emission will provide a cross-check on the extrapolated value. However, the errors that enter into an atmospheric measurement (see, for example, Kogut *et al.* 1990) will be larger for the 1.47 GHz measurement than for measurements at higher frequencies (*eg.* the correction for galactic emission). Our understanding of the spectral dependence of atmospheric emission and the smaller error on higher-frequency measurements probably will make the error on the extrapolated value smaller than the error on the value measured with this radiometer.

The error in the CMB measurement due to the faulty joint at the antenna aperture, as discussed in §5.6, will be greatly reduced by the redesigned joint (§10.1). The differential contribution from the joint will be measured with the cold load absorber bathed in liquid helium and at the observation site. Measuring the effect in this way will eliminate the major

sources of error in ΔT_{joint} as measured in Berkeley with the cold load absorber bathed in liquid nitrogen . The mean and uncertainty on ΔT_{joint} for the 1991 measurements will likely be negligible.

The 1988-89 gravitational offset was measured for load temperatures in the range ~220-330 K. The correction to the CMB data was obtained by extrapolating to 4 K load temperature (§5.3). The large error on ΔT_{inst} was due to the scatter on the test data and the extrapolation in load temperature from ~250 K to 4 K, where the slope was based on data with a relatively small (~100 K) range in target temperature.

The offset will be measured using a new coolable load and a modified version of the 1988-89 ambient load. The coolable load consists of an absorber mounted on a rigid, cooled back-plate and thermally insulated by polyurethane and polystyrene foams, and the exclusive use of low thermal conductivity materials (stainless steel and fiberglass reenforced epoxy). Either liquid nitrogen or cold helium gas is circulated through an aluminum tube which is heat-sunk to the back-plate; the cooled back-plate then cools the absorber. An effective radiometric load temperature of ~150 K and ≤0.01 K orientation-dependent change in $T_{A,load}$ should be possible with this target. The front of the pyramidal absorber is insulated with polyurethane foam shaped to complement the front surface of the absorber. To minimize reflection, a transition region in front of the absorber tapers the large dielectric constant of the polyurethane to the low dielectric constant for polystyrene.

The 1988-89 ambient load (see Figure 3.3) has been insulated with polystyrene foam shaped to complement the front surface of the absorber to eliminate convection (which could mimic an instrumental effect).

The modified joint should improve the repeatability of the tests and eliminate any effect due to the old joint design. With the improved joint and increased range (~150-330 K) in load temperature, the uncertainty on the extrapolated value should be reduced. The actual improvement in ΔT_{inst} will be determined by the 1991 test results.

In 1988-89, the ground signal was calculated from the measured beam pattern and the observed horizon profile and ground properties. In 1991, the ground signal will be reduced by covering most visible ground with reflectors. During the CMB measurements, only a small solid angle (<0.8 sr) at >75° from beam center will be subtended by unshielded ground. The ground signal will be ≤0.05 K at 15° zenith angle, roughly half of the 1989 value.

Although the cold load contributes negligibly to the total error budget, several modifications have been made in an effort to check those aspects of the cold load analysis that depend on calculation and allow us to search for undetected systematic problems with the calibration (see §3.4 for a brief description of the cold load, §5.5 for a discussion of the radiometric temperature, and Appendix A for a compiete treatment of the cold load). The low result of the 1988 and 1989 results could be the result of undetected cold load emission. Radiometric wall emission may not be properly understood. Therefore, two heaters have been mounted on the upper section of the radiometric wall to allow a direct measurement of the emission of this section of the radiometric wall. The upper wall section is the source of most of the wall emission because it is the warmer than the lower wall section. The joint at the top of the wall was covered with Al tape to decrease any joint reflection or loss. The bottom of the absorber was sealed properly to prevent leakage of warm radiation into the radiometric space. The bucket dewar, which failed in 1989 at the South Pole, was repaired (under warranty) by the manufacturer, Kadel Engineering.

As in 1989, solar emission will be minimized by shielding and tilting the radiometer away from the sun. RFI will be monitored during the measurements.

The expected errors for the 1991 measurements are summarized in Table 10.2. The largest improvement is in the zenith temperature error which should decrease from ~0.10 K to ~0.04 K. The ~0.09 K error on $T_{A,sky}$ (decreased from ~0.13 K in 1989) will be completely dominated by the error on atmospheric emission. The three scenarios of the galactic emission error indicate the range of possible results for the 1991 measurements.

If no improvement in the galactic signal error is made, the CMB result error will be decreased from 0.21 to 0.19 K. If the low-frequency sky-brightness experiment calibrates the SCP to ±2 K and the differential profiles at 1.47 GHz are successful, the error on the CMB result will be decreased from 0.21 to 0.14 K.

At present, more precise measurements of the low-frequency CMB temperature depend on improved galactic measurements. Emission from our galaxy, which is diffuse, is distinguishable from the CMB only by its frequency and spatial dependence. Ultimately, there will be confusion between low-frequency CMB spectral distortions and any isotropic variation of the synchrotron spectral index.

Table 10.2 Expected errors for the 1991 South Pole Observations.

Quantity		Error (K)	
$G(S_{zenith}-S_{load})$		±0.010	
$T_{A,load}$		±0.023	
ΔT_{inst}		±0.032	
$\Delta T_{A,joint}$		±0.010	
$T_{A,zenith}$		±0.043	
$T_{A,atm}$		±0.080	
$T_{A,gnd}$		±0.017	
$T_{A,sun}$		±0.004	
$T_{A,RFI}$		±0.005	
$T_{A,sky}$		±0.089	
$T_{A,gal}$	±0.162[a]	±0.134[b]	±0.106[c]
$T_{A,CMB}$	±0.185[a]	±0.161[b]	±0.138[c]

[a] The same galactic emission error as in 1989.

[b] Including a ±2 K calibration of the 408 MHz map at the SCP and a measurement of the polarized signal (~10% of total intensity) with 50% error.

[c] The improvements in (b) and a ±0.1 error on the spectral index.

References

Allen, C.W., 1973, *Astrophysical Quantities, 3rd edition*, (The Athlone Press, London, GB).

Bartlett, J., Stebbins, A., 1991, *Ap. J.*, **371**, 8.

Bensadoun M., *et al..*, 1992, *Rev. Sci. Inst.*, submitted.

Brouw, W. N., Spoelstra, T. A. Th., 1976, *Aston. Astophys. Suppl.*, **26**, 129.

Burigana, C., Danese, L. and De Zotti, G., 1991a, *Astron. Astroph.*, **246**, 49.

Burigana, C., De Zotti, G. and Danese, L., 1991b, *Ap. J.*, **379**, 1.

Danese, L. and De Zotti, G., 1977, *Riv. Nuovo Cimento*, **7**, 277.

Danese, L. and Partridge, R.B., 1989, *Ap. J.*, **342**, 604.

De Amici, G., *et al.*, 1991, *Ap. J.*, **381**, 341.

De Amici, G., *et al.*, 1990, *Ap. J.*, **359**, 219.

De Zotti, G., 1986, *Prog. Part. & Nucl. Phys. (GB)*, **17**, 117.

Duriex, M. and Rusby, R.L., 1983, *Metrologia*, **19**, 67.

Gordon, R. G., 1967, *J. Chem. Phys.*, **46**, 448.

Haslam, C.G.T., Salter, C.J., Stoffel, H., and Wilson, W.E., 1982, *Astr. Astroph. Suppl. Ser.*, **47**, 1.

Hill, R.J., 1987, *IEEE Trans. Antennas Propagat.*, **AP-35**, 198.

Howell, T.F., and Shakeshaft, J.R., 1966, *Nature*, **210**, 1318.

Jackson, J.D., 1975, *Classical Electrodynamics, 2nd edition*, (John Wiley & Sons, NY)

Kogut, A., *et al.*, 1990, *Ap. J.*, **355**, 102.

Kogut, A., *et al.*, 1991, in: Holt, S., Bennet, C., and Trimble, V. (edts.); Proceedings 'After the First Three Minutes' workshop, College Park, MD, USA.

Kraus, J. D., 1966, Radio Astronomy, McGraw-Hill, New York.

Lawson, K. D., *et al.*, 1987, *Mon. Not. R. astr. Soc.*, **225**, 307.

Levin, S.M., *et al.*, 1988, *Ap. J.*, **334**, 14.

Levin, S.M., *et al.*, 1992, *Ap. J.*, submitted.

Liebe, H.J., 1985, *Radio Science*, **20**, 1069.

Mather, J., *et al.*, 1990, *Ap.J. Lett.*, **354**, L37.

Pauliny-Toth, I.I.K., and Shakeshaft, J.R., 1962, *Mon. Not. R. astr. Soc.*, **124**, 61.

Peebles, P.J.E., 1971, Physical Cosmology, (Princeton University Press, Princeton, New Jersey, USA).

Pelyushenko and Stankevich 1969, *Sov. Astron.*, **13**, 223.

Price, R.M., 1969, *Aust. J. Phys.*, **22**, 641.

Reich, P., and Reich, W., 1986, *Astr. Astroph. Suppl. Ser.*, **63**, 205.

Silk, J. and Stebbins, A., 1983, *Ap.J.*, **269**, 1.

Sironi, G., *et al.*, 1991, *Ap.J.* , **378**, 550.

Sironi, G., *et al.*, 1992, *Ap.J. Lett.*, in preparation.

Smoot, G., *et al.*, 1983, *Phys. Rev. Lett.*, **51**, 1099.

Ulaby, F.T., Moore, R.K., Fung, A.K., 1981, *Microwave Remote Sensing: Active and Passive, Vol. 1*, (Addison-Wesley Publishing Company, Reading, MA).

Verschuur, G.L., and Kellermann, K.I. (edts.), Galactic and Extragalactic Radio Astronomy, 1974, (Springer-Verlag, New York, USA).

Warren, S.G., 1984, *Appl. Opt.*, **23**, 1206.

Weinberg, S., 1972, *Gravitation and Cosmology*, (John Wiley & Sons, New York, USA)

Willis, A. G., et al., 1977, in: IAU Symp. No. 74, Radio Astronomy and Cosmology, pg. 39, Jauncey, D. L. ed., D. Reidel, Dordrecht, Holland.

Witebsky, C., *et al.*, 1987, *IEEE Trans. Antennas Propagat.*, **AP-35**, 1310.

Appendix A The Cold Load Calibrator

A liquid helium-cooled absolute reference cold load for long-wavelength radiometric calibration *

Marc Bensadoun, Chris Witebsky, George Smoot, Giovanni De Amici,
Al Kogut,[a] and Steve Levin[b]

Space Sciences Laboratory and Lawrence Berkeley Laboratory
University of California, Berkeley, California 94720

ABSTRACT

We describe a large (78-cm) diameter liquid-helium-cooled blackbody absolute-reference cold load for the calibration of microwave radiometers. The load provides an absolute calibration near the liquid helium (LHe) boiling point, with total uncertainty in the radiometric temperature of less than 30 mK over the 2.5 - 23 cm wavelength (12 - 1.3 GHz) operating range. Emission from those parts of the cold load not immersed in LHe is ≤25 mK and the reflection coefficient is $\leq 3.5 \times 10^{-4}$. Total corrections to the LHe boiling point temperature are ≤50 mK over the operating range. This cold load has been used at several wavelengths at the South Pole, Antarctica and at the White Mountain Research Station, California to calibrate spectral measurements of the cosmic microwave background radiation. In operation, the average LHe loss rate was ≤ 4.4 l/hr, allowing day-long periods of operation without a LHe fill. The boiloff rate is not strongly dependent on the radiative load at the aperture, yielding very stable operation and radiometric performance. Design considerations, radiometric and thermal performance and operational aspects are discussed. A comparison with other LHe-cooled reference loads including the predecessor of this cold load is given.

* Submitted for publication to The Review of Scientific Instruments

INTRODUCTION

We have developed a large, liquid-helium-cooled cold load (CL) (Fig. 1) to permit precise absolute calibration for measurements of the long-wavelength ($\lambda \geq 1$ cm) spectrum of the cosmic microwave background (CMB). This instrument is based on one used for the same purpose in 1982-86[1], with improvements derived from our previous experience.

This device has been used to make measurements of the CMB at wavelengths of 4.0, 7.9, 12 and 20 cm (7.5, 3.8, 2.5 and 1.5 GHz) in December 1989 from the South Pole and, at all but 12 cm, from the University of California's White Mountain Research Station in September 1988. The results of these measurements are reported by Kogut *et al.*,[2] De Amici *et al*,[3] Sironi *et al.*,[4] Bensadoun *et al.*,[5] Levin *et al.*,[6] and De Amici *et al.*[7] Similar measurements at 7.9 and 12 cm have also been performed from White Mountain in past years using our previous load, providing a cross-check of the accuracy of the calibration obtained with the load described here.

A. SCIENTIFIC CONTEXT

The CMB is a relic of the early, hot universe whose spectrum contains information on the evolution of the universe. Low-frequency measurements of the CMB have been made with microwave radiometers, devices whose output changes in proportion to the change in input power.[8] As described elsewhere,[1-9] the measurement consists of comparing the signal difference between the cold load and the sky.

The precision of the result depends upon the calibration: the most accurate measurement is achieved when the cold load characteristics are precisely known and closely matched to those of the sky, with impedance similar to that of free space for low reflection and a radiometric temperature close to that of the sky (4 to 10 K at $1 < \lambda < 30$ cm). The

cold sky temperature requires an absorber immersed in liquid helium (LHe). Precise knowledge of the antenna temperature of the load requires low reflectivity, low emissivity of those parts not immersed in LHe, and precise knowledge of the physical temperature of the absorber.

Measurements of the CMB and tests for systematic effects are made from remote, high-altitude sites over a period of several days. Thus, the cold load must be transportable and robust, have stable performance and a low LHe loss rate, even during observations.

I. PREVIOUS COLD LOADS

Many long-wavelength measurements of the CMB have used LHe-cooled waveguide or coaxial cold loads to calibrate. Emission from the antenna and warm parts of such cold loads requires corrections of ~2 K which have been a major source of error (at the ±0.3 K level).[10,11,12] In the late 1960's, several measurements were made at centimeter wavelengths using LHe-cooled, quasi-free-space waveguide cold loads.[13,14,15] Uncertainty in the cold-load reference was reduced in these experiments to the ±0.1 K level, still a major source of error.

A. The 1982 Cold Load

In 1982, the USA-Italy long-wavelength CMB collaboration built a large, quasi-free-space waveguide cold load[1,16] to eliminate the major sources of error present in previous cold loads over the band from 12-0.33 cm. The measurements produced by this collaboration[17] and continued in 1984-7 by the Berkeley group[4,18,19,20] using the 1982 load were the first for which absolute calibration error was insignificant over the range of 3 to 8 cm wavelength. The 1982 load performance at 12 cm (the design long-wavelength limit) limited the accuracy of the measurement at that wavelength.

The primary features of the 1982 cold load were: (1) an absorber (Emerson & Cuming VHP-8 Eccosorb) immersed in LHe with reflection less than 2×10^{-4}, (2) an

aluminum-coated (13 μm of aluminum) mylar radiometric wall with a diameter of 70 cm, (3) a low-emissivity, boiloff-cooled, manually operated shutter to reduce the heat leak between calibrations, (4) two 23 μm thick polyethylene windows at the aperture to keep out air and moisture, and (5) an aluminum antenna/load interface plate. Insofar as they exist in the new load, these elements are indicated in Fig. 1; relevant dimensions are given in Table 1.

In 1986, we made measurements at 21.3 cm, outside the nominal operating range of the cold load. We encountered radiometric problems with the absorber, which was too thin to give low reflection, and with the manually operated shutter near the top of the radiometric wall. During calibrations the shutter was opened to expose the absorber to the radiometer, but gaps between the shutter and the adjacent radiometric wall caused unacceptably high reflection and emission. Furthermore, the wall was aging and its emissivity may have degraded. The heat loads caused by the large antenna and the poor dewar vacuum made operations very difficult. Consequently, it was decided to build a new cold load with better thermal and operational characteristics, designed specifically for accurate long-wavelength measurements. The 1988 cold load, described in the present paper, is similar in many respects to the 1982 load and draws extensively on the design, fabrication, operational experience as well as the radiometric performance of the previous effort.

II. COLD LOAD DESIGN AND COMPONENT SELECTION

A. General Description

The cold load consists of a bucket dewar with a microwave absorber immersed in a LHe bath (shown in Fig. 1; relevant parameters are given in Table 1). A radiometric wall, an overmoded circular waveguide, extends from the LHe-temperature absorber to the

ambient-temperature aperture, guiding the blackbody emission from the absorber up to the aperture to calibrate a microwave receiver. Each radiometer achieves a repeatable match to a flat interface plate covering the aperture, whose central hole matches the dimensions of the antenna mouth.

The temperature of the absorber, the dominant source of emission in the load (~99%), is determined from the absolute pressure over the bath of boiling LHe. We compute the radiometric temperature of the load by adding the absorber's blackbody signal to the emission from the warm surfaces, windows, and joints in the load, and correcting for the effect of reflections from the load. Reflection of the signal broadcast by the radiometer and the signal from the absorber occurs at the interface plate, the windows, the helium liquid/gas interface, the absorber tips, and the absorber backing. These contributions to the cold load thermodynamic temperature are shown schematically for a typical radiometer in Fig. 2.

Thin polyethylene windows at the aperture prevent condensation of air and moisture inside the load. Infrared-blocking windows located just above the LHe bath intercept ~95% of the large ir heat load entering the aperture. Cold He boiloff gas is flowed past them to remove the absorbed heat from the load. To further reduce the radiative heat leak and protect the load during periods between calibrations, a low-emissivity, thermally-insulated cover is placed over the aperture.

The LHe level, pressures throughout the load, and the temperatures of the absorber, the ir-blocking windows and the radiometric wall are critical to the evaluation of the cold load radiometric temperature and to the smooth operation of the load. Sensors to measure these quantities are located in the 1.6 cm annular space outside of the radiometric wall. A liquid nitrogen level sensing system is also included for use during precooling and radiometric testing.

B. Physical Description

The aluminum/fiberglass vapor-cooled LHe bucket dewar, manufactured by Kadel Engineering, has a neck tube consisting of two 57 cm long, 1.6 cm thick epoxy-fiberglass sections, with a He diffusion barrier of stainless steel foil. The vacuum space has 225 g of activated charcoal getter material attached to the aluminum inner curvature head. The load weighs ~350 kg.

The polyethylene windows are sealed to the top and bottom of an annular aluminum holder. The window holder makes an O-ring seal with the top of the dewar interface. The dewar interface houses the electrical and pressure-sensor feedthroughs as well as the vacuum-insulated fill line, gas purge line, and vent lines.

The top of the radiometric wall attaches to the dewar interface. The upper and lower wall sections are joined by a three-ring aluminum annulus which also holds the ir-blocking windows. The foam absorber, backed by copper screen, is held in place by a friction fit with the wall and by contact with the bottom of the dewar. All seals are made gas-tight with O-rings, silicone (for permanent seals) or latex (for the polyethylene windows). The fill line extends to the bottom of the inner curvature head.

C. The Absorber

The absorber is characterized by its thermodynamic temperature (≈ 4 K) and its reflectivity at that temperature and at the wavelengths of interest. The temperature of the LHe bath is reliably determined to ± 2 mK by measurement of the pressure over the LHe bath, with a cross-check from electronic temperature sensors.

The absorber is constructed from VHP-12 Eccosorb[21] with a 5.7 cm backing layer of Eccosorb LS-22 and LS-24. This absorber is a carbon-impregnated, open-cell, urethane foam with good microwave absorption at 4 K, small volume, low specific heat, good porosity, and low cost.

Reflection from the absorber occurs at the front surface due to the imperfect dielectric matching of the pyramids to the LHe bath, and at the metal backing. The magnitude of the reflection is determined by the shape of the front of the absorber and the temperature- and frequency-dependent complex dielectric constant.

As the absorber cools from 300 K to 4 K, reflection from the front surface decreases slightly because the conductivity of the material decreases with temperature. The decrease in conductivity with temperature reduces the loss in the absorber, increasing the signal reflected from the metal backing. At cm wavelengths, the conductivity, and therefore the power-loss factor, β, is only weakly wavelength dependent. We can scale a previously measured upper limit on the power reflection r_0^2 at wavelength λ_0 to estimate r^2 at wavelength λ:

$$\frac{r^2}{r_0^2} = \exp\left(-\beta\left[\frac{l}{\lambda} - \frac{l}{\lambda_0}\right]\right), \tag{1}$$

where l is the effective absorber thickness. The upper limit on the reflectivity of the 1982 load (VHP-8 absorber at 4 K) at $\lambda_0 = 12$ cm was measured to be $r_0^2 \leq 2 \times 10^{-4}$.[22] The new absorber is thick enough to give approximately the same upper limit at $\lambda = 23$ cm. The reflection for the four radiometers used at the South Pole in Dec 1989 is given in Table 2.

D. Windows

A window of thickness $t << \lambda$ is described by its amplitude reflection, r, and emissivity, e:

$$r = \pi(\varepsilon - 1)t/\lambda \tag{2}$$

$$e = \alpha t = 6.30\, t/\lambda \tan\delta\, \varepsilon^{1/2}, \tag{3}$$

where ε is the dielectric constant, α is the absorption coefficient and $\tan\delta$ is the loss tangent of the material.[23] The reflected power (in units of antenna temperature) is the product of the power reflection coefficient, r^2, and the incident signal. The emitted power is e times

the window's physical temperature. The dependence of both reflection and emission on thickness make thin windows desirable. Window reflection and emission increase at short wavelengths, setting the short-wavelength operating limit of the cold load. Reflection properties of the windows are given in Table 2. The window material properties, emissivity, and emission are given in Tables 3 and 4.

The two 23 μm-thick polyethylene windows have low microwave reflection and emissivity, and enough strength to support a 4 Torr pressure differential and withstand mild physical abrasion at temperatures as low as 200 K. Warmed boiloff He gas circulates between the windows to maintain the top window at a temperature high enough to prevent condensation.

A 250 K blackbody filling the aperture of the load would radiate 106 W to the LHe bath. If this heat were allowed to reach the bath, it would result in an unacceptable LHe loss rate of 150 l/hr. We use two windows made from Fluorglas[24] 381-3 cloth just above the LHe bath to reduce the radiative heat leak. This FEP Teflon[25]-impregnated glass cloth exploits the high opacity of glass in the ir, the microwave transparency of both glass and Teflon, and the outstanding flexibility and durability of Teflon at cryogenic temperatures. The top window consists of one sheet, the bottom consists of two sheets. The material is 30% glass (dielectric constant $\varepsilon_G \approx 5.0$) by volume with a total density of 0.0146 g-cm^{-2} and a thickness of ~75 μm. We model the Fluorglas material as a composite with dielectric constant $\varepsilon_F = \varepsilon_T(1-\phi) + \varepsilon_G\phi \approx 3.0$, where ε_T is the dielectric constant of Teflon and ϕ is the fraction of glass by volume. The 381-3 fabric is inexpensive, easy to handle and available in wide rolls (92 cm). The heat absorbed by these windows is removed from the load by cold He boiloff gas circulating between the windows and then out of the load. No correction to the reflection or emission is made for the small solid angle subtended by the vent holes in these windows (see §II F).

E. Radiometric Wall

We used two identical 77.7 cm i.d., 1 mm thick epoxy-fiberglass cylinders with 1100-H19 aluminum 25 μm thick (10 skin depths at 1.5 GHz) on the inner surface, leaving a clearance of ~1.6 cm between the radiometric wall and dewar wall. The smooth, low emissivity wall subtends a small gain-weighted solid angle. Its thermal conductivity is low, and heat heat conducted down the wall is removed by boil-off gas.

Radiometric wall emission received by the radiometer depends on the temperature profile of the wall, the surface resistivity, the antenna beam pattern (or field configuration) and the effect of small gaps in the wall. The surface resistivity, R_S (ohms), is[26]

$$R_s = \sqrt{\frac{\pi c \mu}{\lambda \sigma}} \quad \text{ohm} \tag{4}$$

where $\mu = 4\pi \times 10^{-7}$ (H/m) and σ is the conductivity (ohm^{-1}/m). The emissivity of the surface is $R_S/c\mu$, proportional to $\lambda^{-1/2}$. At $\lambda = 20$ cm, the wall emissivity varies from 3×10^{-5} at 273 K to 1×10^{-5} in LHe, where the conductivity is determined from the Gruneisen relation.[27] Emission from a 2.5 μm-thick waxy dielectric coating is included, but contributes negligibly.

Below the ir-blocking windows, a small hole in the wall allows for measurement of the pressure over the LHe bath. Thirty-two holes, spaced evenly around the circumference 4 cm above the top ir-blocking window, allow the He boiloff gas to exit the radiometric space. Each hole is 6.4 mm in diameter and backed by copper mesh. Close to the top of the upper wall section are holes for pressure sensing and gas purging.

Small steps in the radiometric wall diameter at the joints between the fiberglass sections and the window holders cause a small impedance change. The step sizes average ≤0.5 mm (and never exceed 1 mm). A 0.5 mm thick epoxy-fiberglass layer at the aperture joint electrically isolates the load from the radiometer interface plate to eliminate

ground-loops or eddy currents. The leakage and reflection from the joints are expected to be minimal.

F. Boiloff Helium Flow and Heat Flow

The gas flow serves the dual purpose of removing the 50-100 W radiative heat load and cooling the electrical leads, plumbing, and the radiometric and dewar walls. The gas flow is channeled up through holes in the middle of the lower ir-blocking window and out along the outer edge of the upper window to remove the radiative heat load, then immediately through the vent holes in the radiometric wall and up the annular space between it and the dewar wall (see Fig. 1). The ir-blocking window venting cross-section (16 cm^2 for each window) is larger than the wall vent cross-section (10 cm^2) to prevent any significant flexing of the windows. The boiloff gas exits the annular space through 6 vents near the aperture; a small fraction is heated and circulated between the polyethylene windows, while the remainder is vented to the atmosphere ~3 m away.

G. Sensors and Heaters

A 4-wire superconducting sensor (AMI 60 cm) measures the LHe level and a capacitive sensor (Cryomagnetics Model 50) measures the liquid nitrogen level. In addition, ten 330 Ω Allen-Bradley carbon resistors indicate reliably whether the liquid level is above or below each of them, allowing calibration of the continuous sensors and providing a backup system. The resistor insulation is removed to improve the thermal contact with their surroundings. Operated at a 10 V bias to provide self-heating, their current typically changes from 5 mA in LHe to 9 mA in cold He gas, and from 24 mA in liquid nitrogen to 27 mA in cold nitrogen gas. The resistors respond to ~1 mm changes in the cryogen level when at the liquid surface. The discrete sensors are located in the curvature head, at intervals along the lower portion of the wall, and at, and just above, the absorber tips. The resistors and the LHe continuous sensor are protected from splashing cryogen to improve their stability and reliability.

Pressures inside the load are measured via small tubes leading out to differential pressure gauges. The differential pressures across the windows and wall (important because the cryogen level sensors are outside of the wall) are measured to $<\pm 0.2$ Torr. The differential pressure over the cryogen (compared to ambient) is also measured to $<\pm 0.2$ Torr.

The absorber temperature is measured directly by two Lakeshore CGR-1500 carbon-glass resistors (CGR) and one 1N4148 diode. The CGRs have high sensitivity at LHe temperatures and are repeatable, capable of a ±5 mK measurement, while the diode has better sensitivity at warmer temperatures. The radiometric wall temperature is measured to ±5 K by 6 matched 1N4148 diodes epoxied to the exterior of the wall (one below the ir-blocking windows, five above).

All of the sensors are located in the space between the dewar and radiometric walls.

A 150 W heater at the bottom of the dewar aids in the removal of water vapor before precooling and liquid nitrogen residue afterward, and in warming up the load. The dewar heater and the He gas heater are electrically isolated from the load.

IV. RADIOMETRIC MODELLING

We have modelled the radiometer-cold load system as a radiometer observing an ideal absorber, separated by a two-port device with power reflection r^2, and loss A. The load antenna temperature, $T_{A,CL}$, is to first order the antenna temperature of the absorber, $T_{A,abs}$. Corrections to $T_{A,abs}$ are due to the reflection and absorption losses as the absorber signal propagates to the receiver, the power emitted from the lossy parts, and the power emitted by the radiometer which is reflected back to the radiometer. By design, the reflection and attenuation are small ($<10^{-3}$) and the emission and reflection terms can be considered independently:

$$T_{A,CL} = T_{A,abs} + r^2 (T_B - T_{A,abs}) + A (T_{CL} - T_{A,abs}), \qquad (5)$$

where T_{CL} is the effective physical temperature of the lossy part, and T_B is the broadcast temperature of the radiometer.

The correction due to loss is the sum of the emissions from the windows and radiometric wall. To find the correction due to reflection we compute r^2 (where by r^2 we mean $|r|^2$ since, in general, r is complex) using the reflection properties of the antenna/load interface, the windows, the liquid helium bath, the absorber, and the radiometer. The computation of r^2 is done in Appendix A.

This method of modelling the reflection gives the coherent (phase-dependent) reflection and the incoherent (phase-independent) reflection. Coherent reflection terms arise because the coherence length of the broadcast radiation is comparable to the separation between the sources of reflection. Incident monochromatic radiation, with amplitude E_0, reflecting off of two sources, with amplitude reflection coefficients r_1 and r_2, gives rise to reflected radiation with amplitude $E_r = E_0 r_1 + E_0 r_2 e^{i\Delta\phi}$, where $\Delta\phi$ is the phase difference of the two signals when they are detected. The reflected power is given by:

$$|E_r|^2 = E_0^2 r_1^2 + E_0^2 r_2^2 + E_0^2 r_1 r_2 \cos(\Delta\phi). \qquad (6)$$

The first two terms are independent of the phase of the signals and depend on the power reflection coefficients which are small (*e.g.* for the absorber, $r^2 \leq 3.5 \times 10^{-4}$). The last term, the coherent reflection term, depends on the phase difference and the *amplitude* reflection coefficients.

If one of the reflections is the reflection internal to the antenna, r_R, then the term depends on the position of the antenna and the term can be more than a factor of ten larger than other reflections in the load (r_R , typically ~0.1, is the largest reflection coefficient in the antenna/load system). If the separation between the two reflections is comparable to the coherence length of the signal (typically ~150 cm), the coherent reflection term is diminished. For terms involving the significant reflections within the load (those from the ir-blocking windows, the helium interface, and the absorber) the separation is small

($\leq$ 40 cm) compared to the coherence length. Terms involving r_R also have a large separation (~150 cm) which reduces the importance of r_R; these terms are comparable in magnitude to the coherent terms involving only reflections inside the load.

V. MEASUREMENT OF RADIOMETRIC PROPERTIES

Our past measurements of the polyethylene window emission and reflection are in agreement with the theory (see §II.D) using the parameters listed in Table 3. The polyethylene window reflection and emission are given in Tables 2 and 4.

A. Cold Load Reflection

We measured the reflection of the antenna/cold load system at 20 cm wavelength. At λ = 20 cm, reflection from the absorber, r_A, and radiometer, r_R, are the dominant sources of reflection in the load, so that, neglecting coherent reflection, $r^2 \sim r_R^2 + r_A^2$ (see Table 2). Fig. 3 shows slotted-line measurements of the reflection with the antenna viewing the absorber at ambient and LHe temperatures. No change in the total reflection between ambient temperature and 4 K is observed at the level of the noise in the data (±2 dB). The average of the measured reflection over the bandwidth of the radiometer is 3.5×10^{-4} (with ±50% error), consistent with the absorber reflection upper limit specified by the manufacturer (see Fig. 4).

Direct measurements of the cold load or absorber reflectivity were not made at shorter wavelengths. We use the estimated upper limit on absorber reflection as a function of frequency from the manufacturer's specifications (see Fig. 4) to scale from the value measured at 20 cm wavelength, with an uncertainty of ±50% from the 20 cm datum. Values for the radiometers used at the South Pole are given in Table 2.

We have determined the reflection correction to the absorber temperature when the antenna views the load. However, signal is reflected even when the antenna observes the sky. What is important for the CMB measurement is the difference in the cold load and sky

reflection corrections. Because the cold load reflection coefficient is small (see Tables 2 and 6) and the antenna/load interface reflection is small (see Appendix B), we expect this difference also to be small.

B. Infrared-blocking Windows

We measured the emission from ambient temperature Fluorglas 381-3 material at 20, 7.9, 4.0, 3.0 and 0.33 cm by measuring the change in the signal when the material was placed on an aluminum sheet which reflected the radiometer beam to the sky (a stable cold reference). The measured absorption coefficient in the 20 - 0.33 cm range is in good agreement with published sub-mm spectrometer measurements of Pyrex over the 0.5 - 0.033 cm range[28] (see Fig. 5). The measured absorption is significantly lower at 5 K that at room temperature at wavelengths longer than 0.05 cm. We use the room-temperature spectrometer data extrapolated to cm wavelengths (with an uncertainty of ±50% to account for errors in the extrapolation) to model Fluorglas absorption (see Table 3).

We determined the reflection coefficient at 4.0, 3.0 and 0.33 cm wavelength by measuring the combined emission and reflection, then removing the emission and coherent reflection signals. We measured the combined reflection and emission by measuring the change in signal when the Fluorglas was placed over the mouth of an upward-pointing antenna. Additional measurements at $\lambda = 0.91$ cm with a slotted-line reflectometer yeilded a Fluorglas power reflectivity of $(4\pm1) \times 10^{-4}$. The measured values are shown in Fig. 4. The line in Fig. 4 is the average of the reflection from Eq. 2 and from the measurement at 0.91 cm. The other measured values lie within a factor of two of this line and we take the error to be +100%/-50%. Table 2 shows the ir-blocking window reflection for the radiometers used at the South Pole.

C. Reflection Dependent on Antenna Position

Table 2 gives the calculated power-reflection coefficient of the position-dependent coherent reflection signal for the four instruments which used this load to calibrate at the South Pole in 1989 (see Appendix A for derivation). The position-dependent signal is that part of the coherent reflection signal which varies with the antenna/load separation. To measure this effect, an extension to the radiometric wall is placed at the load aperture to allow the antenna to move vertically by $\lambda/2$ and map out at least one period of the expected sine curve. Tests at 20, 7.9 and 4.0 cm wavelengths show no sine curves within the limits of the signal noise. The measured upper limits on the amplitude are consistent with theoretical predictions (see Table 5).

VI. COLD LOAD RADIOMETRIC TEMPERATURE

We evaluate the radiometric temperature of the cold load for the four radiometers used at the South Pole in 1989 (see Table 6). A similar procedure would be used to calculate the radiometric temperature for other instruments. The ambient barometric pressure during the CMB measurements at the South Pole ranged from 516 to 523 Torr. The barometric pressure over the LHe bath is increased by 1.0±0.1 Torr due to the LHe boiloff and by <0.1 Torr due to the weight of the column of cold He gas. The uncertainty in the barometric pressure over the LHe bath during any given measurement was ±1 Torr, dominated by the uncertainty in the measurement of the ambient pressure. The 517 to 524 Torr pressure over the LHe bath corresponded to a thermodynamic temperature of 3.835 to 3.847 K[29] with an uncertainty during any given measurement of ±0.002 K.

The correction to the absorber temperature due to reflection is obtained from the calculation of r^2 in Appendix A. The reflection correction, T_{refl}, can be expressed in the form of Eq. 6. In terms of the radiometer reflection coefficient, r_R, and the effective load reflection coefficient, r_{CL}:

$$T_{refl} = (T_B - T_{A,abs}) [\, |r_{CL}|^2 + r_{CL} r_R \cos(\Delta\phi) \,], \quad (7)$$

where $\Delta\phi$ is the phase difference between the load reflection and radiometer reflection. We refer to the first term of Eq. 7 as the incoherent reflection and the second term as the coherent reflection.

The incoherent reflection is the sum of the power reflections and coherent reflections from within the load; the error is equal to the quadrature sum of the individual errors (see Table 2). The coherent reflection is the sum of reflections dependent on radiometer position. The mean value of the coherent reflection is zero because the phase is unknown. We estimate the error as the linear sum of the rms of each of the coherent reflection terms (see Tables 2 and 5). This is a more conservative estimate than the quadrature sum.

The temperatures of the upper and lower ir-blocking windows are 50±10 K and 25±10 K, respectively (see §VII B). Their emission (see Table 4) is obtained using the emissivity from §V B.

The wall temperature increases from 50 K just above the ir-blocking windows to 120 K where the He boiloff gas enters the vent tubes (25 cm from the mouth) to 250 K (ambient temperature during the measurements) at the load aperture. The wall contribution is estimated at λ = 7.9 and 4.0 cm from the convolution of the antenna beam with the wall emission (§II.E), using the measured temperature distribution of the wall. At λ = 20 cm, where the free-space approximation is poor, we calculate the loss[30] for each of the 16 waveguide modes which can propagate. The amplitude of each mode is given by the mode-conversion calculation described in Appendix B. We estimate the contribution due to the joints in the wall in the ray approximation and use the amplitude of the emission as the uncertainty to account for modelling uncertainties. The wall emission at 12 cm is interpolated from the 20 cm and 7.9 cm values.

Radiation from the annular space between the radiometric wall and the dewar wall may leak into the radiometric space through the absorber due to improper rf sealing around the absorber. The blackbody temperature of the annular space is 15±10 K warmer than the LHe bath and thus can increase the radiometric temperature of the absorber. Roughly 50±25% of the signal enters into the absorber, and ~1.0±0.5% of the signal passes through the absorber at λ = 20 cm. The effective gain-weighted radiating surface is ~9% of the total absorber area. The total contribution at λ = 20 cm is 7±8 mK. The absorber attenuation scales exponentially with $1/\lambda$, and the effect is <1 mK for λ < 15 cm.

VII. THERMAL PERFORMANCE

A. Liquid Helium Loss Rate

In the absence of the ir-blocking windows, the principal heat leak to the liquid helium bath would be radiative. During a calibration, the heat leak would be of order 30 W; between calibrations, when the load is uncovered, the heat leak would be of order 100 W. We calculate the radiative heat leak with the ir-blocking windows, Q_R, from measurements of the transmission of the Fluorglas window material at 300 K and 4.2 K over the 100 - 1000 cm^{-1} range using a Fourier spectrometer. The measurements indicate that three layers at 300 K (4.2 K) transmit only 2% (5%) of the power. Assuming a 250 K greybody with emissivity e~0.3 at the load aperture with the ir-blocking windows at 20 to 50 K (similar to the λ = 20 cm antenna observing the load), we predict a radiative heat leak to the LHe bath of $0.6 < Q_R < 1.6$ W.

We can also estimate Q_R from the difference in the total heat leak to the helium bath during calibration with the 20 cm wavelength radiometer (3.1 W) and the total heat leak with the low-emissivity cover in place (2.2 W). The cover (e~0.05) emits ≤0.25 W at 250 K, much less than the radiometer antenna. The heat leak difference is approximately equal to the radiative component: Q_R ~0.9 W, consistent with our predictions.

The remaining heat leak to the LHe bath of 2.2 W comes primarily from conduction down the dewar and radiometric walls. In the absence of any vapor cooling, the conductive heat leak would be ~9 W. The heat leak through the dewar vacuum space is <0.1 W. The convective and conductive heat leak down the He gas column is <0.1 W with the ir-blocking windows in place.

B. Infrared-Blocking Window Temperature

The boiloff gas exits the load at a temperature of ~120 K when the aperture is covered by the 20 cm wavelength radiometer antenna (the maximum radiative heat leak). From the LHe loss rate and the enthalpy of the exiting boiloff gas, we calculate that the gas removes ~88 W of thermal power from the load. While the radiative heat load to the LHe bath is only ~3 W, the ~35 K temperature drop across the ir-blocking windows (see §VI) indicates that ~30 W of radiant and convective power is absorbed. The remaining ~58 W removed is primarily from vapor cooling of the dewar and radiometric walls.

The heat load to the upper (lower) ir-blocking window is <6 (<1.5) $mW\text{-}cm^{-2}$. Because the heat loading to both windows is small and the boiloff gas is in good contact with the windows, the windows and boiloff gas are in thermal equilibrium. The radiometric wall, measured to be 50 K just above the ir-blocking windows and 15 K just below, is also in good thermal equilibrium with the boiloff gas. We infer that the upper and lower ir-blocking windows are at 50±10 K and 25±10 K, respectively. The uncertainties take into consideration the efficiency of the convective vapor cooling and possible radiative heating.

VIII. OPERATIONAL PERFORMANCE

We prepared the cold load for operation by flushing it with nitrogen gas at a slow rate, changing the volume of gas ~14 times and heating the interior to ~30 C. We then filled the load with liquid nitrogen to precool it. After several hours, the liquid was pumped out through the fill line at a rate of ~1 l/min and residual liquid in the bottom of the curved

dewar was boiled off with the heater. The load was then purged of the nitrogen gas by flowing ~7 times the load volume of He gas into the top of the load while pulling out the colder, heavier nitrogen gas via the fill line. As an added precaution, He gas was flowed in the fill line and through the entire system, including the pressure sensing lines.

After a ~15 min initial cool-down period, LHe could be transferred at a rate of 3.6 l/min (~0.7 cm/min). The load was filled to 15-20 cm above the absorber tips, sufficient for a full day of observations. During observations, the level dropped by ≤ 0.85 cm/hr and the pressure above the LHe bath was <1 Torr above ambient. The top window was periodically checked for frost or debris and cleaned if necessary.

IX. COMPARISON WITH OTHER COLD LOADS

Coaxial cold loads used in the past have typically had ~300 mK error, even in the same wavelength range as this quasi-free space cold load. Previous quasi-free-space cold loads (excepting the 1982 load) have had larger corrections to the LHe bath temperature and larger uncertainties in the resulting $T_{A,CL}$ than this load. Table 7 compares four cold loads used for CMB measurements over the range from ~1-50 cm wavelength. The measurement at 50 cm is that of Sironi *et al.*[31]

The 12 and 7.9 cm wavelength radiometers have made measurements using both the 1982 and 1988 cold loads[3,4,7,32,33] and these measurements serve as cross-checks between the two loads. The uncertainties are large compared to the uncertainty quoted in this work because of uncertainties in the atmospheric correction (~±50 mK), so a comparison at the level of the quoted uncertainties on $T_{A,CL}$ is not possible with the existing data.

Table 8 summarizes the predicted load temperature, $T_{A,CL}$, and the measured temperatures of the atmosphere, $T_{A,Atm}$, and CMB, $T_{A,CMB}$ at 7.9 cm wavelength from 1986-9. The weighted averages of $T_{A,CMB}$ agree: for 1988-9 the result is 97±102 mK

higher than for 1986-87. The largest contribution to the error in this CMB measurement is the correction for atmospheric emission. For the three measurements made at White Mountain (1986-88), $T_{A,CMB} + T_{A,atm}$ is 191 ± 58 mK hotter as measured with the 1988 cold load, whereas $T_{A,atm}$ is measured to be only 64 ± 84 mK hotter in 1988.

Any increase from 1986-7 to 1988-9 due to the load used implies a decrease in the true cold load antenna temperature (when compared to the calculated $T_{A,CL}$) from the 1982 load to the 1988 load. If due to the 1988 load, this would require a significant negative coherent reflection correction to the LHe bath temperature (predicted to be less than 18 mK in magnitude). The 1982 load could be warmer than predicted if the radiometric properties changed due to repeated use and/or the wall emission was underestimated. Another potential source of emission which was unaccounted for in the 1982 load is from the antenna/load interface which did not dc-isolate the antenna and load. The difference in the measured CMB temperature could also be due to errors in the measurement of contributions to the sky signal. For example, the CMB difference could be explained if the atmospheric signal were 97 mK warmer than measured in 1988-9 (or cooler than measured in 1986-87).

We conclude that the differences in data obtained using the 1982 and 1988 loads are not significantly different, but that they do suggest one of the following: 1) the 1982 load is warmer than reported (or the 1988 load is cooler than reported), 2) the 7.9 cm wavelength radiometer had an offset (or other correction to the data) which was dependent on both the cold load and the radiometer position, or 3) the atmosphere was warmer than measured in 1988.

X. POSSIBLE IMPROVEMENTS

The back of the absorber should be completely closed, allowing no path for radiation to enter from outside the radiometric wall. The joints in the wall should be covered or eliminated. The glass-Teflon ir-blocking material would perform better both in the ir and microwave if the glass were quartz and if, instead of a woven fabric, the glass were a thin film. Any future CMB spectrum measurement should include direct measurements of the reflection from the radiometer antenna, the radiometer/load interface plate and the load, similar to those made with the 20 cm-wavelength radiometer.

This cold load could be used at ~30 cm wavelength if a thicker absorber were used. To be useful at wavelengths much greater than 30 cm, careful radiometric analysis and testing of the load would be required (in addition to the use of a correspondingly thicker absorber). If the wall diameter and absorber thickness are simply scaled with wavelength, the volume of LHe required to begin operation ($\propto\lambda^3$) and the loss rate ($\propto\lambda^2$) increase rapidly, making the quasi-free space design impractical for very long wavelength calibration. To be useful at shorter wavelengths (λ <2.5 cm), a better ir-blocking material should be used or a higher heat leak to the LHe bath must be tolerated. The corrections due to window and wall emission would be reduced if the calibration were done at balloon altitude, where these emissive parts of the calibrator could be operated at lower temperatures.[34]

ACKNOWLEDGEMENTS

We thank John Gibson for the electronics in the cold load, the Mechanical Shops at the Lawrence Berkeley Laboratory, in particular Armando Meuti and Kit Mui for their help in manufacturing parts of the load, Keith Alexander at Kadel Engineering, David Miller and Bob McMurray of UC Berkeley for their help in measuring the ir properties of Fluorglas, and Scott Friedman for work on the 1982 load. We also gratefully acknowledge the assistance of Barron Chugg, Jenny Hwang, Jay Levin, Michele Limon, and Faye Mitschang. This work was supported by the NSF Division of Polar Programs under Contract No. DPP-8716548, the Physics Division of the Lawrence Berkeley Laboratory, and the Division of High Energy Physics of the U.S. Department of Energy under Contract No. DE-AC03-76SF00098.

APPENDIX A: Cold Load Reflection

The radiometer broadcast power, with electric field amplitude E_0, is reflected by the absorber, the LHe surface, the windows, the cold load interface and in the radiometer itself, resulting in reflected power with electric field amplitude E_r. The i-th component of the reflected signal has an amplitude $E_0 r_i$ and phase ϕ_i which is related to the phase of the reflection internal to the radiometer (taken as the reference phase). Neglecting multiple reflections, the amplitude reflection coefficient, r, is the sum:

$$r = E_r/E_0 = r_R + r_I e^{i\phi I} + r_{P1} e^{i\phi P1} + r_{P2} e^{i\phi P2} + r_{F1} e^{i\phi F1} + r_{F2} e^{i\phi F2} + r_H e^{i\phi H} + r_A e^{i\phi A}, \quad \text{(A1)}$$

where the subscripts R, I, P, F, H and A refer to the radiometer, the antenna/load interface, the polyethylene, the ir-blocking windows (made of Fluorglas), the LHe surface and the absorber. The polyethylene windows have equal thickness ($r_{P1} = r_{P2}$); the lower ir-blocking window has twice the thickness of the upper ($r_{F2} = 4r_{F1}$). The antenna/load interface term is generally predicted to be very small ($r \approx 3 \times 10^{-3}$ for the 20 cm wavelength radiometer; see Appendix B) and the term for radiometer/load interface reflection is dropped. The LHe surface reflection is given by $r_H = (\varepsilon_{LHe}-\varepsilon_{He})/(\varepsilon_{LHe}+\varepsilon_{He}) = 1.0 \times 10^{-2}$.

To find the correction due to reflection we compute $|r|^2$:

$$\begin{aligned} |r|^2 = {} & r_R^2 + 2r_P^2 + r_{F1}^2 + r_{F2}^2 + r_I^2 + r_A^2 \\ & + 2r_R r_P \cos(\phi_{P1}) + 2r_R r_P \cos(\phi_{P2}) + 2r_R r_{F1} \cos(\phi_{F1}) + 2r_R r_{F2} \cos(\phi_{F2}) \\ & + 2r_R r_H \cos(\phi_H) + 2r_R r_A \cos(\phi_A) + 2r_P^2 \cos(\phi_{P1} - \phi_{P2}) \\ & + 2r_{F1} r_{F2} \cos(\phi_{F1} - \phi_{F2}) + 2r_{F1} r_H \cos(\phi_{F1} - \phi_H) + 2r_{F1} r_A \cos(\phi_{F1} - \phi_A) \\ & + 2r_{F2} r_H \cos(\phi_{F2} - \phi_H) + 2r_{F2} r_A \cos(\phi_{F2} - \phi_A) + 2r_H r_A \cos(\phi_H - \phi_A). \end{aligned} \quad \text{(A2)}$$

The r_R^2 term is a correction to the radiometer gain and broadcast temperature and does not affect the cold load temperature or the measurement.

The reflection dilution factor D, calculated in the ray approximation, is the fraction of power broadcast which reenters the antenna aperture. This factor applies to all terms and for the longest wavelength radiometers, D ~ 1.

The phase-dependent terms represent signals reflected from two points arriving at the first amplifier with correlated phases. The path length between two sources a and b, $2x_{a,b}$, and the radiometer bandwidth, $\Delta\nu$, determine the degree of coherence, C:

$$C(z_{a,b}) = \left(\frac{\sin(z)}{z}\right)^2 \quad \text{for } z < \frac{\pi}{2}$$

$$\approx \left(\frac{1}{z}\right)^2 \quad \text{for } z > \frac{\pi}{2}, \tag{A3}$$

where $z_{a,b} = 2\pi x_{a,b}/L$, $L = c/\Delta\nu$ is the coherence length of the signal, and c is the speed of light, and we assume a square bandpass.

The cold load reflection coefficient is:

$$\begin{aligned}
|r|^2 = {} & 2r_P^2 + r_{F1}^2 D_{F1} + r_{F2}^2 D_{F2} + r_H^2 D_H + r_A^2 D_A \\
& + 2r_R r_{P1} \cos(\phi_{P1})\, C(z_{R,P1}) + 2r_R r_{P2} \cos(\phi_{P2})\, C(z_{R,P2}) \\
& + 2r_R r_{F1} \cos(\phi_{F1})\, D_{F1}\, C(z_{R,F1}) + 2r_R r_{F2} \cos(\phi_{F2})\, D_{F2}\, C(z_{R,F2}) \\
& + 2r_R r_H \cos(\phi_H)\, D_H\, C(z_{R,H}) + 2r_R r_A \cos(\phi_A)\, D_A\, C(z_{R,A}) \\
& + 2r_{F1} r_{F2} \cos(\phi_{F1} - \phi_{F2})\, D_{F1}\, C(z_{F1,F2}) \\
& + 2r_{F1} r_H \cos(\phi_{F1} - \phi_H)\, D_{F1}\, C(z_{F1,H}) \\
& + 2r_{F1} r_A \cos(\phi_{F1} - \phi_A)\, D_{F1}\, C(z_{F1,A}) \\
& + 2r_{F2} r_H \cos(\phi_{F2} - \phi_H)\, D_{F2}\, C(z_{F2,H})
\end{aligned}$$

$$+ 2r_{F2}r_A \cos(\phi_{F2} - \phi_A)\, D_{F2}\, C(z_{F2,A})$$

$$+ 2r_H r_A \cos(\phi_H - \phi_A)\, D_H\, C(z_{H,A})$$

$$+ 2r_P^2 \cos(\phi_{P1} - \phi_{P2})\, D_{P1}\, C(z_{P1,P2}) \qquad \text{(A4)}$$

The first five terms in Eq. A4 are phase-independent terms and are calculated from measured and predicted reflection coefficients. Terms 6-11 are coherent reflection terms dependent on the distance between the radiometer and the load and are proportional to the reflection coefficient of the radiometer. The radiometer/load phase difference is unknown, so our best estimate of these terms is zero with an error equal to the rms. We use the linear sum of these terms to estimate the magnitude of the position dependent reflection effect. This estimate of the error due to these coherent reflection terms is conservative because we have used the linear sum whereas some of the terms could partially cancel each other. Note that each term in the sum has a large uncertainty due to our poor knowledge of r_R. We estimate the error in r_R as +100%/-50%.

The last seven terms (12-18) are coherent reflection terms dependent on the separations between the reflecting surfaces within the load. Because they are independent of radiometer position, we group these terms with the incoherent reflection terms. The ir-blocking window separation is known to ±1 cm, so the phase difference in term 12 is known. Our best estimate of this term is included as a correction and ±50% of this term is included in the calculation of the uncertainty in the incoherent reflection.

The last six terms (13-18) depend on separations which are not well known. The phases of the polyethylene window reflection and the LHe surface reflection vary during calibration. We have no knowledge of the phase of the reflection from the absorber. We average over the unknown phases and take the quadrature sum of terms 13-18 as a contribution to the incoherent reflection uncertainty. For the radiometers used at the South Pole in 1989, Table A1 shows some of the radiometer parameters which enter into Eq. A4 and Table 2 shows the values of the resulting terms.

APPENDIX B: Antenna/Cold Load Interface Reflection

The term for antenna/load reflection in Appendix A is taken to be negligible and dropped to simplify the calculation of the load reflection. That approximation is based on an analysis of the matching between the pyramidal, E-plane corrugated antenna of the 20 cm wavelength radiometer and the load. At the long-wavelength limit of the operating range, the approximation to free-space is poor, interface reflections should be largest, and the interface reflection is most difficult to measure.

We model the antenna-load interface by an interface from E-plane corrugated rectangular waveguide to circular guide and calculate the mode conversion. This approximates the 19°-flare horn antenna by a straight waveguide with only the $HE_{1,2}$ fundamental mode propagating.[35] The $HE_{1,2}$ field distribution at the interface is matched to the 16 modes with cutoff wavelengths above 20 cm for the 78 cm radiometric wall diameter. The amplitudes are determined by calculation of overlap integrals and requiring energy conservation.[36,37] The results show that the $HE_{1,2}$ mode matches very well to the circular guide: the rectangular mode amplitude reflection coefficients are all $< 5 \times 10^{-3}$ and the amplitude reflection of the fundamental is 3×10^{-4}. The modes launched into the circular guide have amplitudes which decrease rapidly with increasing mode number.

The 12 cm wavelength radiometer antenna is based on the same design as the 20 cm wavelength antenna and the shorter wavelength should give a better match. At shorter wavelengths, the free-space approximation is better and we measure the difference in antenna/load and antenna/sky interface power reflection by placing the transition plate over the antenna and observing the signal change. These tests are consistent with no effect at the 25 mK level at 4 cm wavelength.

While antenna/load interface effects seem to be small, further study of differences in sky and load reflections should be undertaken. Here, we take this effect to be negligible and, because it is very instrument-dependent, we do not include it in the load analysis.

[a] Present address: Laboratory for Astronomy and Solar Physics, Code 685.3, NASA Goddard Space Flight Center, Greenbelt, MD 20771.

[b] Present address: Jet Propulsion Laboratory, ms 169-506, Pasadena, CA 91109.

[1] G. Smoot, *et al. Phys. Rev. Lett.*, **51**, 1099 (1983).

[2] A. Kogut, M. Bensadoun, G. De Amici, S. Levin, G.F. Smoot, and C. Witebsky, Astrophys. J. , **355**, 102 (1990).

[3] G. De Amici, M. Bensadoun, M. Bersanelli, A. Kogut, S. Levin, G. Smoot, and C. Witebsky, Astrophys. J., **359**, 219 (1990).

[4] G. Sironi, G. Bonelli, M. Limon, Astrophys. J., **378**, 550 (1991).

[5] M. Bensadoun, M. Bersanelli, G. De Amici, A. Kogut, M. Limon, S. Levin, G.F. Smoot, and C. Witebsky, Astrophys. J. , in preparation (1992).

[6] S. Levin, M. Bensadoun, M. Bersanelli, G. De Amici, A. Kogut, S. Levin, M. Limon, G. Smoot, Astrophys. J., submitted (1992).

[7] G. De Amici, M. Bensadoun, M. Bersanelli, A. Kogut, S. Levin, M. Limon, G. Smoot, Astrophys. J., **381**, 341 (1991).

[8] This measures power in units of antenna temperature T_A which is related to the thermodynamic temperature T of the source by $T_A = T\, x\, (e^x - 1)^{-1}$, where $x = h\nu/kT$. Over the operating range of the CL, $T_A \approx T$.

9 A. Kogut, M. Bensadoun, M. Bersanelli, G. De Amici, S. Levin, M. Limon, and G. Smoot, in AIP Conf. Proc. 222: **After the First Three Minutes**, edited by S. Holt, C. Bennet, and V. Trimble (AIP, New York, 1991), p 62.

[10] A.A. Penzias, IEEE Trans. Microwave Theory Tech., **MTT-16**, 608 (1968).

[11] M. Limon, C. Marchioni, and G. Sironi, J. Phys. E. (UK), **22**, 963 (1989).

[12] For a review of CMB measurements up to 1980, see R. Weiss, Annu. Rev. Ast. Astrophys., **18**, 489 (1980).

[13] R.A. Stokes, R.B. Partidge, and D.T. Wilkinson, Phys. Rev. Lett., **19**, 1199 (1967).

[14] M.S. Ewing, B.F. Burke, and D.H. Staelin, Phys. Rev. Lett., **19**, 1251 (1967).

[15] D.T. Wilkinson, Phys. Rev. Lett., **19**, 1195 (1967).

[16] C. Witebsky, Ph. D. Thesis, Dept. of Astronomy, U.C. Berkeley (1985).

[17] G. Smoot *et al.*, Astrophys. J. Lett., **291**, L23 (1985).

[18] G.F. Smoot, M. Bensadoun, M. Bersanelli, G. De Amici, A. Kogut, S. Levin, and C. Witebsky, Astrophys. J. Lett., **317**, L345 (1987).

[19] M. Bersanelli, C. Witebsky, M. Bensadoun, G. De Amici, A. Kogut, L. Levin, and G. Smoot, Astrophys. J., **339**, 632 (1989).

[20] A. Kogut, M. Bersanelli, G. De Amici, S.D. Friedman, M. Griffith, B. Grossan, S. Levin, G.F. Smoot, and C. Witebsky, Astrophys. J. **235**, 1 (1988).

[21] Eccosorb is manufactured by Emerson & Cuming, Gardena, CA.

[22] G. Sironi, private communication (1988).

[23] S. Ramo, J.R. Whinnery, T. Van Duzer, **Fields and Waves in Communication Electronics**, (Wiley, New York, 1965), pp. 351, 335.

[24] Manufactured by Fluorglas, a division of Allied Signal.

[25] Teflon is manufactured by E.I. DuPont de Nemours & Co., Inc., Wilmington, DE.

[26] S. Ramo, J.R. Whinnery, T. Van Duzer, *op. cit.*, p. 288.

[27] J. Bardeen, J. Appl. Phys. 11, 88 (1940).

[28] M. Halpern, H.P. Gush, E. Wishnow, V. De Cosmo, Appl. Opt., **25**, 565 (1986).

[29] M. Duriex and R.L. Rusby, Metrologia, **19**, 67 (1983).

[30] S. Ramo, J.R. Whinnery, T. Van Duzer, *op. cit.*, p. 434.

[31] G. Sironi, M. Limon, G.L. Marcellino, G. Bonelli, M. Bersanelli, G. Conti, and K. Reif, Astrophys. J., **378**, 550 (1991).

[32] G. Sironi and G. Bonelli, Astrophys. J., **311**, 418 (1986).

[33] G. De Amici, G. Smoot, J. Aymon, M. Bersanelli, A. Kogut, S. Levin, and C. Witebsky, Ap. J., **329**, 556 (1988).

[34] D.G. Johnson and D.T. Wilkinson, Astrophys. J. Lett., **313**, L1 (1986).

[35] C. Witebsky, G.F. Smoot, S. Levin, and M. Bensadoun, IEEE Trans. Antennas Propag., **AP-35**, 1310 (1987).

[36] A. Wexler, IEEE Trans. on Microwave Theory and Techniques, **MTT-15**, 508 (1967).

[37] M.S. Narasimhan and V. Venkateswara Rao, IEEE Antennas and Propagation, AP-21, 320 (1973).

TABLE 1. Relevant Geometrical and Physical Parameters of the 1988 Cold Load (described in this paper) and the 1982 Cold Load (see ref. 1 and §I.A)

Quantity	Dimension (cm)	
	1988 CL	1982 CL
bucket dewar depth (at wall)	133	132
bucket dewar i.d.	81.3	76.2
radiometric wall (RW) i.d.	77.7	70
distance from top of RW to top polyethylene window	0.5	0.5
distance from top of RW to top Fluorglas window	74	...
distance from top of RW to absorber tips	112	143
distance from top of RW to absorber base	148	163
separation of polyethylene windows (at edge)	3.8	15
separation of ir-blocking windows	5.1	...
height of absorber pyramids	25	15

TABLE 2. Contributions to the Reflection Coefficient r^2. The effect of the smaller antenna apertures is taken into account by the dilution factor, D (see Appendix A and Table A1). The position-dependent coherent reflection (0.7 times the sum of the reflections dependent on antenna position) predicts the amplitude of the sinusoidal variation in output obtained by varying the antenna/load separation (see Table 5). The amplitude of the coherent reflection independent of antenna position is quoted (the phase of this term is unknown). To get reflected signal in K, multiply by T_B-T_{abs} from Table A1.

Source	Error in Source	Reflectivity 20 cm [10^{-5}]	12 cm [10^{-5}]	7.9 cm [10^{-5}]	4.0 cm [10^{-5}]
Polyethylene windows power reflection ($2r_P^2$)	±10%	0.041	0.11	0.26	1.0
ir-blocking windows power reflection ($r_{F1}^2 D_F + r_{F2}^2 D_F$)	±100%	0.96	4.1	4.4	2.9
Liquid helium power reflection ($r_H^2 D_H$)	±1%	11	11	2.5	0.54
Absorber power reflection ($r_A^2 D_H$)	±50%	35	10	0.92	0.050
Position-independent coherent reflection (amplitude of sine curve)	±71%	24	15	3.6	0.68
Position-dependent coherent reflection (amplitude of sine curve)	±71%	16	17	20	4.5

TABLE 3. Window Material Properties and Emissivity. Emissivities are for the indicated thickness of material at each wavelength. The absorption coefficient, α, for glass is from extrapolation of published data and measured values. The data for glass at 290 K give upper limits on the emissivity at lower temperature. The error on the polyethylene and glass emissivities are ±33% and ±50%, respectively.

Material	Material Properties				Window Emissivity			
	ε	$\tan\delta$	α (cm^{-1})	t	20 cm	12 cm	7.9 cm	4.0 cm
		(10^{-4})	(10^{-4})	(μm)	(10^{-6})	(10^{-6})	(10^{-6})	(10^{-6})
Polyethylene	2.26	3 to 6		23	0.49	0.81	1.2	2.4
TFE Teflon	2.08	4		25	0.46	0.77	1.2	2.3
glass (290K)	5.9		7.1	50	3.6			
			16	50		8.1		
			31	50			16	
			93	50				47

TABLE 4. Emission from the Windows and Radiometric Wall. Emissivity data are from Table 3. Fluorglas emission is for 50 μm of glass and 25 μm FEP Teflon per layer. Wall emission is from a mode loss calculation at λ = 20 cm, and from beam integration at λ = 7.9 and 4.0 cm; the value at λ = 12 cm is interpolated. The contribution from joints is listed separately.

Source	Physical Temperature	Emission			
		20 cm	12 cm	7.9 cm	4.0 cm
	(K)	(mK)	(mK)	(mK)	(mK)
Polyethylene windows	250±10	0.3±0.1	0.4±0.1	0.6±0.2	1.2±0.5
Upper ir-blocking window	50±10	0.2±0.1	0.4±0.2	0.8±0.3	2.2±0.9
Lower ir-blocking window	25±10	0.2±0.1	0.4±0.3	0.8±0.3	2.2±1.3
Wall (w/out joints)	4-250	4±4	2±2	0±1	0±1
Wall joints	30-250	13±13	7±7	2±2	2±2
Absorber Leakage	20±10	7±7	0.7±0.8	0	0
Total Emission		25±16	11±7	5±3	8±3

TABLE 5. Coherent Reflection Test Summary. The predicted amplitude is from Table 2 and Table A1; the uncertainty is +100%/-50%, arising from the uncertainty in r_R. All measurements give only upper limits on the effect; the 1σ limit is shown. No measurement was made at 12 cm wavelength.

	Amplitude of Effect (mK)			
	20 cm	12 cm	7.9 cm	4.0 cm
Predicted	8	5	18	13
Measured	< 14	...	< 30	< 21

TABLE 6. Cold Load Antenna Temperature. The values are for the four radiometers which used this load at the South Pole in Dec 1989. The absorber leakage is included in the wall emission. The pressure over the LHe bath was 520 Torr, corresponding to a thermodynamic temperature of 3842 mK. $T_{A,CL}$ is the absorber emission plus the total correction.

Source	Signal			
	20 cm (mK)	12 cm (mK)	7.9 cm (mK)	4.0 cm (mK)
Window emission	1± 1	1± 1	2± 1	6± 2
Radiometric wall emission	24±16	10± 7	2± 2	2± 2
Incoherent reflection	23±15	7± 4	6± 5	7± 9
Coherent reflection	0± 8	0± 5	0±18	0±13
Total correction to absorber emission	48±23	18±10	10±18	15±16
Absorber emission	3806± 2	3782± 2	3752± 2	3665± 2
Cold load antenna temperature, $T_{A,CL}$	3854±23	3801±10	3762±19	3679±16

TABLE 7. Comparison of Cold Loads Used for Long-Wavelength Measurements of the CMB. Characteristics are given at the wavelength of each measurement. r^2 is the incoherent (power) reflection coefficient (including any correction for illumination). T_B is the radiometer broadcast temperature. Subscripts RW and W designate the radiometric wall and windows, respectively. The total correction to the LHe bath temperature is given by T_{CORR}. Values for 'this work' are from Table 6. When the design required a break in the horn, or when the cold load and sky signals reached the radiometer following different paths, the correction for antenna emission is given by T_{Horn}.

Measurement	λ (cm)	r^2 (10^{-4})	r^2T_B (mK)	$e_{RW}T_{RW}$ (mK)	e_WT_W (mK)	T_{CORR} (mK)	T_{Horn}[a] (mK)
Sironi *et al.* 1990[b]	50	13±3	455±105	1450±280	0	1900±300	1550±130
Sironi *et al.* 1990[b]	12	28±3	140±15	4760±300	0	4800±300	26780±500
this work	20	5.2	26±19	24±16	1±1	48±29	...
this work	12	1.5	7±2	10±7	1±1	18±14	...
this work	7.9	0.5	7±4	2±2	2±1	10±24	...
this work	4.0	0.5	13±8	2±2	6±2	15±18	...
Stokes *et al.* 1967[c]	3.2	6±3	20±10	160±100	60±20	240±100	[d]
Stokes *et al.* 1967[c]	1.58	10±3	30±10	210±80	40±10	280±80	3
Wilkinson 1967[c]	0.856	0±3	0±10	280±110	60±60	340±125	...
Johnson and Wilkinson 1987[e]	1.2	5	0±18[f]	0	35±12[g]	35±22	50±12

[a] '...' indicates that the calibration was at the horn aperture

[b] coaxial cold load used is that described in Limon *et al.* 1989. These measurements were conducted in 1988 at Alpe Gera, Italy. The 12 cm wavelength radiometer, the same instrument as that used in 'this work', is capable of using either load.

[c] the measurements at 3.2, 1.58 and 0.856 cm used the same cold load

[d] no value for this quantity is given

[e] the cold load is an integral part of the radiometer

[f] difference in horn and load reflection using conservative error bars added in quadrature

[g] window is viewed during sky observation and not during cold load calibration

TABLE 8. Comparison of CMB Measurements Made with the 1982 and 1988 Cold Loads

Year	1986	1987	1988	1989
Observing Site	White Mountain	White Mountain	White Mountain	South Pole
λ (cm)	8.1[a]	7.9	7.9	7.9
Load used	1982	1982	1988	1988
Predicted $T_{A,CL}$	3735±55	3742±38	3697±21	3762±19
$T_{A,Atm}$	870±108	898±64	955±55	1109±60
$T_{A,CMB}$	2580±130	2460±79	2621±65	2549±74

[a] radiometer center wavelength was changed from 8.1 cm in 1986 to 7.9 in 1987; the bandwidth was also reduced, from 460 MHz to 200 MHz, which increased the amplitude of the coherent reflection terms for this radiometer.

TABLE A1. Radiometer-Dependent Reflection Coefficient Parameters in Eq A4. r_R^2 has a factor of 2 uncertainty. For reflection dilution factors, $D_A \sim D_H$ and $D_F \equiv D_{F1} \sim D_{F2}$. The coherence factor $C(z_{F1,F2}) \sim 1$ and average values are given for terms like $C(z_{R,H})$ which depend on the LHe level.

Quantity	Units	Value			
		20 cm	12 cm	7.9 cm	4.0 cm
r_R^2		0.01	0.01	0.1	0.01
L	(cm)	150	187	150	60
T_B-T_{abs}	(K)	50	27	86	279
D_F		1	1	0.46	0.079
D_H		1	1	0.23	0.050
$C(z_{R,F})$		0.044	0.045	0.026	0.0074
$C(z_{R,H})$		0.025	0.028	0.017	0.0042
$C(z_{F,H})$		0.44	0.60	0.44	0.071
$C(z_{F,A})$		0.22	0.34	0.22	0.035
$C(z_{H,A})$		0.87	0.92	0.87	0.39

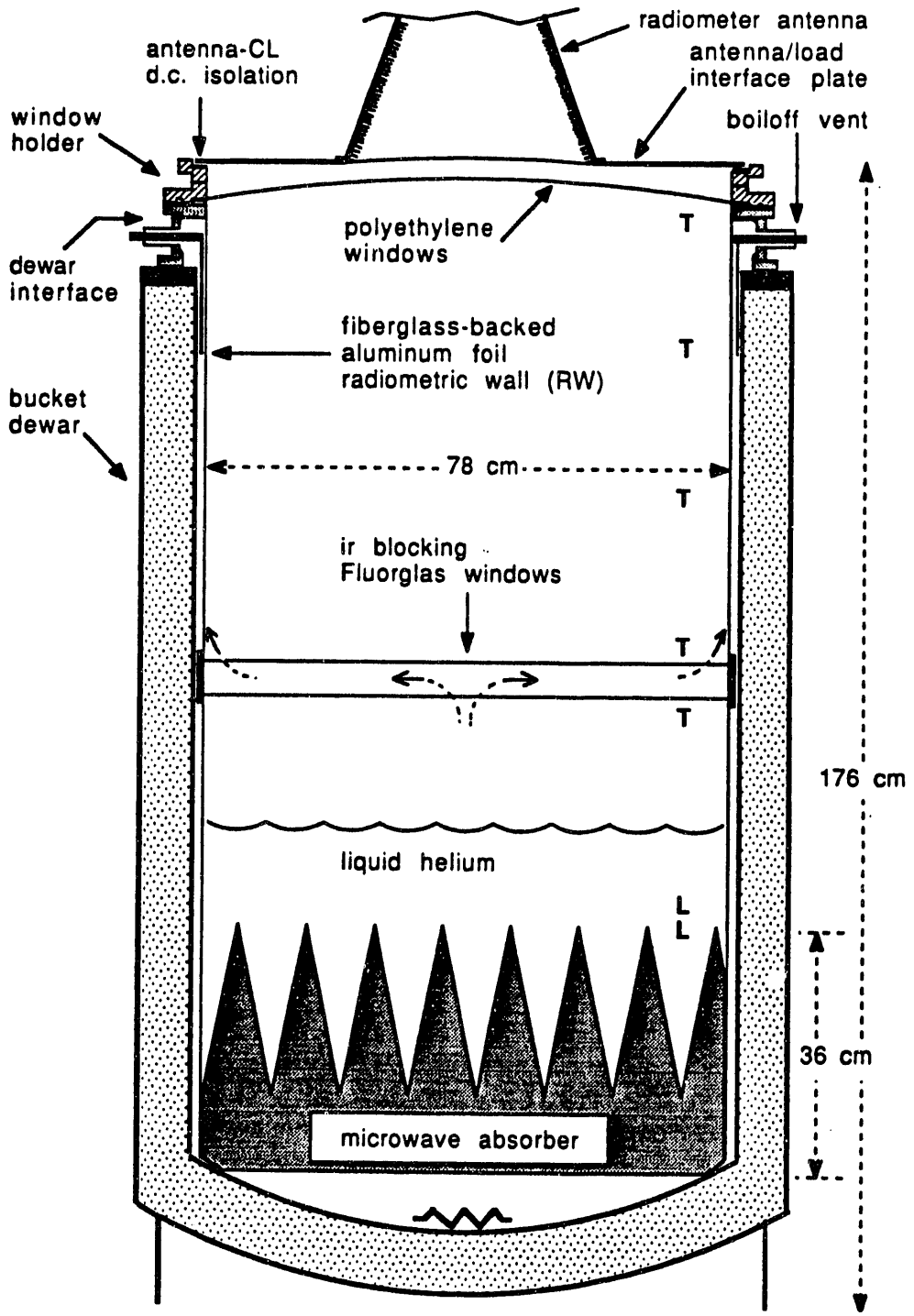

FIG. 1. Cross-sectional schematic of the cylindrical cold load. The He boiloff gas flows through holes in the ir-blocking windows (as indicated), then through the radiometric wall, up the annular space (not shown) and out the vents. The location of several of the discrete level sensors and temperature sensors are indicated by **L** and **T** respectively. The resistive heater at the bottom of the CL is shown. The ir-blocking windows of the present load replace a manually operated shutter which was located just below the polyethylene windows of the 1982 load.

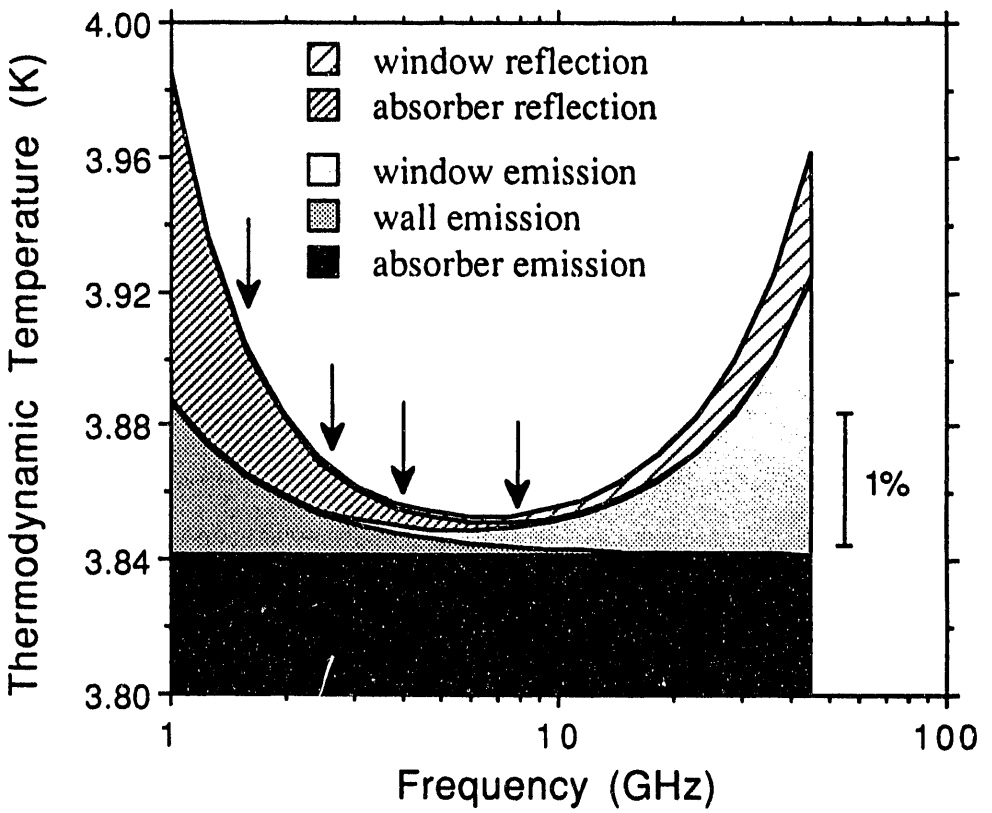

FIG. 2. Approximate contributions to the thermodynamic temperature of the cold load. Contributions due to reflection and wall emission depend on the specific properties of the radiometer observing the load. 1% of the total load signal is indicated on the right. Four arrows at 1.47, 2.5, 3.8 and 7.5 GHz (20, 12, 7.9, and 4.0 cm wavelength) indicate the frequencies of the four radiometers which calibrated with the load at the South Pole in 1989. The window performance limits the high frequency performance of the load while the absorber and wall emission limit the low frequency performance of the load.

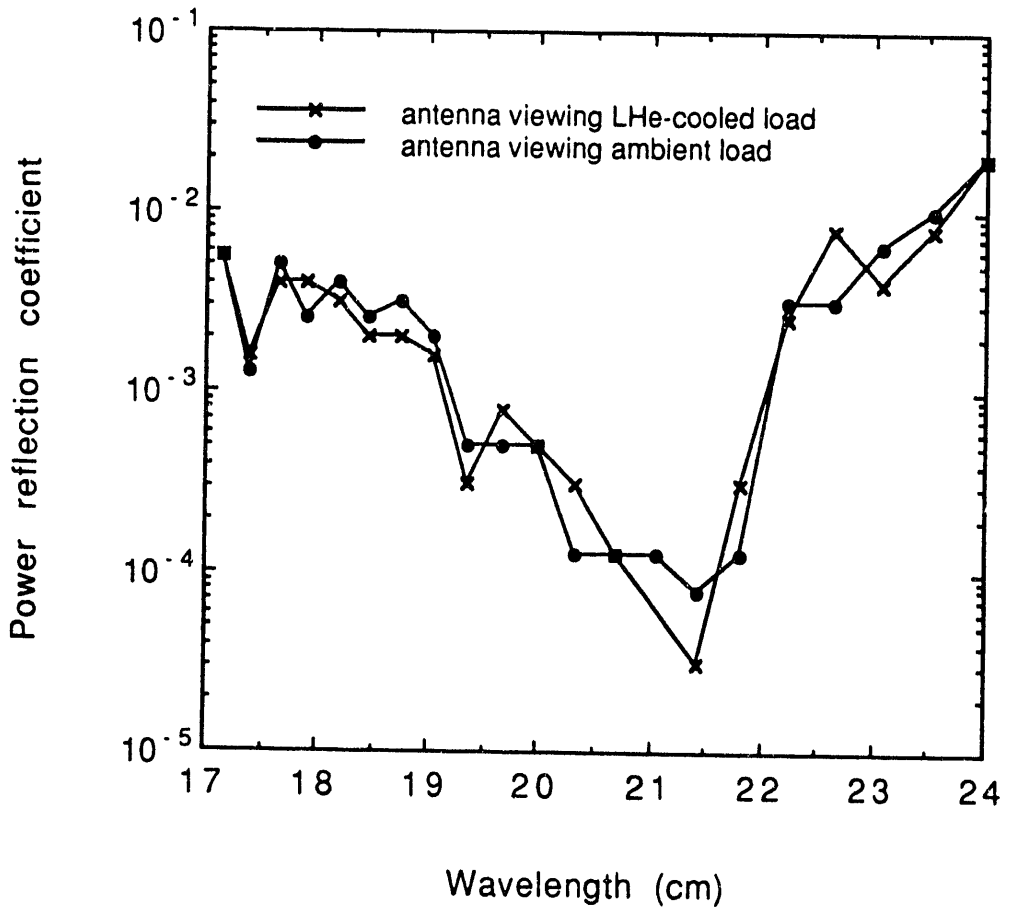

FIG. 3. Reflection measured with the 20 cm wavelength radiometer. (a) Comparison of the total (antenna and load) reflection with the antenna observing the absorber at ambient and LHe temperatures. The measurement was made with a slotted line inserted between the radiometer antenna and waveguide-coaxial transition.

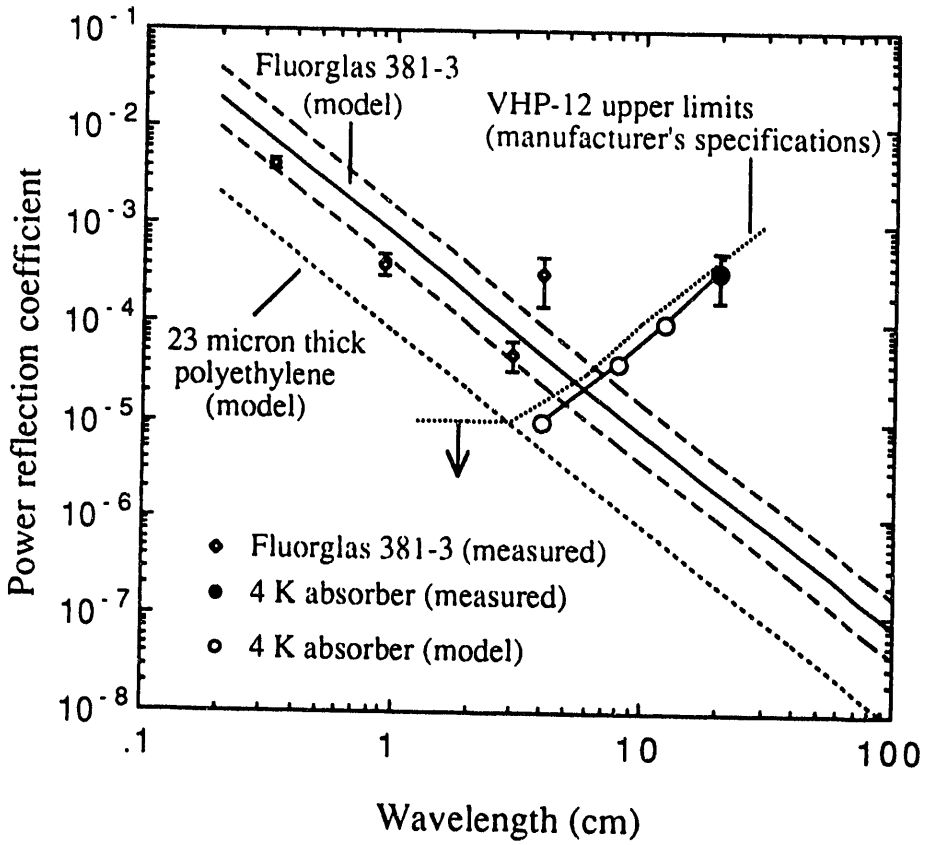

FIG. 4. Absorber and window power reflection coefficients. The absorber used has additional backing to give lower reflection than the manufacturer's specified upper limit for Eccosorb VHP-12. The value at 20 cm is from the measurement in Fig. 3. Measured values are shown for a single thickness (68 μm) of the Fluorglas ir-blocking window material and the model (the value used in the analysis) is the average of the theoretically predicted value and the measured value at 0.91 cm wavelength. The uncertainty used for the Fluorglas reflection is indicated. Reflection from a single layer of 23 μm polyethylene is shown.

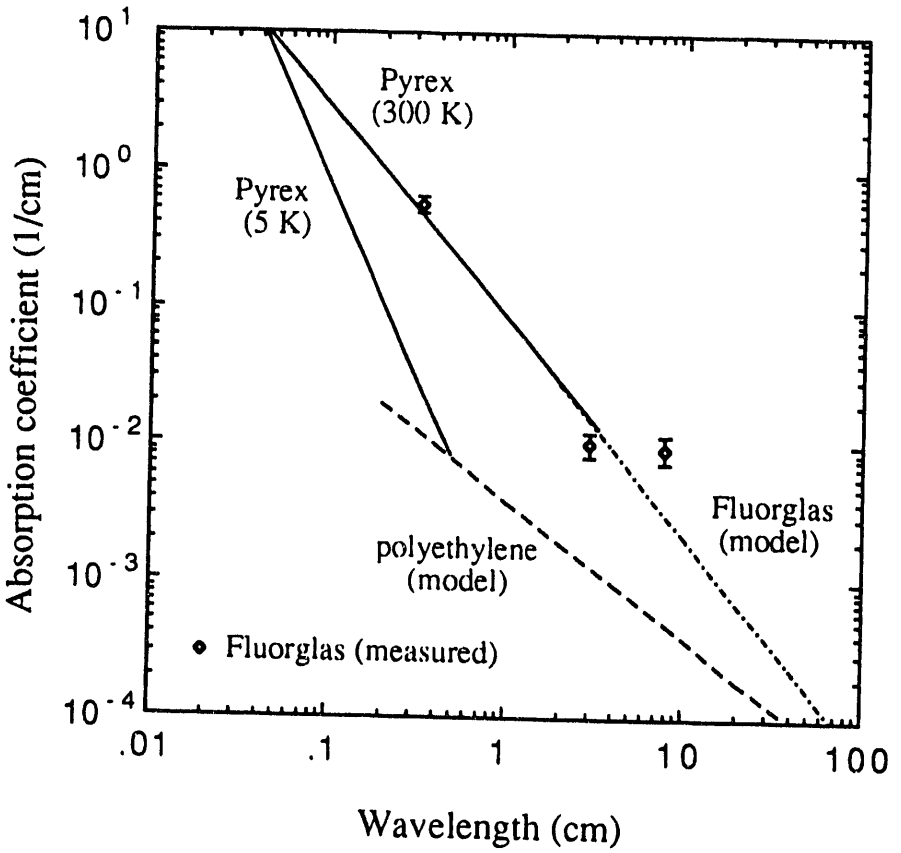

FIG. 5. Absorption coefficient of Fluorglas material. The radiometer data agree with the Pyrex data for $0.03 < \lambda < 0.3$ of Halpern *et al.* and their best fit parameters are used with an uncertainty of ±50% as indicated on the long-wavelength extrapolation. This uncertainty allows for a decrease in the absorption as the Fluorglas material cools.

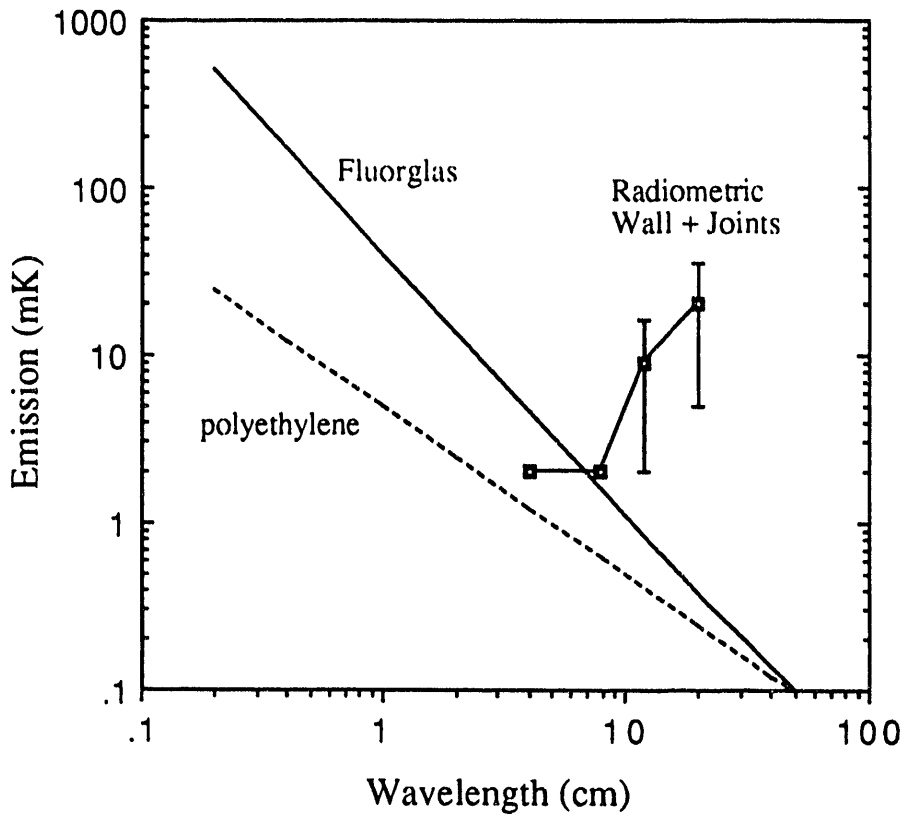

FIG. 6. Emission from windows and radiometric wall. Values are for the observed radiometric wall temperature profile. The upper and lower ir-blocking windows are at 50±10 and 25±10 K, respectively; the polyethylene windows are at 250±10 K. The radiometric wall data is calculated.

END

DATE FILMED

12 / 17 / 92